Max-Planck-Institut
für Meteorologie

MAX-PLANCK-GESELLSCHAFT

International Max Planck Research School
on Earth System Modelling

Scale interactions in high-latitude ecosystems

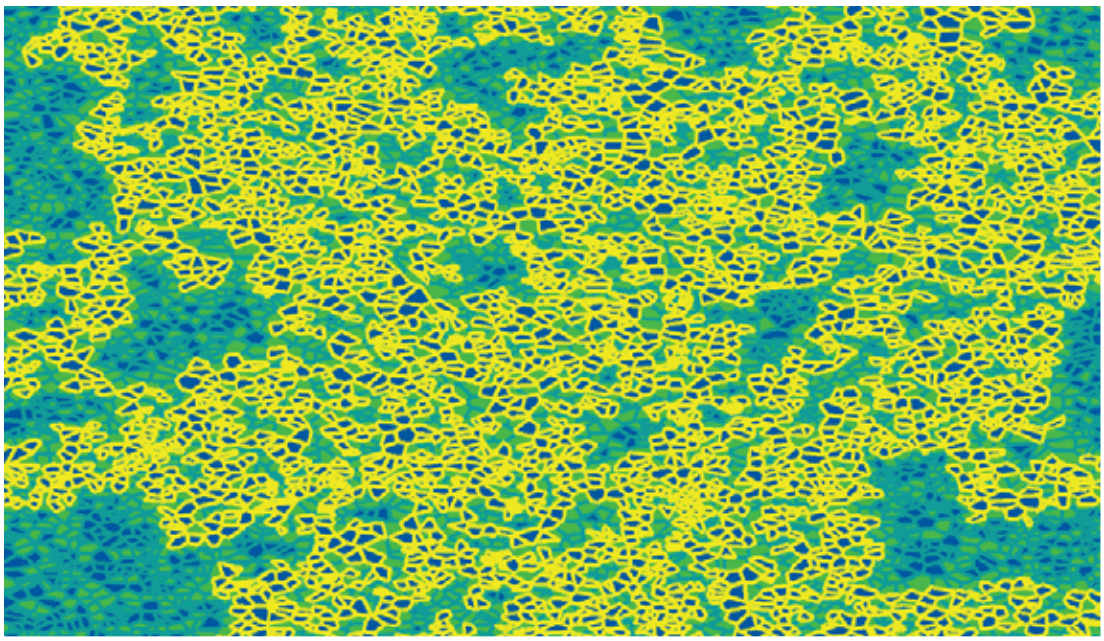

Fabio Cresto Aleina

Hamburg 2014

Berichte zur Erdsystemforschung
Reports on Earth System Science

157
2014

Hinweis

Die Berichte zur Erdsystemforschung werden vom Max-Planck-Institut für Meteorologie in Hamburg in unregelmäßiger Abfolge herausgegeben.

Sie enthalten wissenschaftliche und technische Beiträge, inklusive Dissertationen.

Die Beiträge geben nicht notwendigerweise die Auffassung des Instituts wieder.

Die "Berichte zur Erdsystemforschung" führen die vorherigen Reihen "Reports" und "Examensarbeiten" weiter.

Notice

The Reports on Earth System Science are published by the Max Planck Institute for Meteorology in Hamburg. They appear in irregular intervals.

They contain scientific and technical contributions, including Ph. D. theses.

The Reports do not necessarily reflect the opinion of the Institute.

The "Reports on Earth System Science" continue the former "Reports" and "Examensarbeiten" of the Max Planck Institute.

Anschrift / Address

Max-Planck-Institut für Meteorologie
Bundesstrasse 53
20146 Hamburg
Deutschland

Tel./Phone: +49 (0)40 4 11 73 - 0
Fax: +49 (0)40 4 11 73 - 298

name.surname@mpimet.mpg.de
www.mpimet.mpg.de

Layout

Bettina Diallo and Norbert P. Noreiks
Communication

Copyright

Max-Planck-Institut
für Meteorologie

MAX-PLANCK-GESELLSCHAFT

International Max Planck Research School
on Earth System Modelling

Scale interactions in high-latitude ecosystems

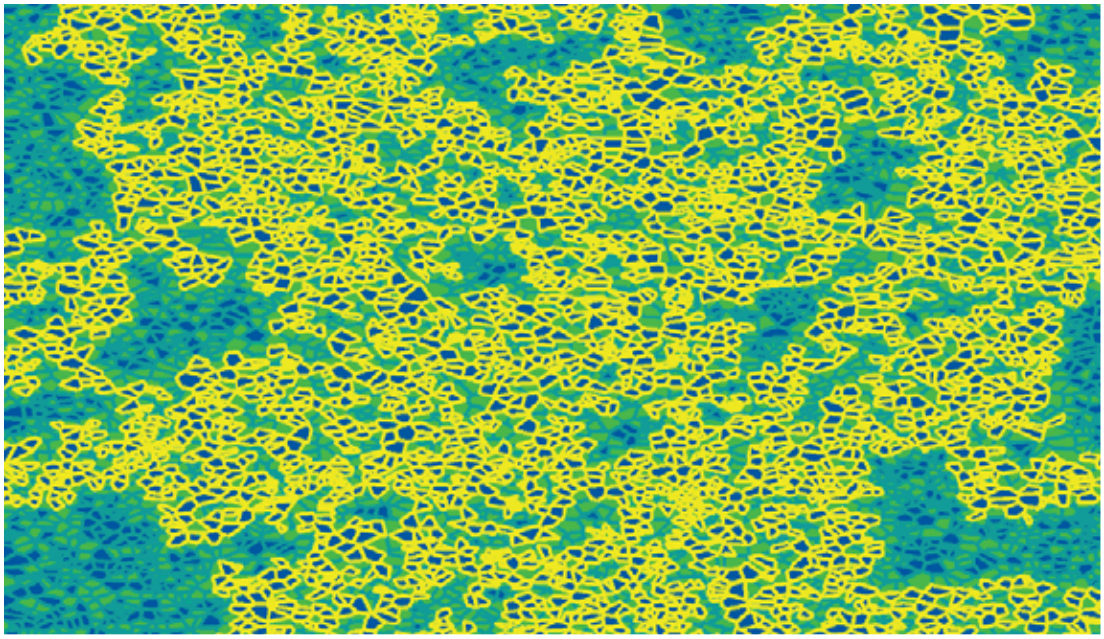

Fabio Cresto Aleina

Hamburg 2014

Berichte zur Erdsystemforschung
Reports on Earth System Science

157
2014

Fabio Cresto Aleina
aus Lanzo Torinese, Italien

Max-Planck-Institut für Meteorologie
Bundesstrasse 53
20146 Hamburg

Als Dissertation angenommen
vom Fachbereich Geowissenschaften der Universität Hamburg

auf Grund der Gutachten von
Prof. Dr. Martin Claussen
und
Dr. (habil.) Victor Brovkin

Hamburg, den 25. Juni 2014
Professor Dr. Christian Betzler
Leiter des Departments Geowissenschaften

ISSN 1614-1199

Abstract

Surface processes occur in various ecosystems and landscapes and at multiple spatial and temporal scales. Because of their small-scale, surface heterogeneities are often not represented or poorly parameterized in climate models. These local soil and vegetation heterogeneities are often important or even fundamental for energy and carbon balances. This is of particular interest in high-latitude ecosystems, because of the large amount of carbon stored in the soil of northern peatlands. Greenhouse gas fluxes, such as methane, carbon dioxide and water vapor, vary largely within the environment, also as an effect of the small-scale processes that characterize the landscape. Therefore, a characterization of the effects of such small-scale features on high-latitude environments is needed in order to consistently assess the water, carbon, and energy balance of these landscapes.

As a first example, I considered permafrost dominated landscapes in the Arctic lowlands, such as the polygonal tundra. These landscapes display characteristic small-scale features generated by contraction and expansion of water by freezing and melting cycles. These small-scale surface heterogeneities may deeply affect the hydrology in this environment. In the first part of my thesis I present a stochastic model for the surface topography of low center polygonal tundra using Poisson-Voronoi diagrams and I compare the results with available recent field studies. I analyze seasonal dynamics of water table variations and the landscape response under different scenarios of precipitation income. Using an idealized model for methane emissions, I can upscale methane fluxes at the landscape level. Hydraulic interconnections and large-scale drainage may also be investigated through percolation thresholds of the model. The model is able to reproduce the statistical characteristics of the landscape, from the area distribution to the water balance. This novel approach statistically relates large-scale properties of the system to the main small-scale surface heterogeneities, which are generally neglected in large-scale models.

In order to generalize the findings from the stochastic model, in the second part of my thesis I present a surface model for small-scale surface heterogeneities in boreal peatlands. Water table depth and dynamics are in turn regulated by the peatland micro-topography, i. e. the elevated and drier hummocks, and the lower and wetter hollows. A classical mean field approximation of a single bucket model may not be adequate to describe land-atmosphere interactions in northern peatlands. I can assess the potential effects of the representation of small-scale surface heterogeneities on greenhouse gas fluxes by coupling this fine scale model with a process based model for methane emissions. By partitioning of space in smaller subunits and then by analyz-

ing the landscape-scale behavior of the system, I am able to resolve the small-scale processes and to investigate their effects at larger scales. I not only investigate the influence of the hummocky surface on greenhouse gas emissions, but I also simulate how complex sub grid-scale hydrological interactions affect the average energy balance of the peatland.

In the last part of my thesis I present a pattern recognition analysis in order to relate the landscape-scale model to the working scale of General Circulation Models (GCMs). This novel application of the pattern recognition analysis can describe the dynamics of the patterns emerging from the small-scale models. Minkowski densities are a useful tool to measure patterns, as they can help to quantify emergent landscape-scale properties arising from local, small-scale interactions. I can link the behavior of the surface characteristics to the seasonal dynamics of greenhouse gases. In order to fill this scaling gap I develop a simple and novel parameterization, which significantly improves the output of the model running without micro-topography. This new parameterization is computationally analogous to the model running without micro-topographic representation, and it has the potential to be included in large-scale models, such as GCMs. It is a first step towards a comprehensive method to fill the general scale gaps in climate-biosphere interactions.

Contents

Chapter 1

Introduction

1.1 Motivation and open questions

Climate modeling involves representation of phenomena at a multiplicity of spatial and temporal scales. This is particularly true in the case of land surface modeling, where land-atmosphere interactions depend on surface heterogeneities with spatial scale generally varying between 10^0-10^2 m. Such scales are too small to be explicitly resolved in a climate modeling framework, typically working at a scale of 50-100 km. Rietkerk et al. (2011) highlighted how climate models generally miss the representation of small-scale land surface phenomena, and that a new parameterization of these surface heterogeneities is needed. Even though from a climate modeling perspective neglecting sub-grid scale surface heterogeneities may be a good first order approximation, it is possible that these local surface patterns may generate local feedback mechanisms able to modify the forcing itself. This not represented feedback loop can potentially lead to miss ecosystem-climate interactions at regional or even global scales (Janssen et al., 2008; Dekker and Rietkerk, 2007; Scheffer et al., 2005; Pielke, R. A., Sr et al., 1998). In Fig. 1.1 I show examples of sub-gird scale heterogeneities in high-latitude environments, which can potentially affect water, carbon, and energy balance in such ecosystems.

Many studies focused on land surface small-scale patterns, in particular highlighting mechanisms for pattern formation [i. e.,][](Schymanski et al., 2010; Rietkerk and van de Koppel, 2008; Couwenberg and Joosten, 2005). Recent works linked some spatial properties of vegetation patterning, particularly in water limited systems, to situations where the system becomes more and more sensitive to perturbations. The sensitivity of the system can become so large that the perturbations may lead to phase

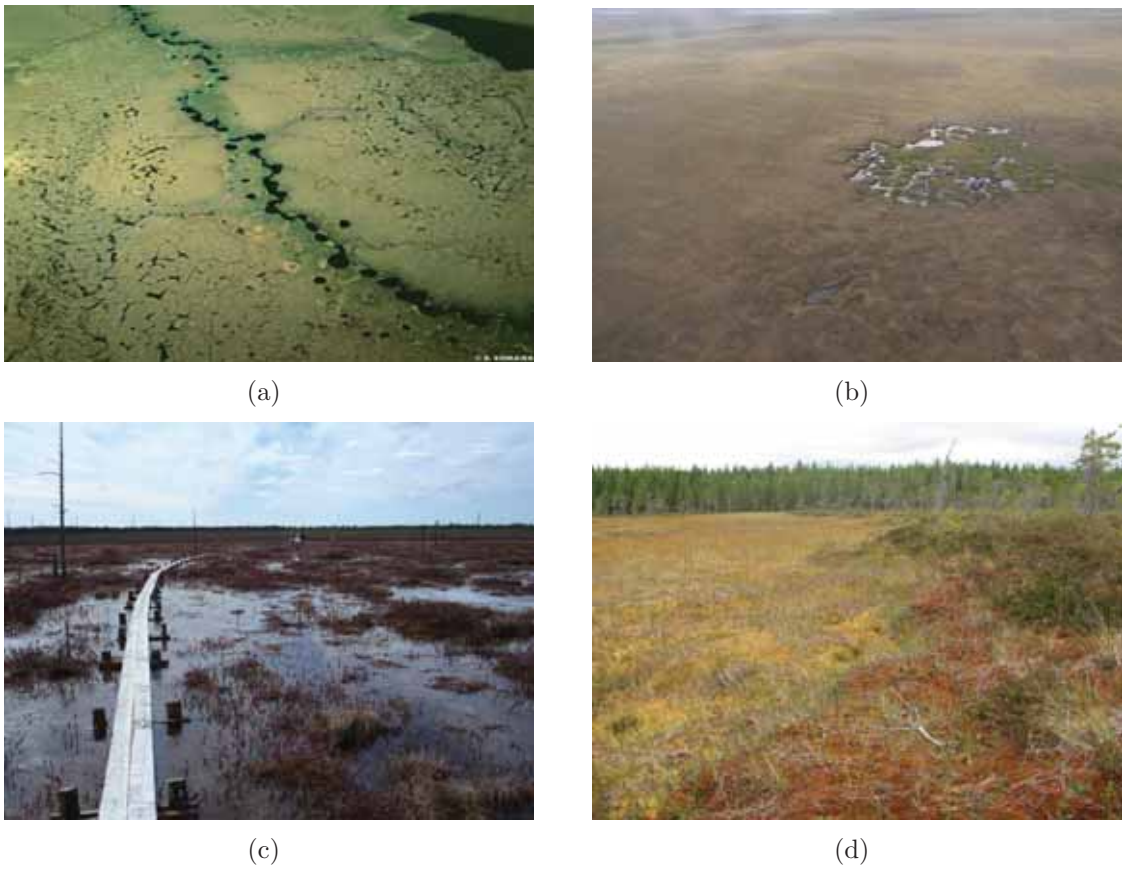

(a) (b)

(c) (d)

Figure 1.1: The Figure shows surface heterogeneities on high-latitude ecosystems, both in permafrost and in permafrost-free environments. Panel (a), is a picture from the IPA (International Permafrost Association) website. It shows a tessellated landscape consisting of low-center polygons. The progressive drying of the polygon surface leads to an amplification of the degradation of the ice wedges in the drier rims. This small-scale phenomenon causes the large-scale outflow visible in the lake chain in the center of the picture. Panel (b) shows an aerial photograph of a polygonal tundra landscape in Northern Seward Peninsula, Alaska, in 2012. The interpolygonal water flow degrades the permafrost within the rims and can initiate thermokarst lake formation. This phenomenon not only regulates the water flow and the energy and carbon exchange between permafrost environments and atmosphere, but it drastically changes the landscape and the ecosystem, transitioning a strongly organized polygonal ground to a potentially expanding lake. Photo taken by Guido Grosse. Panel (c) shows a picture from the Ust-Pojeg mire (Komi Republic, Russia) study site where the team of the Institute of Soil Science of the Hamburg University conducted measurement campaign. The sparse micro-topography shows how the water table position in respect to the surface vary over a flat landscape such as the mire. This is due to the heterogenous elevation of hummocks (small-scale relieves) and hollows (depressions). The picture is from the website of the Institute of Soil Science of the Hamburg University. Panel (d), finally, shows the elevation profile of the hummock-hollow stripe transition in a peatland near the Bothnian Bay, Sweden. The different colors of the vegetation also indicate different types of biomes and plant communities between the two micro-topographic features. Picture taken by the author.

transitions in ecosystem states. Pattern properties can be used as early warning signals for such catastrophic shifts in ecosystem states (i. e., Kéfi et al., 2007, 2013). Other studies focused on the impact of climate on vegetation dynamics, demonstrating how the climatic forcing is a key factor in determining characteristics of the small-scale vegetation patterns (Kletter et al., 2009; von Hardenberg et al., 2001; Dijkstra, 2011). As mentioned, small-scale vegetation patterns may in turn feed back on climate, changing the forcing. Baudena et al. (2013) showed how, by changing the shape and the type of the vegetation pattern, land-atmosphere water fluxes can vary up to 10 %. Studies that close the feedback loop from climate forcing on land surface, to the response of climate to potential variations of land-atmosphere fluxes due to sub-grid scale heterogeneities are almost absent. Melton and Arora (2014) recently showed that sub-grid scale variability plays an important role in the model response to a changing climate. In their study, two different representations of sub-grid scale variability of plant functional types (PFTs) lead to different effects on the magnitude of the global terrestrial carbon sink.

This issue concerning sub-grid scale heterogeneity effects on fluxes is of particular interest and importance in northern peatlands and in periarctic environments in general, as pointed out by Baird et al. (2009b). The total amount of carbon in the circumpolar regions, both in permafrost and in permafrost-free organic soils, has been recently estimated in 1672 Pg, which is approximately 50% of the world soil carbon (Tarnocai et al., 2009; Hugelius et al., 2013). Northern peatlands, i. e. wetlands with at least a layer of 30 cm of organic soil on top, despite covering only up to the 3% of the land surface area, contain large amount of partially decomposed carbon, which is susceptible to be emitted either as CO_2 or CH_4. Recent estimates by Yu et al. (2010) computed the amount of carbon stored in boreal peatlands of about 547 (473-621) Pg, significantly larger than previous estimates of 270-370 Pg (i. e., Turunen et al., 2002). Such environments are likely to experience the largest increase in temperature in the next 100 years due to the abrupt climatic change and due to the so-called Arctic amplification (i. e., Pithan and Mauritsen, 2014). Therefore it is likely that local changes in such a key region for the carbon cycle can have global effects. In order to understand and project the soil carbon storages, one has to consider the controls on land-atmosphere fluxes and the feedbacks arising from such interactions, which may in turn depend on small-scale surface heterogeneities. Accounting for such information may be fundamental, especially because nonlinear relationships are involved in the processes driving greenhouse gas emissions (Stoy et al., 2009; Mohammed et al., 2012). Recent efforts tried to reproduce permafrost, peatland and wetland extent and carbon accumulation in various Dynamic Global Vegetation Models (DGVMs) and in

Earth System Models (ESMs), which couple the land surface with atmosphere and ocean dynamics, (i. e., Ekici et al., 2013; Schuldt et al., 2013; Kleinen et al., 2012; Wania et al., 2009a,b). Regarding wetland extent, results of simulations with different DGVMs are reassumed in the WETCHIMP intercomparison project by Melton et al. (2013); Wania et al. (2013). Despite the large differences in process parameterizations and representations among the DGVMs used in the intercomparison project, it is clear that all of them lack representation of fine scale heterogeneities and sub-grid scale processes. Because of the lack of such representations in the models, it is still unknown the extent of the effects of surface heterogeneities on land-atmosphere fluxes in northern peatlands. Considering the need to fill the gap among different spatial scales in carbon-rich high-latitude ecosystems, I can formulate the overarching research question of the present thesis as:

How do sub-grid scale surface heterogeneities influence climate-biogeosphere interactions in high-latitude ecosystems?

In order to asses the potential effects in different environments, I start my investigations in periarctic environments, focusing my attention on the ice-wedge polygonal tundra, a typical ecosystem of the Arctic lowlands. Such patterned grounds play a dominant role in determining surface morphology, drainage and patterns of vegetation (French, 2007). In particular, low center polygonal tundra typically consists of elevated and comparatively drier rims, and of lower and wetter centers. The environment displays a large variability, and several experimental studies focussed on the controls of such sub-grid scale heterogeneities on greenhouse gas emissions (see e.g. Sachs et al., 2008, 2010; Wille et al., 2008; Kutzbach et al., 2004), on hydrological properties (Boike et al., 2008), and of surface energy balance (Langer et al., 2011b,a). Recent studies with the help of remote sensing data were able to capture and analyze surface heterogeneities (i. e., land cover and surface temperature). They highlighted the importance of small-scale surface heterogeneities for the land-atmosphere water fluxes (Muster et al., 2012; Langer et al., 2010). Langer et al. (2013) presented a satellite-based modeling study for predicting temperature trends in such environments, but not all characteristics can be detected by remote sensing. Therefore, a different modeling approach, able to combine local data and statistical representation of the small-scale heterogeneities, is needed to consistently model properties, such as the regional water balance. I therefore address the following research questions:

How can we represent multi-scale phenomena in permafrost environments, such as the polygonal tundra, from the single polygons to the landscape-scale? How and to which extent do sub-grid scale surface heterogeneities control the water balance in the polygonal tundra?

Small-scale surface heterogeneities play an important role also in permafrost-free boreal ecosystem. Surface heterogeneities are typical in peatlands and consist of small and relatively drier relieves, called *hummocks*, and of lower and wetter zones, called *hollows*. Local mechanistic surface models suggested the potential role of the micro-topography in boreal peatlands in regulating water and carbon balance (i. e., Nungesser, 2003; Bohn et al., 2013). In northern peatlands the position of the water table is a fundamental control on greenhouse gas emissions, since it changes the depth of the oxic zone, i. e., the region where methane fluxes coming from below can be oxidated and therefore released as carbon dioxide (Waddington et al., 1996; Kettunen et al., 1999; Moore and Knowles, 1989). As the two gases have different greenhouse properties, it is difficult to estimate the climate impact of natural wetlands and peatlands without precise estimate of methane emissions (Kirschke et al., 2013). In order to compute a consistent greenhouse balance over the landscape, one should consider the small-scale micro-topography and how water table and soil surface heterogeneously change within the environment (Bellisario et al., 1999; Camill and Clark, 1998; Law et al., 2002). Water table position can potentially also control other variables, such as the ecosystem-scale energy balance, due to the different heat capacity between water and peat. In order to understand all these processes and their links among each other, a new modeling framework, combining micro-topography representation, methane emissions, and a dynamical computation of peatland energy balance, is needed. Hence, I address the following research question:

What are the effects of micro-topography on water, carbon, and energy balance in a typical boreal peatland?

Land surface models such as JSBACH (Raddatz et al., 2007), the DGVM included in the Earth System Model MPI-ESM, work at a spatial resolution of about 50 x 50 km at the finest scale. Even a geometric tessellation approach, besides the additional computational cost it would carry, is unfeasible to be incorporated in a global model because of consistency issues with the other model components. On the other hand, prediction of greenhouse gas fluxes may be underestimated or generally wrongly represented by neglecting the information coming from the local surface heterogeneities. The problem is similar to the one of coarse-graining in physics of complex systems. Starting from a fine grained description of a system with a large number of elements one tries to infer large-scale properties by coarsening the resolution of the model, ultimately finding an effective theory able to preserve the information useful for a final prediction (i. e., DeDeo, 2011; Gell-Mann and Low, 1954). What is needed is therefore a theory able to describe observations, but explicitly without the claim that the model represents the actual processes at play in the observed phenomena to which the

theory is calibrated. The methodological framework is shown in Figure 1.2. In order to develop such an effective theory, it is necessary to develop and use a method to consistently identify and to quantify the larger-scale features of the patterns emerging from sub-grid heterogeneities and from their interaction. To tackle this problem I formulate the following research questions:

How can we identify the landscape-scale properties of the patterns emerging from sub-grid scale heterogeneities in boreal ecosystem? How can we develop an effective theory, feasible to be incorporated in a DGVM, which takes into account the information arising from such small-scale surface heterogeneities?

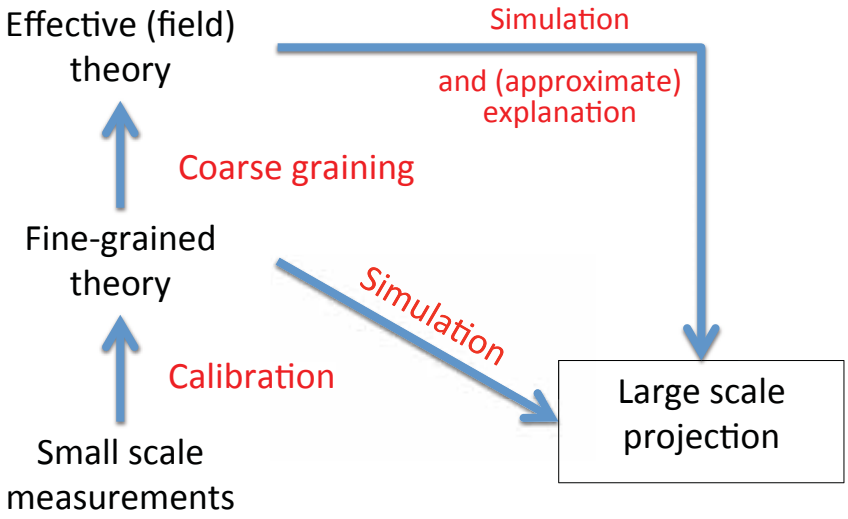

Figure 1.2: A sketch of the methodological framework to tackle scale interactions in complex systems. The construction of an effective theory is fundamental in order to relate small-scale/plot measurements to large-scale/global predictions (DeDeo, 2011). The use of simulations can link also a fine grained theory to full prediction, but the computational costs between the fine and the coarse grained simulation differ substantially, and only the coarse grained is feasible to be considered as (approximate) explanation of the observed phenomenon in a large-scale model.

1.2 Thesis outline

In the three following Chapters I present different approaches to identify and tackle scale interactions in northern environments. I present the different models I developed, and the applications of these novel tools. Each Chapter can be read independently.

In Chapter 2, I present a stochastic model for the polygonal tundra based on Poisson-Voronoi Diagrams. In order to investigate micro-scale (m) effects on the landscape-scale (km) and to compare the model results with local measurements, I developed a stochastic representation of the geometrical features arising from complex crack and growth processes. Geometrical properties of the low center polygonal tundra, such as area of wetter and lower centers and of drier and elevated polygon rims, are well represented, and water table dynamics is in agreement with observations. The small-scale heterogeneities play a fundamental role in consistently representing the landscape-scale properties, such as water and carbon balance. The results of the model presented in this Chapter have been published in Cresto Aleina et al. (2013b).

In Chapter 3, I present a model for the identification of scale interaction issues in another boreal ecosystem, i. e., a typical permafrost-free peatland. I initialize the model with in site measures for micro-topography typical of boreal peatlands. I show how the micro-topography representation controls the water table dynamics. By coupling the micro-topography model with a process-based model for methane emissions, and with a one-box atmospheric model I can quantify effects and feedbacks on greenhouse gas emissions and energy balance from the micro-scale (m, hummocks and hollows) to the landscape-scale (km, the whole peatland).

In Chapter 4, I use the outputs of the model I presented in Chapters 2 and 3 in order to apply a novel analysis method, which makes use of Minkowski functionals and densities (Mecke, 2000). This analysis framework gives information on the landscape-scale pattern generated by the models presented in the previous Chapters. I also show the first steps towards the development of a comprehensive parameterization that takes into account the effects of micro-topography in northern peatlands. Such a parameterization is computationally feasible to be incorporated in a DGVM such as JSBACH, working at an ESM-scale (50-100 km).

In Chapter 5, I summarize the main results and the answers to the research questions, and I draw more general conclusions to the overall problem of scale interactions in boreal ecosystems. I also discuss the main implications of the present thesis for possible research in the future.

Chapter 2

A stochastic model for the polygonal tundra based on Poisson-Voronoi diagrams

Sub-grid processes occur in various ecosystems and landscapes but, because of their small scale, they are not represented or poorly parameterized in climate models. These local heterogeneities are often important or even fundamental for energy and carbon balances. This is especially true for northern peatlands and in particular for the polygonal tundra where methane emissions are strongly influenced by spatial soil heterogeneities. We present a stochastic model for the surface topography of polygonal tundra using Poisson-Voronoi diagrams and we compare the results with available recent field studies. We analyze seasonal dynamics of water table variations and the landscape response under different scenarios of precipitation income. We upscale methane fluxes by using a simple idealized model for methane emissions. Hydraulic interconnectivities and large-scale drainage may also be investigated through percolation properties and thresholds in the Voronoi graph. The model captures the main statistical characteristics of the landscape topography, such as polygon area and surface properties as well as the water balance. This approach enables us to statistically relate large-scale properties of the system to the main small-scale processes within the single polygons.

2.1 Introduction

Large-scale climate and land surface interactions are analyzed and predicted by global and regional models. One of the major issues these models have to face is the lack of

representation of surface heterogeneities at sub-grid scale (typically, less than 100-50 km). How phenomena and mechanisms interact at different spatial scales is a challenging problem in climate science (see e.g. the review of Rietkerk et al., 2011). In particular, the lack of cross-scale links in most general circulation models (GCMs) may lead to miss nonlinear feedbacks in climate-biogeosphere interactions, as highlighted by recent studies (Baudena et al., 2013; Janssen et al., 2008; Dekker and Rietkerk, 2007; Scheffer et al., 2005; Pielke, R. A., Sr et al., 1998). This issue may cause a strong bias in climate models trying to compute accurate energy and carbon balances. This is particularly true for methane emissions in northern peatlands that contribute considerably to the Arctic carbon budget (Baird et al., 2009a; Walter et al., 2006). In addition, thawing permafrost could lead to increased carbon decomposition and enhance methane emissions from these landscapes causing a positive feedback to climate change (O'Connor et al., 2010; Schuur et al., 2008; Christensen, 1995).

One important driver of methane emissions, for example, is water level. In polygonal tundra, the pronounced micro-topography leads to a tessellate pattern of very contrasting water levels and hence strong small-scale variability of methane emissions. Previously, typical process-based wetland methane emission models (e.g., Walter et al., 1996; Walter and Heimann, 2000) were constructed based on plot-scale process understanding and emission measurements but have subsequently been used for upscaling emissions to large areas using a mean water level. With water level often acting as a on-off-switch for methane emissions (Christensen et al., 2003), the problem becomes obvious: where methane is emitted at the inundated micro-sites and not emitted at the dominating relatively drier sites, the mean water level in the model can either be near the surface (as in the inundated sites), leading to large emissions throughout the area, or it can be below the surface (as in the moist sites) leading to emissions close to zero. Both results would not represent the differentiated emission pattern of the polygonal tundra, also because water table position in respect to the ground surface is nonlinearly related to methane emissions. Zhang et al. (2012) also used a process-based model to upscale methane emissions from the plot to the landscape-scale but ran the model separately for each land surface class as derived from high-resolution aerial imagery. This approach leads to a much better agreement with landscape-scale emissions as measured by eddy covariance than previous upscaling attempts with process-based models that ignored the spatial heterogeneity. The model representation of such heterogeneity is currently usually driven by the pixel size of available remote sensing products or the grid cell size of the respective model, but the real world functional or structural differences between individual components of a heterogeneous domain may actually be on a very different scale. Preserving their information content becomes particularly im-

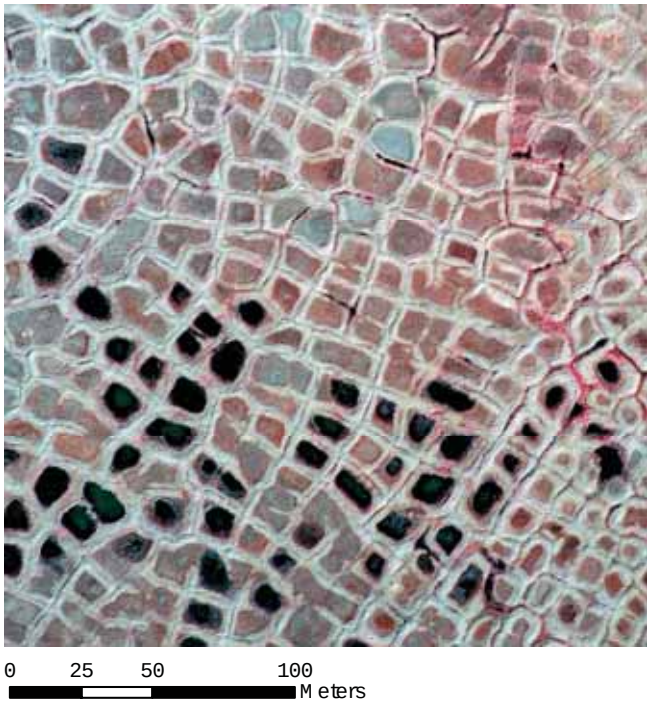

Figure 2.1: Color-infrared aerial picture of polygonal tundra on Samoylov Island, Lena River Delta, Russia. Dry rims appear light grey, open water appears black. Dark grey and reddish areas indicate moist to wet areas.

portant where nonlinear relationships are involved in the represented processes such as those driving greenhouse gas emissions (Stoy et al., 2009; Mohammed et al., 2012).

Arctic lowland landscapes underlain by permafrost are typically characterized by patterned ground such as ice-wedge polygonal tundra. They cover approximately 5-10% of Earth's land surface, where they play a dominant role in determining surface morphology, drainage and patterns of vegetation (French, 2007). Low center polygonal tundra typically consists of elevated comparatively dry rims and lower centers that can become wet if the water table rises to the ground surface level or above. Thermally induced cracking in the soil during winters with large temperature drops generates the polygonal patterned ground. When the temperature rises and snow cover melts, water infiltrates in those cracks, and refreezes. Over the years, as this process is cyclically iterated, the terrain is deformed due to the formation of vertical masses of ice, called ice-wedges. Aside of the wedges, terrain is elevated because it is pushed upwards, forming the elevated rims typical of this landscape. Incoming water (precipitation or snow melt) is then trapped by the rims in the polygon center, resulting in a water table level which dynamically responds to climate and weather. This environment is typical for high-latitude permafrost areas of Alaska, Canada, and Siberia. Ice-wedge polygon features

have been observed also on Mars (Haltigin et al., 2011; Levy et al., 2010). The surface morphology of dry rims and wet centers determines drainage and vegetation patterns in the polygonal landscapes. They have therefore been the focus of extensive field studies on experimental sites on Samoylov Island in the Lena River Delta in Siberia (an aerial picture of the study site is shown in Fig.1). Previous works involved closed-chamber and eddy covariance measurements of methane fluxes (see e.g. Sachs et al., 2008, 2010; Wille et al., 2008; Kutzbach et al., 2004), as well as measurements and modeling of hydrological properties (Boike et al., 2008), and of surface energy balance (Langer et al., 2011b,a) in this typical periglacial landscape. Recent studies with the help of remote sensing data were able to capture and analyze surface heterogeneity (land cover and surface temperature) and its importance for the land-atmosphere water fluxes (Muster et al., 2012; Langer et al., 2010). Theoretical efforts have also managed to quantitatively classify ice-wedge polygons and other permafrost patterns in Alaska using Minkowski density functions, quantifying binary patterns from aerial photographs. (Roth et al., 2005).

In general, stochastic models may be useful tools to link different scales. Such an approach has been widely used in modeling physical, biological, and ecological phenomena, seeking to represent only the main processes and observable properties, and replacing complex dynamics with random processes (see e.g. Dieckmann et al., 2000, and references therein). To model large-scale (e.g., 100 km^2) seasonal dynamics of the small-scale-driven greenhouse gas emissions from such a landscape, it is impossible to limit the description to an accurate model for a single polygon (typical dimensions in the order of 10 m in diameter), due to the wide internal variability of the landscape. In particular, this mechanistic approach would require a large number of parameters and computational power in order to represent polygon variability in size, water table position with respect to the surface, and response to climatic forcing. In this work, we provide a stochastic method that takes into account such variability, using properties of Voronoi polygons.

Voronoi diagrams (or *tessellations*) have been applied to various fields, from astronomy to biology, forestry, and crystallography. For comprehensive reviews, see e.g. Lucarini (2009), Okabe et al. (2000), and reference therein. Their wide range of applications derives from the fairly simple concept of partitioning the space behind them and from their adaptability. In ecology and Earth science, they have been used to describe ecological subdivision of territories (Hasegawa and Tanemura, 1976), hydrology and precipitation, geology, and recently also as a framework in order to integrate climatic variables over an irregular geographic region (Lucarini et al., 2008).

2.2 The model

We develop a stochastic model, which is able to reproduce the main statistical characteristics of the low center polygonal tundra (i.e., surface topography, area of different soil surfaces, water table height). With the present model we do not seek to explain surface pattern formation: our aim is, instead, to find a robust way to upscale land-atmosphere greenhouse gas fluxes and the landscape response to climatic forcings that are coupled to these statistics. We limit our description to the landscape's present-day state, and we do not represent polygon formation nor degradation.

We tessellate the plane with random polygons which are able to reproduce the main general features of ice-wedge polygons. The model represents, analyzes and considers the statistical characteristics of a region covered by ice-wedge polygons and describes the landscape-scale (about 1 km^2 or more) response to climatic forcing. In order to represent ice-wedge polygonal tundra we use a random tessellation of the plane, so-called Poisson-Voronoi diagrams (Okabe et al., 2000).

2.2.1 Poisson-Voronoi diagrams

Let us populate a Euclidean plane with an at most countable number of distinct points. We then associate all regions in that space with the closest member(s) of the point set with respect to the Euclidean distance. The result is a set of regions that cover the whole plane, and each one of them is associated with a member of the generating points. This tessellation is called planar ordinary Voronoi diagram, generated by the point set. The regions constituting the Voronoi diagram are the Voronoi polygons. More rigorously, let $P = \{\mathbf{x_1}, \ldots, \mathbf{x_n}\}$ be the generating point set, where $2 \leq n \leq \infty$ and $\mathbf{x_i} \neq \mathbf{x_j}$ for $i \neq j$, with i and j integers. The (ordinary) *Voronoi polygon* associated with $\mathbf{x_i}$ is defined as:

$$V(\mathbf{x_i}) = \{\mathbf{x}| \parallel \mathbf{x} - \mathbf{x_i} \parallel \leq \parallel \mathbf{x} - \mathbf{x_j} \parallel, i \neq j\} \tag{2.1}$$

and the set given by

$$\mathbf{V} = \{V(\mathbf{x_1}), ..., V(\mathbf{x_n})\} \tag{2.2}$$

is the Voronoi tessellation. In our case, the generating process P is a homogeneous Poisson point process $P(\lambda)$, where λ is the intensity of the process. Therefore, we call the resulting tessellation a *Poisson-Voronoi diagram* (PVD). Parameter λ basically controls the density of the Poisson process. On a square $L \times L$, the intensity of the

process is defined as:

$$\lambda = \frac{E[n]}{L^2} \tag{2.3}$$

where $E[n]$ is the mean of the number n of generated points, which follows a Poisson distribution. Parameter λ directly regulates the polygon sizes. We tuned this quantity with data from image analysis of the landscape (Muster et al., 2012). From equation (2.3), $L = 1$ km and $\lambda = 7500$. Since $\lambda L^2 \gg 1$ we are in the thermodynamic limit and the boundary effects can be neglected. A model realization of PVD is shown in Fig. 2.

The area of polygons in a Poisson-Voronoi diagram has been widely analyzed by numerous studies (Okabe et al., 2000). Direct numerical investigations showed that 3-parameter generalized gamma distributions fit quite well the statistical properties of the PVD (Miles and Maillardet, 1982):

$$f_A(x) = \frac{r b^{\frac{q}{r}} x^{q-1} e^{-bx^r}}{\Gamma\left(\frac{q}{r}\right)},\ r > 0,\ b > 0,\ q > 0. \tag{2.4}$$

Other distributions have also been used in the literature to describe the PVD area distribution such as lognormal and 2-parameter gamma (from equation (3.31), one obtains the 2-parameter gamma distribution if $r = 1$), as reported by Okabe et al. (2000) and reference therein.

2.2.2 Idealized polygons

Ice-wedge polygons are composed of two main regions: elevated drier rims and lower wet centers. In our model:

$$A_{pol} = qA_{pol} + (1 - q)A_{pol} = r + C \tag{2.5}$$

where A_{pol} is the total polygon area, and r and C represent the area covered by elevated rims and the one covered by low centers respectively. Parameter q is a random quantity varying between 0.35 and 0.7, which we tune according to observation data (Muster et al., 2012).

Each Voronoi-region represents an ice-wedge polygon and its vertical structure consists of a column, which parameterizes the water table level W_t, the thaw depth TD, and the low polygon center surface level S. Water table is a dynamical variable and responds to climatic forcing, whereas thaw depth follows a prescribed behavior during the seasonal cycle (see Section 2.3 for the parameterization dynamics). Surface level, polygon depth, thaw depth and water table level are initialized randomly: we tune their

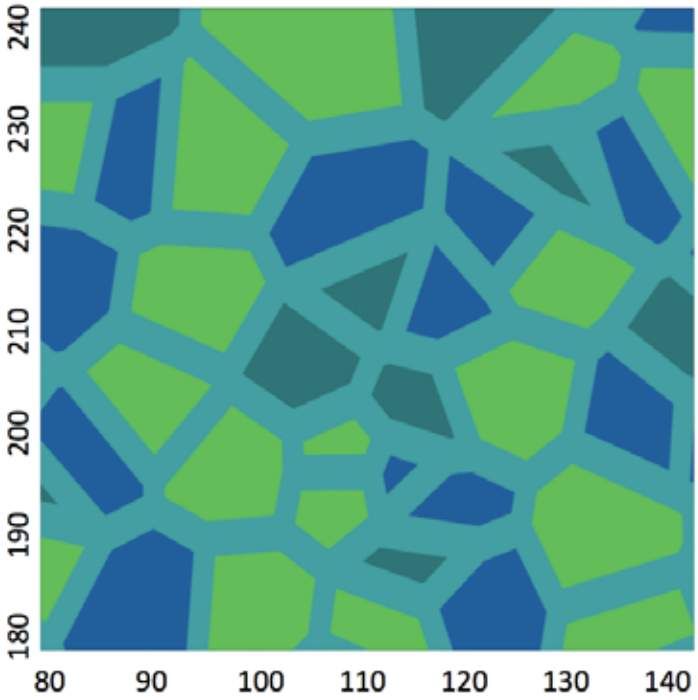

Figure 2.2: Poisson-Voronoi diagrams: different colors represent different types of surfaces: light green if the polygon center is moist (water table >10 cm below the surface), dark green if it is saturated (water table < 10 cm below as well as < 10 cm above the surface) and blue if it is wet (water table > 10 cm above the surface and the polygon is covered by open water). Dimensions of polygon edges in the figure are not to scale, since in our model they cover up to 70 % of the whole polygon area. Distances on x and y axes are in meters.

mean values with data from available field observations. All quantities are computed from the top elevation of rims, as shown in Fig. 3.

If water table rises above the center surface, area C increases as well, following the equation:

$$C' = \pi \left(\sqrt{\frac{C}{\pi}} + \frac{\delta W}{\tan \alpha} \right)^2 \tag{2.6}$$

where C' is the polygon center area after the water table rise δW and α is the angle between elevated rims and polygon center surface, parameterized as:

$$\alpha = \frac{\pi}{4} \log(10q)$$

which takes into account that the larger the rims, the steeper polygon walls become, as suggested by observations. Factor $\frac{\pi}{4}$ is needed not to exceed the limit $\alpha_{lim} = \frac{\pi}{2}$.

Computing water table (W_t) variations with respect to the polygon surface (S) is essential to estimate methane emissions (Sachs et al., 2008; Wille et al., 2008; Kutzbach

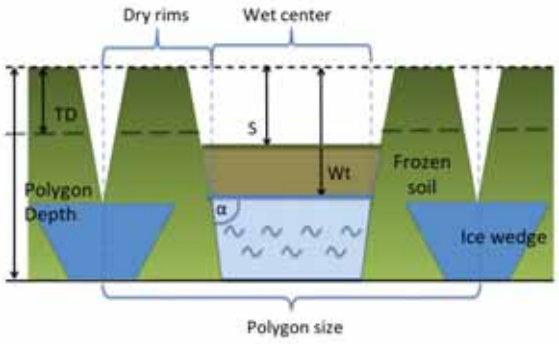

Figure 2.3: Cross section of a polygon. Surface is divided in drier elevated rims and in lower wet centers. Both surface level and single polygon depth are randomly generated. Water table level W_t and thaw depth TD are also randomly initialized but they dynamically variate with external forcing (W_t) and seasonal cycle (TD). Angle α represents the slope of polygon rims.

et al., 2004). We distinguish between three kinds of surface types, depending on the position of the water table with respect to the polygon center surface. If:

$$\begin{aligned} S - W_t > \epsilon \quad &\Rightarrow \quad \text{Wet centers} \\ |S - W_t| \leq \epsilon \quad &\Rightarrow \quad \text{Saturated centers} \\ S - W_t < -\epsilon \quad &\Rightarrow \quad \text{Moist centers} \end{aligned}$$

where threshold $\epsilon = 10$ cm has been inferred from observations of small-scale methane emissions (Sachs et al., 2010). They are controlled by the site's water table height, and different surface types correspond to different emitting characteristics. In particular, methane emissions from saturated centers are an order of magnitude larger than in the case of moist centers or than emissions from dry rims.

2.2.3 Water table dynamics

We simulate water table variations at each time step (i.e., each day). The time period we are looking at is the summer season (namely, from beginning of July till the end of September), when the snow has already melted, and thaw depth deepens. The prognostic equation for water table dynamics is:

$$\frac{dW_t}{dt} = \frac{P_{eff} - ET - R}{s} \tag{2.7}$$

where water table height W_t responds dynamically to effective precipitation P_{eff}, evapotranspiration ET, and lateral runoff R. Parameter s represents the drainable porosity. We compute water table variations for each polygon at each time step. Water table position is then related to surface characterization, as described in the above paragraph. Since we only focus on the effect of surface heterogeneity on GHG emissions, precipitation and evapotranspiration are parameterized as uniform over the whole area, i.e. we do not apply any downscaling of climatic forcing. In particular, the two variables follow a simple random parameterization. In this way, we are able to simulate both dry and wet summers. We also take into account that the water income in polygon centers does not only depend on precipitation income directly on the area C (Eq. 2.5), but some of the precipitation falling on the rims r also percolates through the soil and has an impact on the water balance. In particular, we assume that half of the precipitation falling on the rims percolates or flows to the polygon centers. We therefore consider an additional water income term. We generate a random number of rainy days (between 5 and 35). If the day t is a rainy day ($r.d.$), then:

$$P_{eff} = P\left(1 + 0.5\frac{r}{A_{pol}}\right) - \Delta S_t. \tag{2.8}$$

Where precipitation P is defined as:

$$P = \begin{cases} R_p \sin(\frac{t+T}{6T\pi}) & \text{if } 30 < t < 90 \\ 10\frac{\text{mm}}{\text{day}} \ \sin(\frac{t+T}{6T\pi}) & \text{else} \end{cases} \tag{2.9}$$

where R_p is a randomly generated number, which tunes the amplitude of precipitation events in the part of the summer season when main precipitation events are supposed to occur, and it is computed in mm/day. In particular, changing R_p changes drastically the amount of incoming water. $T = 30$ days is hereinafter a time constant. Term ΔS_t represents the amount of water stored in the unsaturated terrain in the rims that does not contribute to water table variations at each time step. After large precipitation events, not all the precipitation flows from the rims to the water table centers, but part of it fills the unsaturated terrain of the elevated rims. This water balance term has been observed in field campaigns and it is supposed to have a stronger influence at the beginning of our simulation time slice (July), when the upper layer of the soil is unsaturated, whereas storage capacity decreases with time until the whole terrain is

saturated. In our model we parameterize storage as an exponential function:

$$\Delta S_t = \begin{cases} (P - ET)e^{-\frac{t}{\tau}} & \text{if } P \geq 15 \text{ mm/day} \\ 0 & \text{else} \end{cases} \tag{2.10}$$

where t is time and $\tau = 45$ days is the characteristic time at which ΔS is reduced to $(P - ET)/e$. We assume precipitation and evapotranspiration to be uniform over the center and the rims.

We parameterize ET as:

$$ET = ET_p \sin(\frac{t+T}{6T\pi}) \tag{2.11}$$

where ET_p follows:

$$ET_p = \begin{cases} 5 \text{ mm d}^{-1} & \text{if } t = r.d. \text{ and } 30 < t < 90 \\ 2.5 \text{ mm d}^{-1} & \text{if } t = r.d. \text{ and } (t < 30 \ \vee \ t > 90) \\ 2 \text{ mm d}^{-1} & \text{else} \end{cases} \tag{2.12}$$

We chose parameterization of ET and P in order to reproduce data from observation campaigns from Boike et al. (2008) and Langer et al. (2011a), which describe how evapotranspiration is linked to the landscape's energy balance.

Thaw depth, on the other hand, follows a seasonal trend: its level depends on the time of the year the model is run at. With progress of the summer, the depth of the seasonally thawed layer (frost table depth) increases, reaching its maximum at the beginning of September. We keep thaw depth dynamics prescribed, i. e., we do not consider how temperature variations may affect the environment. From available observations, we assume thaw depth to behave as follows:

$$TD = \begin{cases} 15\frac{t}{T} \text{ cm} & \text{if } t < 30 \\ \left(15 + 20 * \sqrt{\frac{t-T}{T}}\right) \text{ cm} & \text{if } 30 < t < 90 \\ const & \text{else} \end{cases} \tag{2.13}$$

During spring/early summer the ground is still frozen and water is kept inside the polygons. With progression of thaw depth during summer, neighboring polygons can become hydraulically connected. Field experiments show that water, which was retained inside a polygon by the frozen elevated rims, may in this situation slowly flow through the active layer of the rims themselves, from one polygon to another one or from polygon center to the ice-wedge channel network (Boike et al., 2008). This phenomenon is important for the water balance: in this case we assume a constant drop

of the water table because of lateral runoff R:

$$R = \begin{cases} 3 & \text{if } W_t < TD \\ 0 & \text{else} \end{cases} \tag{2.14}$$

where R is computed in mm/day. Physically it represents both surface and subsurface runoff.

We also consider that, due to soil porosity and water holding capacity, water table rises differently inside and above the soil. We assume drainable porosity s to be 0.7 if $S - W_t < 0$, and 1 if $S - W_t \geq 0$. We base this assumption on field studies (Helbig et al., 2013; Langer et al., 2011a).

We integrate the model for 90 days, which is approximately the duration of the thaw season in northern Siberia (July-September). Our model does not include cold months, when the surface is covered by snow. We also do not consider early summer, when the thaw depth is still limited. External climatic forcings are precipitation and evapotranspiration. We can vary precipitation intensity and its seasonal amount by tuning parameter R_p (Eq. 4.15). In our simulation, we use: $R_p = 30$ mm/day for a *standard* scenario, $R_p = 15$ mm/day for a *dry* scenario and $R_p = 60$ mm/day for a *wet* scenario. For each scenario, we perform ensemble simulations, calculate the average of 30 ensemble members, and compute water table dynamics. We finally derive variations on the amount of landscape area covered by different surface characteristics (i.e., moist centers, saturated centers or wet centers).

Many studies showed the relationship between water table height and methane emissions, such as Couwenberg and Fritz (2012); Zona et al. (2011); Sachs et al. (2010); Strack (2004). In order to give an example of the influence of water table and surface wetness on methane fluxes accounting for different climatic forcing, we multiply the area covered by moist, saturated, or wet centers by values which represent the average August methane emissions from each surface type (Sachs et al., 2010). Average methane flux (in mg d^{-1}) from the total region at each daily time step is computed following the equation:

$$F_{tot} = \sigma C_{saturated} + \omega C_{wet} + \delta(C_{moist} + r) \tag{2.15}$$

where $\sigma = 94.1$ mg d^{-1} m^{-2}, $\omega = 44.9$ mg d^{-1} m^{-2}, and $\delta = 7.7$ mg d^{-1} m^{-2}. Values are taken from Table 4 of Sachs et al. (2010). Area C_i of polygon centers with different wetness and area r of relatively dry rims are computed in m^2. In this simple model, we assume polygon rims and moist centers to have the same emission coefficient δ.

2.2.4 PVD and percolation theory

Mathematical properties of PVD are also well suited to describe some landscape-scale physical processes that have been observed in the field. In particular, we focus on interconnectivity properties of the graph, applying percolation theory on PVD.

When water flows from polygon centers through the unfrozen top layers of the rims (lateral runoff), it starts to flow into channels on top of the ice wedges between the polygon rims (visible in Fig. 1). Due to thermal erosion, water does not stay confined in the channel, but flows through a path of interconnected channels. If this path of channels is large enough to connect polygons from one side of the landscape unit of consideration to the other one, we can assume that water in the channels is able to flow from one side to the other one. The system tested in this study is an island. Consequently, water which was previously confined in the channels would likely run off the island to the Lena river nearby. In our model we assume interpolygonal channels (polygon edges in the PVD, or bonds, in percolation theory) to be *active* if the polygon experiences lateral subsurface runoff. We also assume the polygon channel system to be flat, or with a very small topological gradient, so that outflow due to landscape slope is negligible.

Percolation theory describes the behavior of connected clusters in a random graph: since its introduction in the late fifties (Broadbent and Hammersley, 1957), it has been widely and successfully applied to a large number of fields, from network theory to biological evolution, and from galactic formation to forest fires (Grimmett, 1999, and references therein). Originally, the question to be answered focused on transport in porous media. Let us imagine a porous stone touching some water on a side: what is the probability that the water passes through the whole stone, coming out at the other side? This simple question led to a basic stochastic model for such a situation and gave birth to percolation theory. In our model, the question would be: what is the probability that an open path of interconnected *channels* is formed? This is in fact the probability that a giant cluster of channels with flowing water appears. On the PVD, *bonds* connecting two points of the graph represent channels. Water flowing through rims enters the channel network generated above the ice wedges between the polygons. These channels are underlain by ice-wedges, and water flowing through them may also cause thermo-erosion because of its mechanical and thermal effects on flowing water on ice. In our simple model, if a channel is filled by water, we call it *active*. Since we assume the environment not to have any slope, all edges of a polygon with $W_t < TD$ become *active* at the same time.

Percolation theory focuses on the probability $\theta(p)$ that a giant cluster exists. This

probability is non zero only if the probability p that a bond is active exceeds the critical threshold values p_c. This value depends on the graph. Recent studies (Becker and Ziff, 2009) determined numerically the bond percolation threshold p_c on a PVD:

$$p_c = 0.666931 \pm 0.000005$$

In order to reach percolation, the condition $W_t < TD$ must be reached in a large enough number of polygons. We simulate this result by keeping the thaw depth constant and increasing the water table. We do not consider any physical process involved in water table change, but we keep increasing its level until we reach the percolation threshold.

2.3 Results and discussion

In this section we analyze environment statistics by comparing model outputs with available observations, both from field and from aerial photography. We analyze the geometric characteristics of the polygonal tundra and the ones of PVD. We then present and discuss results from 90 days of simulations, and the water table dynamics in different simulated scenarios. Finally, we show results from our bond percolation realization. Our results are qualitatively different from a mean field approximation approach, since mean water table variations are computed considering processes taking place in each single polygon.

2.3.1 Polygon statistics

We are interested in the distribution of areas covered by polygon centers $C = (1-q)A_{pol}$. As for the polygon area A_{pol}, we compare the histogram of model output for C with a generalized gamma distribution f_A and a 2-parameter gamma distribution. Both distributions are accepted by a Kolmogorov-Smirnov test at a 0.05 level of confidence. Parameters of the distribution are taken from literature concerning the polygon area distribution in a PVD (Okabe et al., 2000, and reference therein). Lognormal, exponential, and normal distributions are rejected by the test for both A_{pol} and C.

We then proceed to compare the model results with available data for the ice-wedge polygons (Muster et al., 2012). We tuned the controlling parameter of the point process λ and the random parameter q (equation 2.5) with observed mean values of polygon and polygon center areas. Results show that comparisons between model outputs and data are quite robust: not only the first two statistical moments are comparable, but

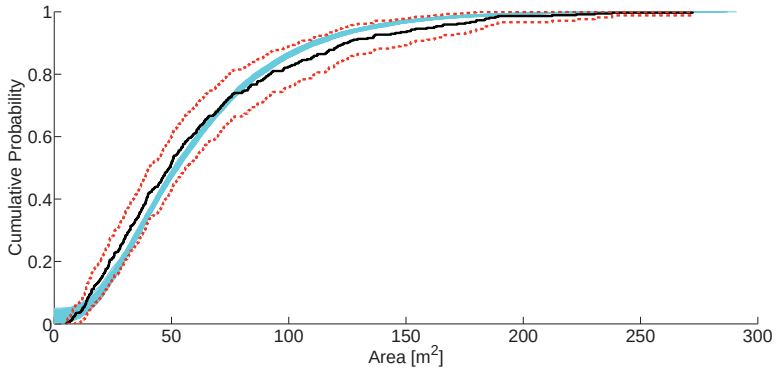

Figure 2.4: Cumulative probability distribution of polygon center sizes. Observations (blue line), and 100 model realizations (cyan lines) are compared. The figure displays area on the x axis. Mean size of center area is 61.19 m^2 in the observations and 61.36 m^2 in the model on. These values are comparable as confirmed by a Student's T test. Distribution and standard deviation of data and model output are also comparable. Red lines represent the confidence bounds for the data cumulative distribution function at a 0.01 confidence level.

they also display a very similar distribution (as confirmed by a χ^2 test at a 0.05 level of confidence).

This result is central in our approach: it shows that PVD description of the landscape statistics is consistent with observations. In particular, we claim that our approach is able to consistently capture the topographic features of the landscape we analyze. Even though the PVD are generated by a completely stochastic process (Poisson point process), they represent area distribution of such a complex environment as the low-center ice-wedge polygonal tundra. In order to test the robustness of this result, we performed simulations on an other less random tessellation, i.e. a regular square lattice, with polygon area A_{pol} equal to the mean area from observation data (136 m^2). Again, polygon center area $C = (1-q)A_{pol}$, with parameter q defined in the same way as for the random case. Even though mean polygon and polygon center areas have been tuned with observations, results do not fit polygon center distributions and fail in particular to capture the skewness of the distribution, being therefore rejected by Kolmogorov-Smirnov test.

2.3.2 Response to climatic forcing

Precipitation and evapotranspiration are the main inputs and outputs that drive water level dynamics as described in equation 2.7. In order to test the model response to drier and wetter conditions, we simulate different configurations by changing the amount of incoming precipitation. We then compare the cumulative precipitation simulated by the

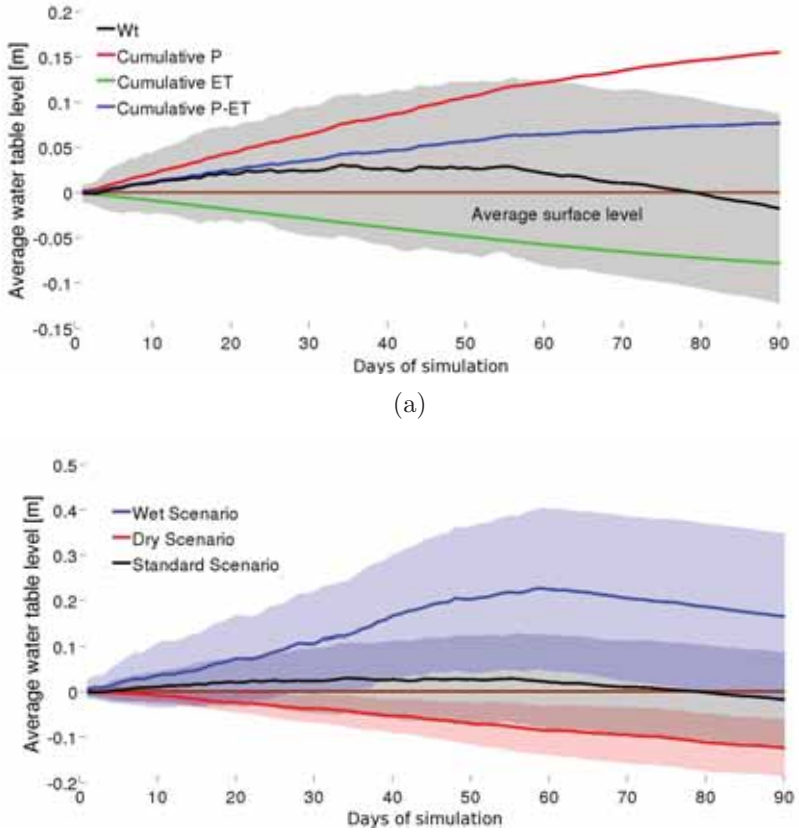

Figure 2.5: Ensemble averages of 30 model simulations. The graph in panel (a) displays water table variations over time. Assuming no runoff, and storage term equal to zero, water level should correspond to the blue curve (cumulative precipitation minus cumulative evapotranspiration). Field datasets clearly show a drop in water table at the end of the season, due to lateral runoff, when water table lies above the thaw depth. Panel (b) shows water table dynamics in the three simulated scenarios: *wet* (blue line), *dry* (red line), and *standard* (black line). Shaded areas represent the variance of the ensemble simulations, which increases with the increase of the amount of water input.

model and the one measured in the field in order to have realistic scenarios comparable with data from field campaigns (Boike et al., 2008; Sachs et al., 2008). Field studies observed in particular the influence of lateral runoff and storage: water table drops in the late summer season, since water table usually lies above thaw depth, and it leads to lateral fluxes of water in the ice-wedge channel network. The model captures this process (Fig. 5) as well as the water table variation magnitude.

Model results show that a decrease in precipitation will lead to a drastic drop in the water table level, due to lateral runoff (Fig. 5b). Precipitation income is the only input in equation 2.7. Scenarios of such dry seasons are likely to lead to drastically drier soil conditions in the polygonal tundra landscape if there is not a parallel decrease in mean

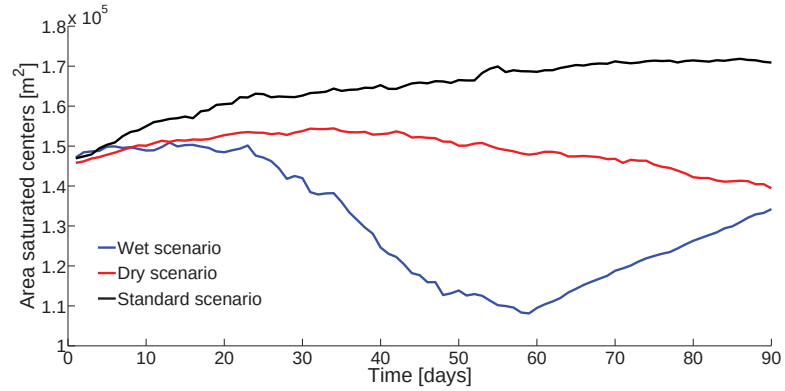

(a)

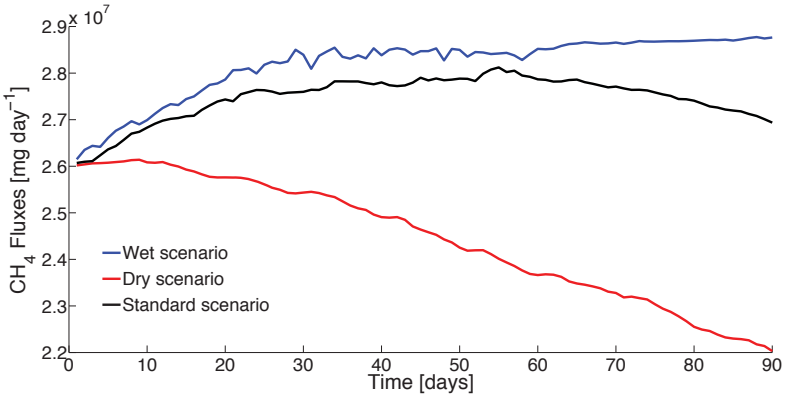

(b)

Figure 2.6: Ensemble averages of 30 model simulations in different scenarios. Panel (a) displays seasonal variations of area covered by saturated centers in a *wet* (blue line), *dry* (red line), and *standard* (black line) scenario. Saturated centers represent the major contribution to methane emission in this area, and in our model their total area drops in both *dry* and *wet* scenarios. Panel (b) shows modeled total methane emissions from the whole landscape in the three scenarios. Despite a decrease in the number of high-emissive saturated centers, our simple model shows increased methane emission in the *wet* scenario because of a drop in the area covered by the relatively drier tundra (moist centers and elevated rims).

surface temperature, and consequently in thaw depth behavior. On the other hand, an increase in precipitation with respect to the reference value used in the *standard* scenario will not cause a flooding of the landscape. In the *wet* scenario we perform simulations with a mean seasonal increase in precipitation of 100 mm/year with respect to the reference value. In agreement with observations, mean water table changes its position by lying slightly above the average polygon surface (i.e, $W_t < \epsilon = 10$ cm).

Depending on W_t position in respect to the surface of the polygon center, soil characteristics in polygon centers vary from moist to saturated and wet conditions.

Field studies in this region showed a link between water table position and emissions of greenhouse gases, with respect to methane (Kutzbach et al., 2004; Sachs et al., 2010) and latent heat fluxes (Langer et al., 2011b; Muster et al., 2012). In particular, methane fluxes vary up to an order of magnitude among different surface types. Therefore dynamics of water table also influences dynamics of GHG emissions. Once again, temperature variations and influences on thaw depth seasonal behavior are neglected. If mean surface temperature rises, we expect lateral runoff to start earlier in the season and therefore to be able to drain more water away from the environment. In our *wet* scenario precipitation further increases. In this case, runoff is not sufficient to balance the excess water, and the area covered by wet centers increases.

Our model is also able to calculate the seasonal dynamics of the landscape area covered by moist centers, saturated centers, and wet centers. These results are dependent on thaw depth dynamics, which we here assume prescribed. Overall, in the ensemble averages of simulations in the three different scenarios we used for precipitation input, the fraction of area covered by saturated centers shows little seasonal dynamics if compared to the fraction of surface covered by wet and moist centers. According to our model, during the summer only extreme drops in water table, or very wet summers would lead to significant modifications of the fraction of the landscape covered by saturated centers. We argue though, that coupling our simple approach to available permafrost models, and thus with thaw depth behaviors dependent on climatic and environmental conditions, would enable more realistic predictions in different scenarios. In particular, in warmer conditions, soil could thaw deeper and earlier in the season, leading to further drops in the water table level and in the fraction of the landscape covered by different terrains.

The simple model here introduced for computing methane emissions is directly related to changes in soil wetness. We show the results of ensemble simulations in different scenarios in the second panel of Fig. 5b. In particular, we observe that a decrease in precipitation (*dry* scenario) leads to a parallel decrease of methane emissions with respect to the *standard* case, mainly because of spreading of relatively drier tundra, which presents lower methane fluxes than wet and saturated centers. Water table decreases and more and more centers become drier. According to equation (2.6), the area of the lower centers decreases at the same time, thus increasing the area covered by rims r, which in our model have the same emission properties of drier centers. If precipitation increases, our model predicts a corresponding increase in methane emission from the landscape. In this extreme case, a more elevated water table would lead to an increased number of wet centers, causing a retreat of the relatively drier tundra. Even though area covered by high-emissive saturated centers decreases, in fact, the decrease

of surface covered by relatively drier centers is even larger. This situation is likely to increase methane emissions in respect to the *standard* scenario. In the *wet* scenario, however, the decrease in the area covered by moist centers is counterbalanced by the decrease of area covered by saturated centers in favor of wet ones. Therefore, methane emissions, even if, as expected, larger in the *wet* scenario, do not increase significantly. Our results are only qualitative, since we assume only a fixed average value for the seasonal methane emissions. It is worthy to mention that the order of magnitude of the methane emission is the same as the one found in eddy covariance measurements in the study site (Sachs et al., 2010). This finding has been obtained without any fine tuning and with a very simple methane emission model (Eq. (15)), but it nevertheless proves the goodness of the model.

2.3.3 Percolation threshold

Fig. 7 shows a bond percolation realization. We reach the bond percolation threshold by increasing the water table with a constant thaw depth. More and more polygons experience lateral runoff. Consequently, their channels become *active* and water flows into the channel network. The number of *active* channels needed to reach bond percolation is given by the theoretical findings described above, and it increases with a rising water table. We expected the system to reach the percolation threshold if the average water table level lies above the thaw depth, but the correlation between these two phenomena is not trivial. In particular, the system does not reach the percolation threshold at the same time as the average water level is above the average surface. In the real system, if an interpolygonal channel is *active*, i.e. filled with water, water would not stay confined in it, but would spread to other empty channels because of gravity. This means that as only single polygons show lateral runoff, this drainage water would be distributed to a certain number of other topographically connected channels, thus the overall increase of water level within the channels would be dampened. If many polygons experience lateral runoff, the number of empty channels would be drastically reduced. The water of the *active* channels could then spread in fewer channels. Therefore, the average water level within the channel network would increase. In this case, if a physical threshold somehow analogous to the percolation threshold on the PVD would be reached, the water which was confined in the network channel is likely to flow out of the system, namely into a near river, or sea. This phenomenon may also have a significant impact on the carbon balance of the system since the outflow of water from the channel is one of the most important phenomena for the exchange of DOC (dissolved organic carbon) and DIC (dissolved inorganic carbon). Improving

those features could be a future development of our approach, and the focus of further studies, more specifically interested at landscape-scale processes of periglacial environment. Nevertheless, a simple application of mathematical properties of PVD is able to capture landscape-scale behavior of the system. In particular, the number of polygons needed to reach outflow can be easily computed through a bond percolation model. At this stage, water can flow from the system into a near river, or to the sea and would be lost. Consequences of strong runoff events are ignored in our model but field observations suggest that thermoerosion and water runoff could be agents for polygon degradation. We argue that the ability of PVD to simulate a physical process through critical thresholds enhances the power and the theoretical predictive capability of our approach.

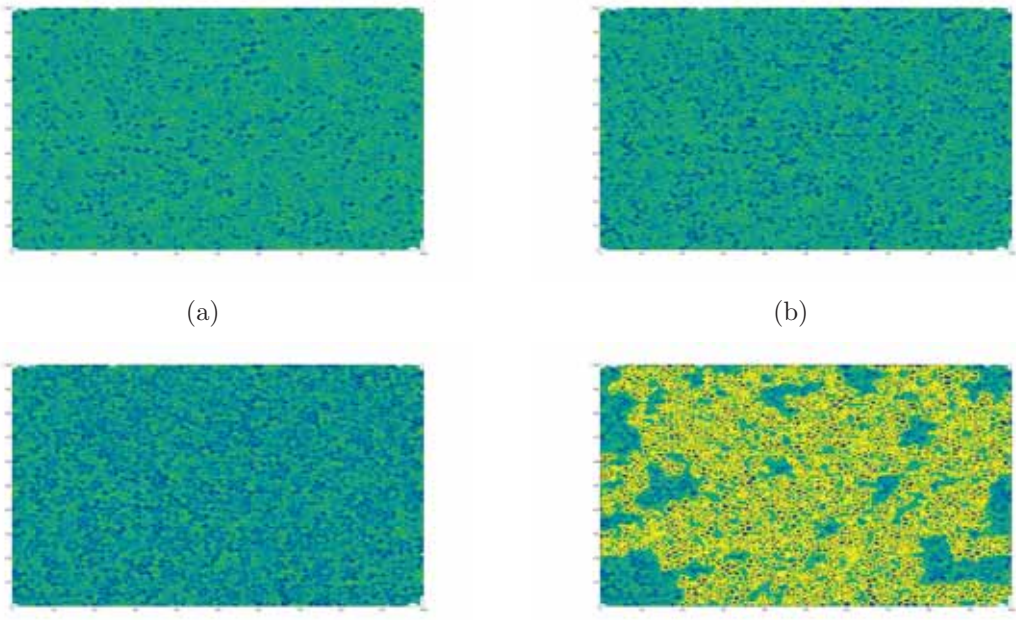

(a) (b)

(c) (d)

Figure 2.7: Bond percolation realization: increase of W_t level and decrease of thaw depth cause interpolygonal flow of water. Water flows into ice-wedge channel network, generated by crack processes. In our model, channels become *active*, and polygons with $W_t > TD$ are colored in blue. In panels (a) to (d), the thaw depth becomes deeper and deeper. This process happens seasonally, and with the deepening of the thaw depth, more and more channels become active, until a certain threshold is reached (panel (d)), when an open path of interconnected active channels appears. The open path is colored in yellow, and it crosses the whole region: water can flow from channels in the middle of the region to its borders as outflow, and it is not kept in the environment any longer.

2.4 Summary and conclusions

Our model provides a simple, stochastic, and consistent approach to upscale the effect of local heterogeneities on GHG emissions at the landscape-scale. In particular, we show how applications of Poisson-Voronoi diagrams can statistically represent the main geometric and physic properties of the low-center ice-wedge polygonal tundra.

We describe the landscape using Poisson-Voronoi diagrams, tuning model characteristics with field data. We show that the probability density function of modeled polygon center areas is consistent with the one inferred by observations. Our approach is therefore able to statistically upscale the terrain geometrical characteristics.

Dynamical water table variations in respect to the polygon surface are essential to compute methane fluxes, and we compute such variations during the summer season over the whole region, parameterizing processes within the single polygons. Results of water table dynamics agree with observations. In particular, the stochastic model is able to represent the water balance over the whole landscape. The model relates then the water table position to different soil wetness levels. In particular, we are able to compute for each time step the fraction of the landscape covered by moist tundra (moist centers and polygon rims), saturated centers, and wet centers, under different climatic forcing.

Our modeling framework enables us to investigate effects of large-scale interconnectivity among ice-wedge channel network. Applications of percolation thresholds on the PVD suggest possible explanations for water runoff from the landscape.

The stochastic parameterization of our model is far from the precision and accuracy of a mechanistic model. Mechanistic models, however, can reach accuracy only at the local scale whereas our approach accounts for landscape-scale properties and processes. Our presented approach could be further improved by including parameterization of hydrology, characterization of ice wedges and phenomena like thermokarst and polygon degradation. In particular, we argue that linking this approach with available permafrost models would enable even more realistic predictions of water table position and the seasonal development of different surface types. Both variables are fundamental to consistently predict GHG emissions from polygonal tundra.

This model shows a new approach that could be successfully applied to other environments and ecosystems where local processes and micro-topography play an important role and a mean field approximation would fail in estimating large-scale features. In order to achieve this goal, we need to gather information on the micro-topography of the environment to which the tessellation approach will be applied. For environments

such as peatlands, for instance, a characterization of the surface elevation (namely, the amount of surface covered by lawns, hummocks, and hollows) in respect to the water table is essential. In order to proper model other ecosystems, the point process generating the tessellation, which in the present study is a stochastic Poisson point process, could also be substituted by a more regular one. For such a development, it is necessary to adapt the vertical structure and the hydrology parameterization of the model (which now represents polygonal tundra) to the new system under consideration. We show such development in the next Chapter.

Flow network techniques, along with more information on the interpolygonal channel characteristics gathered in the field, could be useful tools to estimate and predict the water flow in the channel network.

Further work will be focused on linking the stochastic model to existing mechanistic surface models, such as Land Surface Schemes (LSS). We think that using the model as an external module for characterizing surface micro-topography will improve the variance of the mechanistic model, leading therefore to a qualitative improvement of the mean field approximation for water table level, energy balance and greenhouse gas emissions. One way to couple these two models is to use a LSS to compute the area covered by such an environment and the climate forcing. The micro-topography model driven by the LSS data will then be able to feed back to the LSS the response of local soil features to such forcing for the given area.

Overall, the general agreement between field measurements and model in this study results suggests that statistical methods and simple parameterizations, if accurately tuned with field data, could be a powerful way to consider spatial scale interactions in such heterogenous and complex environments.

Chapter 3

Micro-topography controls on CH_4 emissions and energy balance in northern peatlands

A challenging problem in climate modeling is how to deal with interactions and feedbacks across a multiplicity of spatial scales, and how to improve our understanding of the role played by local soil heterogeneities in the climate system. This is of particular interest in northern peatlands, because of the large amount of carbon stored in the soil. Greenhouse gas (GHG) fluxes, such as methane, carbon dioxide and water vapor, vary largely within the environment, as an effect of the small-scale processes that characterize the landscape. It is then essential to consider the local heterogeneous behavior of the system components in order to properly estimate water and carbon balances. We propose a novel method to fill the scaling gap from local mechanistic models to large-scale mean field approximations. We developed a surface model for peatlands working at the landscape-scale, which is able to show the impact of surface micro-topography in modeling greenhouse gas fluxes and surface energy balance. We tuned our landscape-scale model with data from a peatland site in the Komi Republic of Russia. We simulate surface micro-topography and hydrology, and we couple it to a process-based model for methane emissions. By partitioning the space in smaller subunits and then analyzing the landscape-scale behavior of the system, we are able to resolve the small-scale processes and to investigate their effects at larger scales. We not only investigate the influence of the hummocky surface on GHG emissions, but we are also able to simulate how complex sub-grid scale hydrological interactions affect the average energy balance of the peatland.

3.1 Introduction

The general issue of scale interactions in the climate-biosphere system is of particular relevance in northern peatlands. Peatlands are wetlands where the terrain is covered by at least 30-40 cm of partly decomposed organic matter (peat). Peatlands cover only about 3 % of the global land surface (Wieder et al., 2009), but they play a fundamental role in the global carbon cycle (Blodau, 2002; Limpens et al., 2008). This is particularly true in boreal latitudes, where peatlands and wetlands are one of the largest sources of natural methane (i. e., Bousquet et al., 2006). This is due to the fact that during the Holocene peatlands constantly worked as a sink of atmospheric carbon carbon (Smith et al., 2004), and recent estimations by Yu et al. (2010) computed the amount of carbon stored in boreal peatlands of about 547 (473-621) Pg, significantly larger than previous estimates of 270-370 Pg (i. e., Turunen et al., 2002). Recent efforts tried to reproduce peatland and wetland extent and carbon accumulation in various Dynamic Global Vegetation Models (DGVMs), (i. e., Schuldt et al., 2013; Kleinen et al., 2012; Wania et al., 2009a,b), and the results are reassumed in the WETCHIMP intercomparison project by Melton et al. (2013); Wania et al. (2013). There are large differences among the different models in peatland representation and in the parameterization of processes. It is nevertheless clear that all of them lack in the representation of fine-scale heterogeneities and sub-grid processes.

In the previous Chapter we showed how local surface heterogeneities matter for water balance in peri-arctic environments. In the present Chapter we propose a novel method that takes into account sub-grid scale processes, and directly assess their impact on the peatland ecosystems, from greenhouse gas emissions, to the energy balance. Baird et al. (2009b) showed how fundamental small-scale features can be in the peatland carbon cycle, as also highlighted by local surface models (i. e., Nungesser, 2003; Bohn et al., 2013). As for peri-arctic peatlands (Sachs et al., 2010), the position of the water table is a fundamental control on greenhouse gas emissions, since it changes the depth of the oxic zone, i. e., the region where methane fluxes coming from below can be oxidated and therefore released as CO_2. As the two gases have different greenhouse properties, it is difficult to estimate the climate impact of natural wetlands and peatlands without precise estimate of methane emissions (Kirschke et al., 2013). In order to compute a consistent greenhouse balance over the region, one should consider the small-scale properties and how the water table and the soil surface heterogeneously change within the environment (Bellisario et al., 1999; Camill and Clark, 1998; Law et al., 2002). Water table position can possibly influence also the surface energy balance, because of the different heat capacity between soil and open ponds. Langer et al. (2011b)

showed how surface temperature heterogeneities can be observed in the Arctic tundra under a large input of solar radiation, which increases the partitioning of latent and sensible heat fluxes. This situation, especially after snow melt, where average water table is generally very high, can have important impacts in boreal peatlands such as the Ust-Pojeg mire complex in the Komi Republic, Russia.

We developed a mechanistic model working at the landscape-scale for a typical boreal peatland, in order to show the importance of surface micro-topography on greenhouse gas fluxes. These small-scale surface heterogeneities are typical in peatlands, and consist in elevated and relatively drier zones, called *hummocks*, and lower and relatively wetter zones, called *hollows*. We tuned our landscape-scale model with data from an elevated bog in the Ust-Pojeg mire complex. Many recent studies focused on this study site, and provided measures of fluxes of water vapor, carbon dioxide and methane, as well as energy and water balance (Runkle et al., 2014, 2012; Schneider et al., 2012; Gažovič et al., 2010; Wolf, 2009). The Institute of Soil Science of the Hamburg University measured also the micro-topographic elevation on the site, and we use such extensive datasets to initialize the micro-scale elevation. We couple this hydrological model to a process-based model for methane emissions (Walter and Heimann, 2000). We want to investigate how the complex hydrolological interactions happening within the system at a sub-grid scale ($\sim 10^0$ m) are essential to correctly estimate the landscape-scale land-atmosphere GHG fluxes ($\sim 10^3$ m). In order to compute methane emissions, we force our model climatology with data from the CMIP5 (Coupled Model Intercomparison Project Phase 5) output from the MPI-ESM model: temperature and NPP (net primary productivity) are taken from the present day experiments. We also want to investigate possible effects of micro-topography representation on surface energy balance, and therefore we need to dynamically compute surface and atmospheric temperature. We couple our surface model with a simple one-box atmospheric model originally developed by D'Andrea et al. (2006), and later coupled with a surface model and dynamic vegetation and adapted for water limited environments by Baudena et al. (2008); Cresto Aleina et al. (2013a). We modified the soil representation in order to account for a dynamical water table.

We can then compare the GHG emissions from a model with a consistent micro-topographic representation and the emissions from a single bucket model, which is the classic way to represent such small-scale ecosystems in larger scale regional or global models. Such a comparison can highlight the effects of micro-topography on various peatland characteristics, from water, to carbon and energy balance.

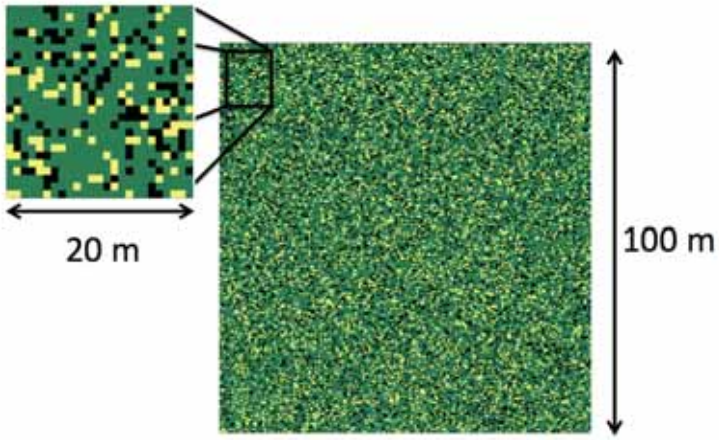

Figure 3.1: Representation of the model grid cell. Colors are function of the water table position in respect to the surface level, going from green (water table below -10 cm), to yellow (water table between -10 cm below the surface, and 10 cm above the surface), to black (water table above 10 cm).

3.2 The model

We develop a model to consider peatland micro-topography, in the framework of a squared lattice. The model works at a landscape-scale of 1 x 1 km, and each cell represents one type of micro-topography, either a hummock or a hollow, with dimensions of 1 x 1 m. We compute for each grid cell both water table balance and methane emissions. We are able to explicitly represent the micro-topography characterizing peatland surface, and therefore we parameterize at the point-scale the heterogeneous hydrological properties of the peatland soil (i. e., hydraulic conductivity, and parameters for the surface and the subsurface water flow). Due to such an accurate representation of the micro-scale, we can upscale emissions and water balance at the landscape-scale. When coupling the model with the atmospheric box model, we compute for each grid cell also the soil and the water temperature ad the point-scale. We then average the local quantities over the whole landscape, aggregating the fluxes to interact with the atmosphere. We compute the atmospheric dynamic quantities at the landscape-scale.

3.2.1 Micro-topography representation

We tune the model with micro-topographic data from a peatland of Northwest Russia, the Ust-Pojeg mire in the Komi Republic (61^o 56'N, 50^o 13'E, 119 m a.s.l.). Many studies focused on this study site as typical boreal peatland, as the mire complex displays different kinds of peatlands type, from an ombrogenous bog, to a minerogenous fen,

Figure 3.2: Series of composite/ 360 degree panoramic images taken by the team from the Institute of Soil Science of the Hamburg University (courtesy of B. Runkle). The images show both the pace of snow melt (5 days) and the sparseness of the micro-topographic features. All the dark spots in the top photo are the tops of hummocks.

to a transitional zone with the surrounding forest. Former studies provided measures of fluxes of water vapor (Runkle et al., 2012), carbon dioxide (Schneider et al., 2012), methane fluxes (Gažovič et al., 2010; Wolf, 2009), as well the energy balance (Runkle et al., 2014), and we use these measures to evaluate the performances of the model. The extensive studies on the site also allow us to represent peatland micro-topography (i. e., hummocks and hollows). In order to consistently simulate small-scale surface heterogeinities, we use field data to initialize the surface elevation in the model. We focus our modeling framework on the bog, in order to exclude the influence of the underground water flow that characterizes the fen ecosystem.

We use the dataset collected by expeditions organized by the Institute of Soil Science of the University of Hamburg. It consists of elevation data measured over the whole mire complex. We organize the elevation data in a histogram, in order to infer the statistical distribution. We then randomly pick a value from the statistical distribution, and we assign it to each grid cell. We assume that with this procedure we statistically capture the peatland micro-topography. If the grid cell at the position i, j has an elevation $H_{i,j}$ above a surface level $H_0 = 20$ cm then we assume that such a grid cell is a *Hummock*, otherwise it is a *Hollow* (B. Runkle, personal communication). Along

with the micro-topography, we initialize each cell with other two properties which affect methane production and hydrology respectively: peat depth $pd(i,j)$ and slope $sl(i,j)$. The peat depth roughly reproduces the peat profile of the bog in the Ust-Pojeg mire, and it is modelled as:

$$pd(i,j) = \frac{pd_x(i,j) + pd_y(i,j)}{2} \tag{3.1}$$

where

$$\begin{cases} pd_x(i,j) = (0.3/250)x \text{ m if } x(i,j) < 250 \\ pd_x(i,j) = 0.3 + (0.7/50)(x(i,j) - 250) \text{ m if } 250 \leq x(i,j) < 300 \\ pd_x(i,j) = 0.3 + (0.7/50)(x(i,j) - 250) \text{ m if } 300 \leq x(i,j) < 750 \end{cases} \tag{3.2}$$

where x(i,j) is the longitudinal position of the grid cell, ranging from 1 to 1000 m, and analogously:

$$\begin{cases} pd_y(i,j) = (0.3/250)x \text{ m if } y(i,j) < 250 \\ pd_y(i,j) = 0.3 + (0.7/50)(y(i,j) - 250) \text{ m if } 250 \leq y(i,j) < 300 \\ pd_y(i,j) = 0.3 + (0.7/50)(y(i,j) - 250) \text{ m if } 300 \leq y(i,j) < 750 \end{cases} \tag{3.3}$$

where y(i,j) is the latitudinal position of the grid cell, ranging from 1 to 1000 m. Peat depth basically gives information on the amount of carbon available for decomposition and GHG emissions.

The second term $sl(i,j)$ parameterizes the slope of the bog. We assume the slope of the bog to have a uniform linear dependence on the y axis:

$$sl(i,j) = 3 - y(i,j)/m_y \text{ m} \tag{3.4}$$

where $m_y = 1$ km is the longitudinal dimension of the landscape-box representing our bog. The slope regulates water flow over the peatland due to the Manning's Flow (see Section 3.2.3).

3.2.2 Water table dynamics

We compute water table position at each time step. We start the simulations at the end of March, i. e. when snow melt takes place, and we end it at the mid of October, when the cold season starts. We also model snow melt explicitly since it represents one of the main inputs in the water balance, and most of the landscape becomes inundated, as we can see in the lower two snapshots of Figure 3.2. For each cell at position i,j we

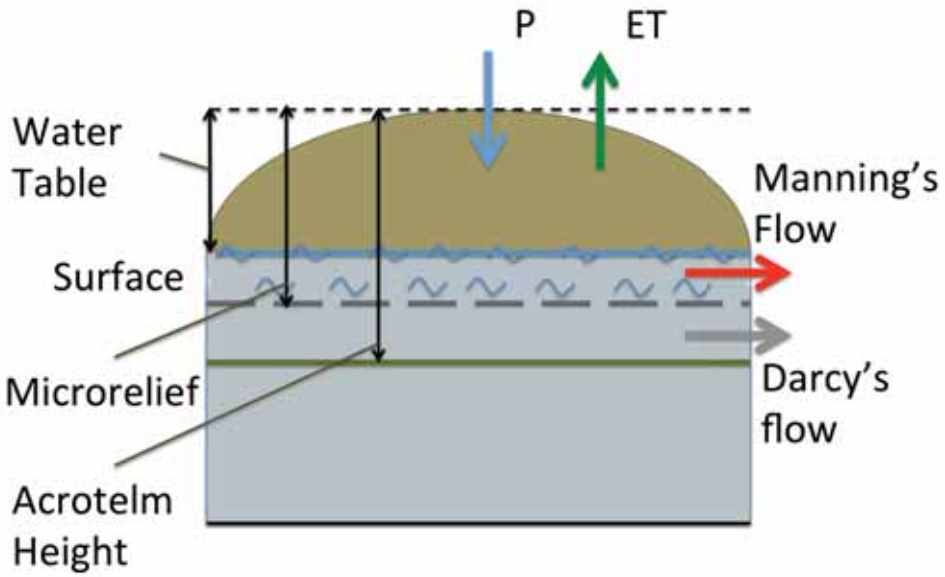

Figure 3.3: Schematics of a model grid cell, i. e., a hummock. The water table position can variate due to precipitation P, evapotranspiration ET, and lateral runoff. Lateral runoff is parameterized as the sum of the Manning's and the Darcy's flow. One further input to water table is the snow melted at the beginning of the simulation (not shown). Height of the acrotelm variates from cell to cell, following micro-topography representation.

compute the water balance following the equation:

$$\frac{dW_{i,j}}{dt} = \frac{S + P - E_{i,j} + R_{i,j}}{s_{i,j}} \tag{3.5}$$

where $W_{i,j}$ is the water table level in the cell at the position (i, j) relative to the reference surface level, S is the snow melt input, P is the precipitation income, $E_{i,j}$ is the evapotranspiration, $R_{i,j}$ is the lateral runoff, $s_{i,j}$ is the drainable porosity, and t is the daily time step.

Snow melt S represents the water input at the beginning of the warm season. The cold season is not represented in the model, because we assume the snow to cover the area (almost) uniformly. We simulate cumulative snowfall Sn using a gamma function, and we assume that snowfall takes place in 180 days:

$$Sn = \sum_{n=1}^{180} \gamma_S(n) \tag{3.6}$$

where γ_S is a random number following a 2-parameter gamma-distribution with shape parameter $\alpha = 1$, and scale parameter $\beta = 1$.

To simulate the snow melt, we use a melting-degree formula, which determines the

amount of snow melting each day as a function of the air temperature:

$$S(t) = \frac{R_f Sn - M_s(T(t) - T_0)}{\delta t} \tag{3.7}$$

where $M_s = 3$ mm K^{-1} is a tuning parameter that regulates the snow melt input into the system. $T(t) - T_0$ takes into account when air temperature T at time t is above $T_0 = 273.15$ K, and $\delta t = 1$ day. Number $R_f = 0.3$ takes into account the difference in water and snow volume.

Precipitation is the main water input, and it is a given forcing that, analogously to what we did in Chapter 2, follows the formula:

$$P(t) = P_r \gamma_P(t) \tag{3.8}$$

where $P_r = 10$ mm regulates the amplitude of the precipitation events, and γ_P is a random number following a 2-parameter gamma-distribution with shape parameter $\alpha = 0.3$, and scale parameter $\beta = 1$. We choose both γ_P and γ_S in order to fit the data of local cumulative precipitation, and the cumulative amount of snow falling during winter respectively. Evapotranspiration on the other hand is dependent on the soil dryness and patchiness. We refer to former studies (Nichols and Brown, 1980), which extensively analyzed the evaporation rate from sphagnum moss surface. We made the evapotranspiration dependent on the day of the season, the surface wetness, and on the micro-topographic features.

$$ET_{i,j} = \begin{cases} \frac{ET^{min}_{i,j}}{fr(W_{i,j})} \sin(\frac{(t-4T)\pi}{6T}) & \text{if } 180 < t < 300 \\ \frac{ET^{min}_{i,j}}{fr(W_{i,j})} & \text{otherwise} \end{cases} \tag{3.9}$$

where t is the time step in days of Gregorian calendar and $ET^{min}_{i,j}$ depends on the micro-topographic features for the cell at the position i, j:

$$ET^{min}_{i,j} = \begin{cases} 6 \text{ mm d}^{-1} & \text{if Hummock} \\ 3 \text{ mm d}^{-1} & \text{if Hollow} \end{cases} \tag{3.10}$$

and $fr(W_{i,j})$ takes into account the fact that evaporation takes place at a higher rate if water table is above the surface:

$$fr(W_{i,j}) = \begin{cases} 1 & \text{if } W_{i,j} \text{ above the surface level} \\ 2 & \text{if } W_{i,j} \text{ below the surface level} \end{cases} \tag{3.11}$$

Term $s_{i,j}$ is the drainable porosity, and it variates spatially both horizontally and

vertically. If water table is above the surface level, $s_{i,j} = 1$, whereas if the water table is below the surface, we assume it to follow:

$$s_{i,j} = \begin{cases} 0.8 & \text{if Hummock} \\ 0.5 & \text{if Hollow} \end{cases} \tag{3.12}$$

By dynamically representing the water table at the micro-topographic level, we are able to distinguish the subsurface water flow in hummocks and hollows. We expect that the statistical distribution of the spatial pattern of the water table depth will change over the season, as the subsurface water flow changes among the different micro-topographic units.

3.2.3 Lateral runoff

Lateral runoff term R computes the water flux among the different grid cells, and it allows the water exchange. We compute it as $R_{i,j}^{IN} - R_{i,j}^{OUT}$, where $R_{i,j}^{IN/OUT}$ is the sum of Darcy's and Manning's flows D and M:

$$R_{i,j}^{IN/OUT} = D_{i,j}^{IN/OUT} + M_{i,j}^{IN/OUT} \tag{3.13}$$

Where Darcy's Law and Manning's flow represent the underground water flow and the overland water flow respectively. They are parameterized as:

$$D_{i,j}^{IN/OUT} = D_{i,j} \frac{\Delta W_{i,j}}{m_{i,j}^{x/y}} \tag{3.14}$$

$$M_{i,j}^{IN/OUT} = \begin{cases} \left(\frac{k}{Mc_{i,j}}\right) Rad_{i,j}^{\frac{2}{3}} \Delta Sl_{i,j}^{\frac{1}{2}} & \text{if } W_{i,j} > 0 \\ 0 & \text{otherwise} \end{cases} \tag{3.15}$$

Both terms are computed in mm/day.

Term $m_{i,j}^{x/y}$, instead, is the distance between the centers of cells i and j. In respect to the classical expression for Darcy's Law, we the consider the term $D_{i,j}$ to represent the hydraulic conductivity, and its units are lengths per time. It is spatially dependent, since we assume a different value for hummocks and hollows:

$$D_{i,j} = \begin{cases} 0.005 & \text{mm if Hummock} \\ 0.01 & \text{mm if Hollow} \end{cases} \tag{3.16}$$

Manning's formula describes the velocity of an overland flow driven by gravity.

It is also dependent on the soil heterogeneity because we assume a difference in the hummock-hollow surface roughness. In the equation, this term is represented by the dimensionless number $Mc_{i,j}$:

$$Mc_{i,j} = \begin{cases} 4 & \text{if Hummock} \\ 0.4 & \text{if Hollow} \end{cases} \tag{3.17}$$

k is a conversion factor of 1 $m^{1/3}s^{-1}$. $\Delta Sl_{i,j}^{\frac{1}{2}}$ represents the difference in slope between the cells i and j. The term $Rad_{i,j}^{\frac{2}{3}}$ is the hydraulic radius, defined as

$$Rad_{i,j} = \frac{A_{i,j}}{P_{i,j}} \tag{3.18}$$

where $A_{i,j}$ is the cross sectional area of flow, in our model:

$$A_{i,j} = m_{i,j}^{x/y}(W_{i,j} - H_{i,j}) \tag{3.19}$$

and $P_{i,j}$ is the wetted perimeter, or the perimeter of the cross sectional area $A_{i,j}$ at contact with water, in our model:

$$P_{i,j} = 2(W_{i,j} - H_{i,j})m_{i,j}^{x/y} \tag{3.20}$$

where $W_{i,j} - H_{i,j}$ is the elevation of water table in respect to the surface and $m_{i,j}^{x/y}$ is the lateral extent of the grid cell.

Manning's flow occurs on only if the water table is above the surface level, whereas Darcy's flow is always occurring. Hydrology representation is the one of main differences between this new approach and the classical bucket model, and the main driver of water seasonal dynamics. The heterogenous surface and the interactions among the different grid cells represent at a fine spatial scale actual interaction among hummocks and hollows in actual peatlands. Values for parameters are displayed in Table 3.2.

3.2.4 Coupling with a process-based methane emissions

In respect to Chapter 2, here we propose a more explicit parameterization of methane fluxes, by coupling the micro-topographic model to a process-based model for methane emissions, in order to more consistently quantify the effect of surface heterogeneities on GHG fluxes. The model developed by Walter and Heimann (2000) is an accurate and quite general model for methane emissions, which can be applied to peatlands

in different environments. In particular, it is the same model which is built in some DGVMs, such as JSBACH (Schuldt et al., 2013), and LPJ (Kleinen et al., 2012). We tune the model to perform in a typical peatland at the latitude of the Ust-Pojeg mire complex. In Table 3.1 we show the list of parameters used to force the methane model. We couple the methane model at each cell, and we compute methane fluxes locally. We average over the whole landscape in order to upscale the local fluxes at the landscape-scale. The process-based model for methane emissions provides an output of methane fluxes $F^{i,j}_{CH_4}$ as a function of water table, carbon available, daily net primary productivity (NPP), and temperature:

$$F^{i,j}_{CH_4}(t) = f(W_{i,j,}(t), S^{oil}_{i,j}(t), NPP^{d}_{i,j}(t), T^{d}_{i,j}(t)) \tag{3.21}$$

Where $W_{i,j}$ is the water table depth in respect to the surface computed at each position i, j, $S^{oil}_{i,j}$ is the soil depth, $NPP^{d}_{i,j}$ the daily NPP of the ecosystem, $T^{d}_{i,j}$ the daily temperature. The water table depth is a fundamental control on methane emissions, since it regulates the depth of the oxic zone, where methane coming form below the water table horizon can be oxidate as CO_2. The soil depth takes into account that each grid cell has a different peat depth. We sum the peat depth to the height of the acrotelm (the part of peat containing living plants, which we assume being $H_{i,j}$). This quantity $S_{i,j}$ controls the amount of carbon available:

$$S^{oil}_{i,j} = pd_{i,j} + H_{i,j} \tag{3.22}$$

We force the model with prescribed time series of of NPP and temperature. The time series are computed from simulations performed for the CMIP5 experiments with the MPI-ESM model. We extracted temperature and NPP for the grid cell with latitude and longitude corresponding to the one of the Ust-Pojeg mire. Both time series are adapted for each time cell i, j taking into account that NPP and temperature vary if water table lays above or under the soil surface. In particular, we assume:

$$NPP^{d}_{i,j}(t) = \begin{cases} 0 & \text{if } W_{i,j}(t) > 15 \text{ cm} \\ NPP(t) & \text{otherwise} \end{cases} \tag{3.23}$$

where $NPP(t)$ is the net primary productivity from the MPI-ESM model at the time step t. For the temperature dynamics we assume:

$$T^{d}_{i,j}(t) = \begin{cases} T(t) - 5 & \text{K if } W_{i,j} > 15 \text{ cm} \\ T(t) & \text{otherwise} \end{cases} \tag{3.24}$$

Parameter	Meaning	Value
S_{depth}	Soil depth	150 cm
r_{depth}	root depth	70 cm
R_0	Tuning parameter	0.30

Table 3.1: Table of parameters used in coupling the micro-topographic model to the process-based model for methane emissions (Walter and Heimann, 2000)

where $T(t)$ is the atmospheric temperature from the MPI-ESM model at the time step t. We assume that the atmospheric temperature and the soil temperature are the same if the water table is below the threshold of 15 cm. If water is above the threshold, we assume that due to the different heat capacity of water, the soil is cooler than the atmosphere.

Tuning parameter R_0 in the model, tuned depending on climatic condition, is set to 0.30, following references in Walter and Heimann (2000). We assume the vegetation of the peatland to consist only of *sphagnum* and not to vary in space or in time.

3.2.5 Coupling with an atmospheric box model

The equation of the coupled soil-atmosphere system for the potential air temperature tendency is modeled as following:

$$\rho_a h_a c_{pa} \frac{d\theta}{dt_h} = G - \rho_a h_a c_{pa} \frac{\Delta\theta}{\delta t_h} + \epsilon_S \epsilon_a \sigma < T_S >^4 + R_L \tag{3.25}$$

Where θ is the PBL potential temperature, t_h the hourly timestep, G the sensible heat flux, ρ_a the air density, h_a the PBL height, c_{pa} the specific heat of air, $\Delta\theta$ the convective adjustment, R_L the lateral relaxation of temperature, ϵ_S and ϵ_a the emission - absorption coefficients of soil and air respectively, and σ the Stefan-Boltzmann constant. The emission temperature in the third term r.h.s., $< T_S >$, is the average over the whole landscape of the heterogeneous soil temperature $T_{i,j}$ computed for each cell in the soil surface module. Convective adjustments and precipitation are computed following D'Andrea et al. (2006).

As we showed above, the influence of micro-topography can be evaluated by coupling an accurate dynamical description of water table with a process-based methane model. On the other hand, the effect of local surface heterogeneities on the energy balance can be investigated by coupling the model for micro-topography with a dynamical model for the atmosphere. We use a one-box model for the convective boundary layer, with

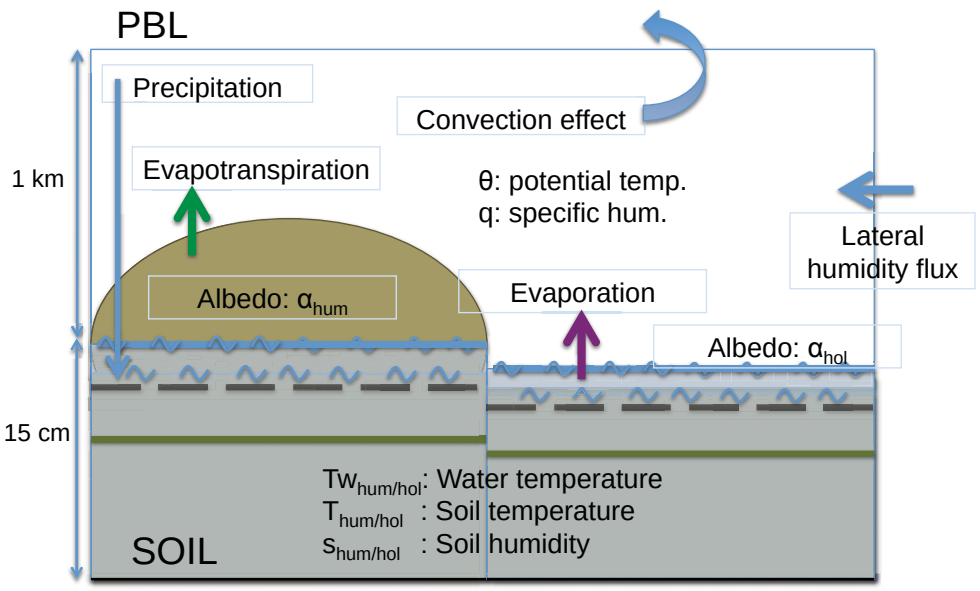

Figure 3.4: Schematics of the micro-topographic model coupled to the atmospheric box model. Lateral processes are not shown.

parameterizations of convection and precipitation. We modified the model developed in D'Andrea et al. (2006), and coupled to soil and vegetation in Baudena et al. (2008), and in Cresto Aleina et al. (2013a).

The model also computes dynamically specific humidity, following the equation:

$$\rho_a h_a \frac{dq}{dt_h} = < E > - \rho_a h_a \frac{\Delta q}{\delta t_h} + F_L \tag{3.26}$$

Where q is the specific humidity, Δq the convective adjustment, F_L the lateral moisture influx, and term $< E >$ the aggregated evaporation flux, averaged over the whole landscape from heterogeneous fluxes $E_{i,j}$. Evapotranspiration follows the Penman-Monteith equation:

$$E_{i,j} = E_{i,j}^{min} \frac{\Delta(F_r - G) + \rho_a c_{pa}(q) g_a}{L_e(\Delta + \gamma(1 + g_a/g_s))} \tag{3.27}$$

Where Δ is the rate of change in saturation specific humidity (in Pa K^{-1}), F_r is the incoming solar radiation (W m^{-2}), G the sensible heat flux at the ground (W m^{-2}), ρ_a the dry air density, c_p is the specific heat capacity of air (J kg^{-1} K^{-1}), g_a and g_s (measured in m s^{-1}) the conductivities of air and soil respectively, and L_e is the volumetric latent heat of vaporization. Parameters for this equation are fixed accordingly to Runkle et al. (2014).

We compute the surface temperature at each time step t_h as:

$$S_{i,j}^{oil}[q(\rho_S c_{pS}) + (1-q_f)(\rho_W c_{pW})]\frac{dT_{i,j}}{dt_h} = (1-\alpha_{i,j})F_r - G - L_e E_{i,j} - \epsilon_S \sigma T_{i,j}^4 - \\ - \rho_S c_{pS}\frac{h_S - h_{SD}}{\tau_T}(T_{i,j} - T_D) - \\ - \delta_W \rho_S c_{pS}\frac{h_S - W_{i,j}}{\tau_{Tw}}(T_{i,j} - T_{Wi,j}) \tag{3.28}$$

Where $T_{i,j}$ is the soil temperature, ρ_S the density of peat (assumed constant), c_{pS} the specific heat of peat, ρ_W is the density of water, c_{pW} the specific heat of water, and q_f is a free parameter that describes the mixture of water and peat in soil. In our model, $q_f = 0.2$. On the r.h.s, $\alpha_{i,j}$ the albedo, F_r the incoming shortwave radiation, L_e the latent heat of evaporation, $E_{i,j}$ the water flux due to evaporation. The last two terms on the r.h.s. represent the heat conduction between soil and the deeper soil, and soil and water layer respectively: T_D is the fixed temperature of the deeper soil, $T_{Wi,j}$ is the dynamical temperature of the water standing above the soil layer. h_{SD} and $W_{i,j}$ are the heights of the deep soil layer and of the water table in respect to the surface respectively. In particular, $W_{i,j}$ is a quantity that we compute dynamically in Equation 3.5. Term δ_W is a step function that allows the last term to be not zero only if the water table is above the surface level:

$$\delta_W = \begin{cases} 1 & \text{if } W_{i,j} - surf_{i,j} > 0 \\ 0 & \text{otherwise} \end{cases} \tag{3.29}$$

Therefore, if water table lays below the surface level, we assume it does not influence the temperature of the soil. In wetlands and peatlands it is not unusual that water table lays above the surface layer, in particular during the snow melt period. This affects energy balance as well as GHG fluxes, since latent heat fluxes are different from open ponds to saturated or unsaturated terrain, and water heat capacity is different from the one of peat. If $W_{i,j} > 0$, we add a further tendency equation, which is the one for open water temperature.

$$\delta_W \rho_W W_{i,j} c_{pW}\frac{dT_{Wi,j}}{dt} = (1-\alpha_{i,j})F_r - G - L_e E_{i,j} - \\ - 2\epsilon_W \sigma T_{Wi,j}^4 + \epsilon_S \epsilon_W \sigma T_{i,j}^4 + \\ + \rho_S c_{pS}\frac{h_S - W_{i,j}}{\tau_{Tw}}(T_{Si,j} - T_{Wi,j}) \tag{3.30}$$

While for the other quantities the initial conditions are initialized at the beginning of the simulation, we assume the water to be at the same temperature of the soil at

Symbol	Meaning	Value	Units
ρ_a	Air density	1.2	kg m^{-3}
ρ_S	Soil density	1300	kg m^{-3}
ρ_W	Water density	1000	kg m^{-3}
h_a	Height of PBL	1000	m
h_{SD}	Deep soil layer depth	2.5	m
ϵ_S	Emissivity of PBL	0.2	–
ϵ_a	Emissivity of soil	0.8	–
ϵ_W	Emissivity of water	0.9	–
σ	Stefan-Boltzmann constant	5.6×10^{-8}	W m^{-2} K^{-4}
g_a	Air conductivity	0.00135	m s^{-1}
g_s	Stoma conductivity	0.00148	m s^{-1}
γ	Psychometric constant	66	Pa K^{-1}
L_e	Latent heat of vaporization	2.501×10^6	J kg^{-1}
c_{pa}	Air specific heat	1005	J kg^{-1} K^{-1}
c_{pS}	Soil (dry) specific heat	2000	J kg^{-1} K^{-1}
c_{pW}	Water specific heat	4200	J kg^{-1} K^{-1}

Table 3.2: The Table shows the parameter values for the atmospheric model.

the time at which $W_{i,j} > 0$. We keep vegetation cover constant over the season, since we assume this approximation does not represent a large bias for the purpose of this model.

Lateral fluxes of heat in soil are not considered, because we assume them to be of order of magnitudes smaller than the vertical heat exchanges. Values for parameters are shown in Table 3.2. We conducted tests on parameter values in realistic ranges and the behavior of the model does not change qualitatively.

3.3 Results and discussion

The model we developed allows us to consistently represent the micro-topographic effect on hydrology and methane emissions in a typical northern peatland. We first study the possible effects with a stand-alone model and a prescribed external temperature. By coupling the model with a simple dynamic representation of the convective boundary layer instead, we are able to remove this prescription and to dynamically compute the effect of micro-topography on the peatland energy balance.

We first discuss the statistics of the micro-topographic representation, as well as the properties of the methane emissions. We then present the results of the stand-alone model, comparing the novel approach to a classical bucket model, and finally we show the results for the coupling with an atmospheric box model.

3.3.1 Micro-topography statistics

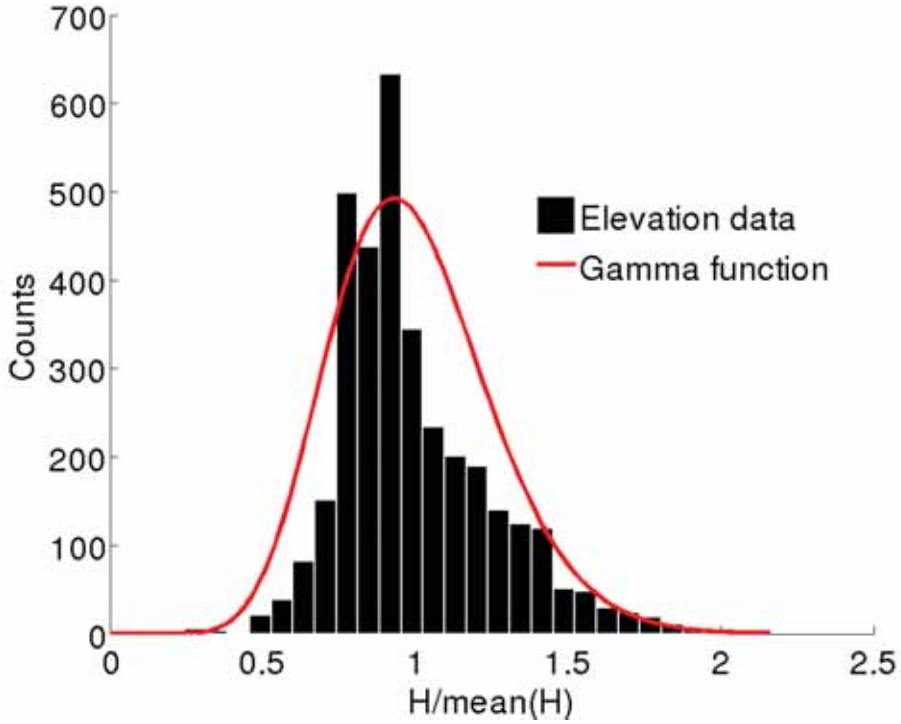

Figure 3.5: Comparison between the Ust-Pojeg mire elevation data collected by the team of the University of Hamburg and a generalized 3-parameters gamma distribution multiplied by maximum number of counts in the histogram. The good visual agreement is confirmed by the positive results from a Kolmogorov-Smirnoff test at 5% confidence (P≥0.5).

We initialize soil surface elevation with elevation data collected in the field. In order to be sure to consistently represent the surface elevation, we try to infer the statistical distribution of the field data. The histogram appears skewed on the right tail, as we show in Figure 3.5. We fitted the histogram with a generalized 3-parameters gamma distribution multiplied by maximum number of counts in the histogram:

$$f_A(x) = N_{max}\frac{1}{2}\frac{b^q x^{q-1} e^{-bx}}{\Gamma(q)},\ b > 0,\ q > 0. \tag{3.31}$$

The visual fit is good, and we run a Kolmogorov-Smirnoff test at a level of confidence of 5%. The test shows that the population has no significant difference to the function

$f_A(x)$. We tested also other distributions, such as normal distribution, exponential, and lognormal, but none of them passed the Kolmogorov-Smirnoff test. We then assume that $f_A(x)$ fits our data well enough to be used for our purposes as parameterization of the distribution for micro-topographic elevation, and we proceed to initialize the microtopogrpahic model by assigning at each grid cell a value randomly picked from $f_A(x)$. Parameters in Equation 3.31 are:

- $b = 5.8$
- $q = 8.9$
- $r = 1.5$

The distribution of surface elevation is not bimodal, as showed in (Eppinga et al., 2008). Even though the histogram shows two peaks they are too near to be resolved in a bimodal distribution. In Figure 3.5 we show the good agreement between the field elevation data (histogram) and $f_A(x)$ (red line).

3.3.2 Micro-topography controls on hydrology and methane emissions

Previous studies suggested that micro-topography may influence GHG emissions (Baird et al., 2009a). An accurate description of the complex hydrological processes happening at small scales in peatlands is necessary to consistently model GHG emissions. We do not simulate winter season, but we randomly compute snowfall, namely the amount of water available water for the ecosystem at the beginning of the season. How this water flows through the system depends on the hydrology representation of the system itself. We expect that a more physically based representation of these process would affect and improve the dynamics of methane emissions. We performed ensemble simulations with 30 ensemble members and we compared two versions of the model. In the standard model version (hereafter *Microtopography*) we simulate accurately micro-topography as discussed in the previous Sections. In order to be able to investigate the micro-topographic effect, we realized a second version of the model (hereafter *Single bucket*), in which the whole peatland is represented by a simple bucket. Its height and peat depth are the same over the whole region.

In Figure 3.6 we show the dynamics of the water table averaged over the whole region. As expected, the differences on the water table dynamics is significant. In the model version version *Single bucket*, after the snow melt period and the large income of

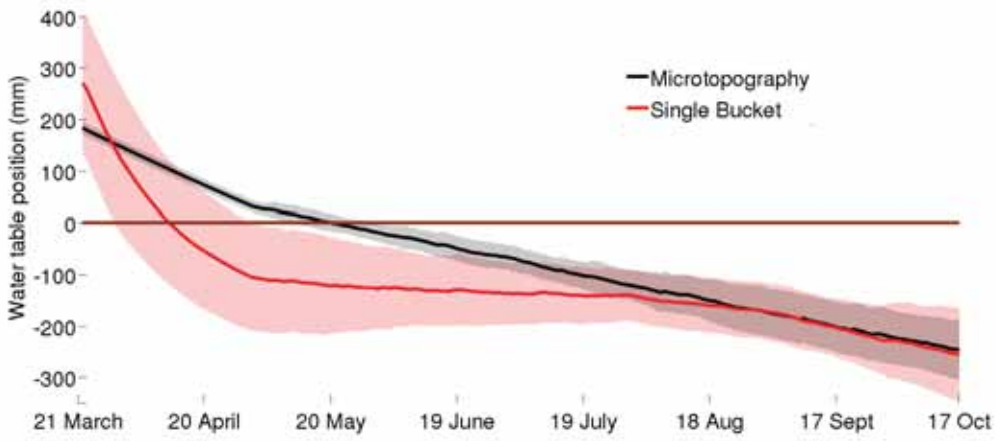

Figure 3.6: The figure shows ensemble simulations of water table dynamics. We show a comparison between the sub-grid tessellation approach (black line) and the single bucket (red line). The micro-topography affects water table position by delaying the runoff, because of the complex interactions among the grid cells, which we resolve in a finer scale model. The shaded areas represent the standard deviation over 30 simulations.

water which basically floods the system, the water flows out. As a result, water table drops early in the warm season, increasing the oxic zone depth. In the *Microtopography* version, instead, the complex sub-grid scale interactions delay the runoff. The large decrease in water table position at the beginning of the season in *Single bucket* version disappears if one takes into account the flow among the different micro-topographic units. In particular, small elevated spots (hummocks) can delay the strong Manning's flow (Equation 3.15), making the decrease in water table almost linear. This dynamics is similar to the observations, which show a much smoother water table decrease, as in **?**Schneider et al. (2012).

The water table position affects the oxic zone depth, i. e. the depth of the zone where methane emitted by the deeper soil, in the anoxic zone, can be oxidated and therefore emitted as carbon dioxide. Figure 3.7 shows how important effects the differences in water table representation can have. In particular, the *Single bucket* version, because of the deeper oxic zone during most of the season, shows much smaller methane fluxes than the *Microtopography* version. The visual difference is even more striking if one considers the cumulative methane emissions over the whole simulation, which differ by a factor of 2. The *Microtopography* version performs much better in comparison to chamber measurement data (Wolf, 2009, Master thesis). The large peak toward the end of August in Figure 3.7 can be explained by the high temperatures in the CMIP5 time series.

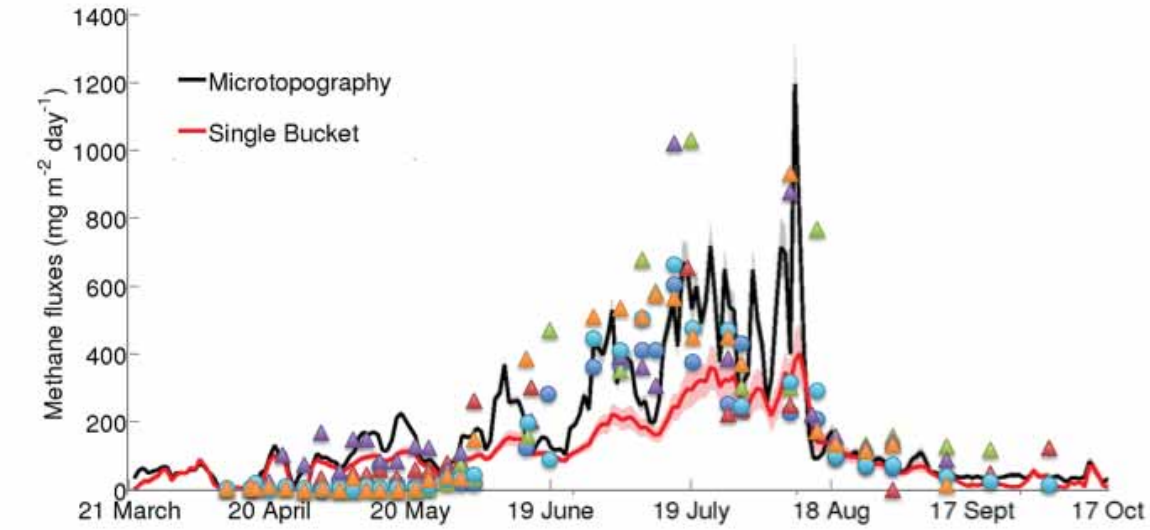

Figure 3.7: The figure shows ensamble simulations of methane emissions. Methane emissions are computed by coupling the model with a process-based model. As in Figure 3.6, we compare the *Microtopography* version of the model (black line) with a *Single bucket* version without microtopgraphy representation (red line). We show the average of 30 ensemble runs (solid line) and the standard deviation among the runs (shaded areas). Because of a different representation of hydrology, the micro-topography deeply affects the methane emissions, as the *Single bucket* version emits much less methane. The shaded areas represent the standard deviation over 30 simulations. The superimposed dots and the triangles represent in situ chamber measurements from Wolf (2009). The order of magnitude of the local data is better captured by the model with micro-topography. Some differences still exist because of the different climatology between model and measurements. Moreover, both black and red lines are averages over the whole landscape, whereas the measurements represent single plots.

3.3.3 Spatial representation of water table and methane emissions

We compute water table position and methane emissions for each cell of the squared lattice. Due to the heterogeneous pattern of soil properties, water table variates not only over the season, but also spatially. We show the impact of such an heterogeneous pattern on hydraulic properties in Figure 3.8, where we plot in histograms the water

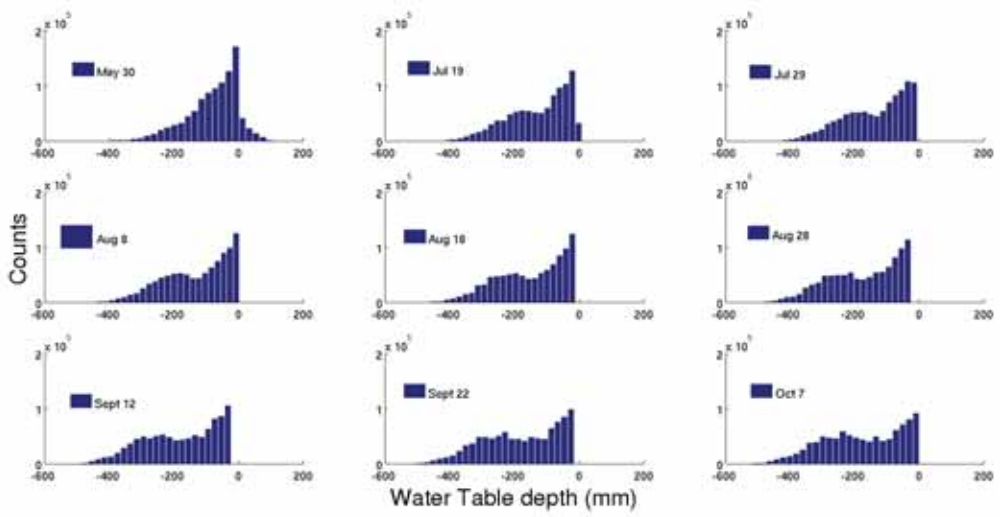

Figure 3.8: Histograms of water table distribution over the landscape at different days of simulation We simulate water table position relatively to the surface level for all cells. As expected, the distribution shifts towards negative values towards the end of the season. The two peaks emerging by July coincide with the peak in water table distribution of hummock and hollow grid cells respectively, as shown in Figure 3.9. The distribution shape does not change qualitatively after the emergence of the second peak, but its position shifts as the water balance changes. In particular, the peak near to the 0 level constantly decreases.

table depth relative to the surface elevation for each grid cell. In particular, we see how the one peak at the beginning of the simulation splits in two peaks from July onwards. This is due to the strong Manning's flow, that washes the water which stays above the surface out of the system. This explains how by the end of July no grid cell displays $W_t > 0$, where the 0 level is fixed at the grid cell surface level. The second peak emerging as the simulation proceeds coincides with the peak in water table distribution in the hummocks (panel (a) in 3.9). Analogously, the peak near to the surface level coincides with peak of the water table distribution in hollows (panel (b) in 3.9).

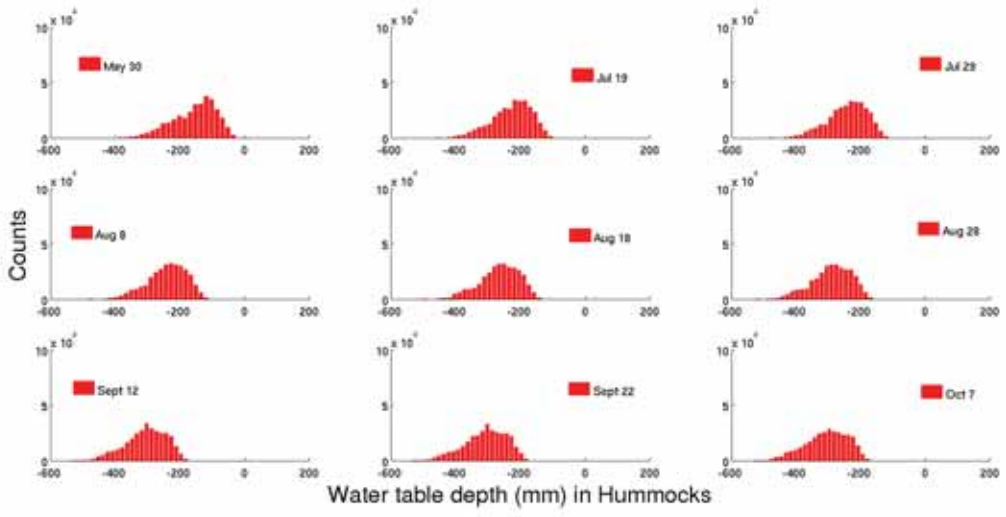

(a)

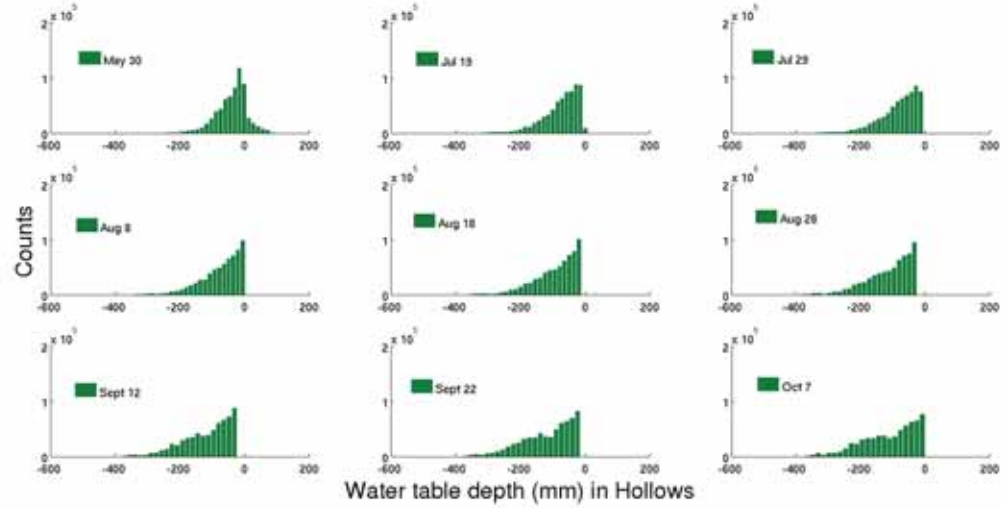

(b)

Figure 3.9: Histograms of water table position in hummocks and hollows. The two micro-topographic classes we take into account in this study show different spatial distribution of water table depth relatively to the surface. The drier hummocks maintain the distribution shape over the simulation, whereas the histogram of water table in hollow grid cells becomes peaked around the 0 level surface). This is due to the strong Manning's flow, that makes water above the surface run off.

We can also investigate what is the relative water table distribution among hummocks and hollows (Figure 3.10). As expected, the position of the water table relative to the surface level is lower in the drier hummocks than in the hollows, where it is often above the surface level. At the beginning of the season, the peaks of hollow water table distribution and hummock water table distribution are in a similar position in respect to the surface. As the simulation proceeds and water table drops, both hummocks

and hollows become drier, but relative water table position drops differently in the two micro-topographic classes. The shape of hummock water table distribution does not change over the season, and its position shifts towards more and more negative values. In the case of hollows, instead, the large peak in proximity of the 0 level (surface) decreases only at the end of the season, when still many grid cells display a water table at the surface level.

In Figure 3.10 we show histograms of methane emissions at different time steps, and we separate the contributes of the two microtopogrpahic classes, i. e., hummocks and hollows. Hollows as expected contribute more than hummocks on methane emissions, being generally wetter and thus displaying a shallower oxic zone. This feature is well displayed in the histograms as the shape of the total histogram is basically dominated by the contribution of the methane emissions of hollows. Methane emissions increase drastically at the end of July and at the beginning of August as also shown in Figure 3.7, due to a higher temperature forcing. By the end of August, instead, water table drops in average at a level lower than 100 mm from the surface, causing a significant decrease in methane emissions (note the different scale of the horizontal axis in the figure). We can conclude that hollows are the methane hotspots, and hummocks basically reduce the emissions. On the other hand, the presence or the absence of hummocks determines the shape of water table distribution, which in turn regulates the oxic zone depth. micro-topography representation takes into account these characteristics and correctly represents the ecosystem. Results are similar in magnitude of fluxes to the chamber measurements shown in Wolf (2009).

3.3.4 Micro-topography effects on the ecosystem-scale energy balance

In the previous Sections we explored how micro-topography affects methane emissions. Such a control is quite straight-forward, since position of water table regulates the oxic zone depth. The impact of micro-topography on the local energy balance has been instead less explored by past studies. We introduce therefore a novel approach combining a simple theoretical box model for the lower troposphere (i. e., the Planetary Boundary Layer) to the surface elevation model, once again in both versions, *Microtopography* and *Single bucket*. The results we show do not aim to give a comprehensive and quantitative investigation on possible feedbacks between peatland micro-topography and atmosphere, but it is rather a fist step in a so far unexplored direction.

In Figure 3.6 we show how an improved representation of the water table due to complex hydrological interactions affects the energy balance. The atmospheric poten-

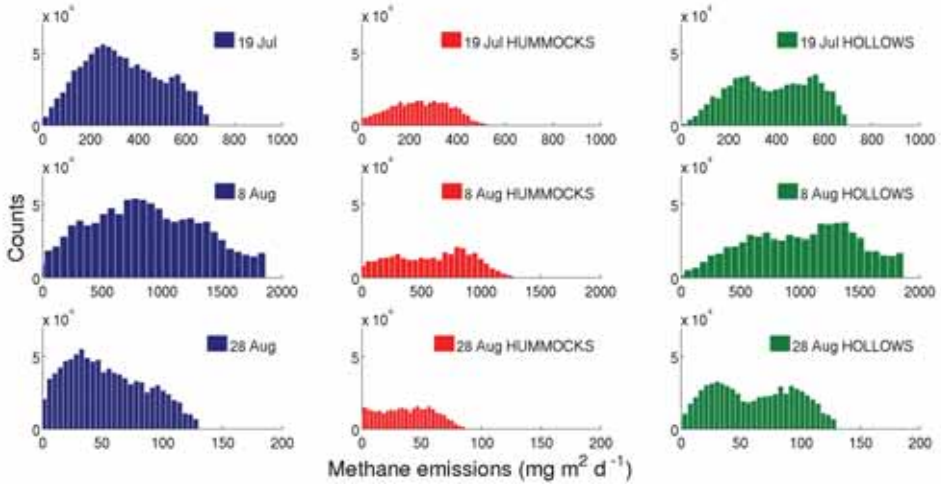

Figure 3.10: Histograms of methane emissions over the landscape. We show methane emissions for all cells (blue histograms), hummocks (red histograms), and hollows (green histograms) at different time steps. We chose to show snapshot of methane fluxes between the mid of july and the end of August because this is the time slice at which changes in methane emission dynamics are more rapid and dramatic. Let us note the different scale of the x axis. Methane emissions increase of almost an order of magnitude in few days, because of temperature forcing and water table position, which, by the end of August is in average below the -10 cm level. This leads to an increase in the oxic zone, where the carbon can be oxidated and released as carbon dioxide.

tial temperature of the planetary boundary layer is affected by sensible and latent heat fluxes. Sensible heat fluxes increase significantly if water table is below the surface, as the latent heat fluxes decrease. Plus, the heat capacity of soil (peat) is different from the one of water. Another factor which may cause difference is the surface albedo. Water is darker than the soil surface, and hollows, wetter, have generally lower albedo than the relatively brighter and drier hummocks. We compare our results with eddy covariance *in situ* measurements. In Figure 3.11 we show how the soil temperature is affected by micro-topography. The water table in the *Microtopography* model version lays for longer time above the surface (in average).

In the *Single bucker* model version, instead, the water quickly runs off out of the system. The drier soil of the bucket model responds differently to the radiative forcing, due to a different heat capacity of peat and water, and a different albedo. This causes the soil temperature to rapidly increase as soon at the water table drops below the surface. The same phenomenon happens in the *Microtopography*, but later on in the simulation. The increase in temperature is thus dumped, and it reaches its maximum ($\simeq$15^{o}C) later. The dynamics of the temperature is significantly nearer to the eddy covariance measurements than the dynamics of the soil temperature driven by the

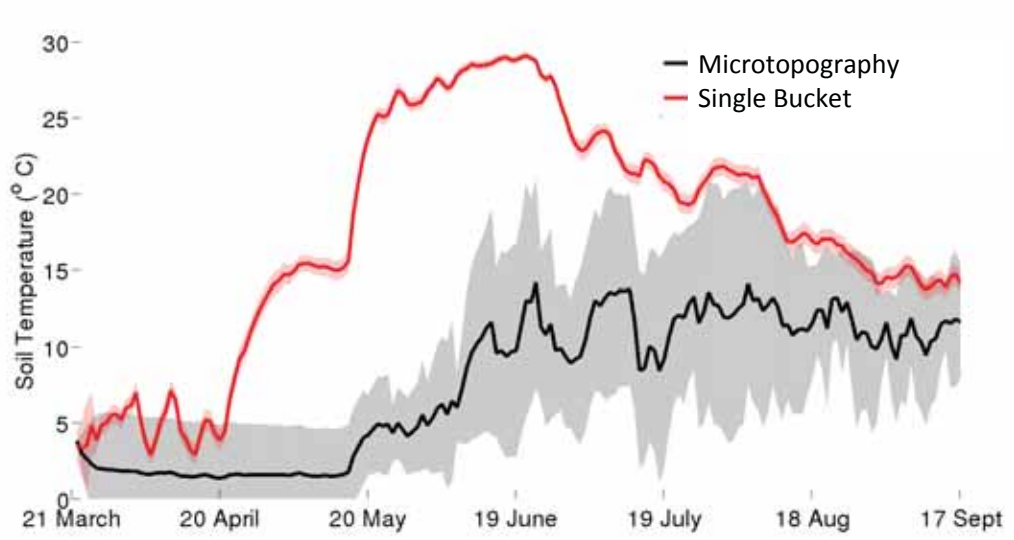

Figure 3.11: Dynamics of soil temperature. The figure shows a comparison between the *Microtopographic* version of the model (black line), and the classical *Single bucket* version (red line), coupled with an atmospheric box model. The soil temperature therefore changes as the soil characteristics do. In particular, the dynamics of the water table influences heat capacity and albedo of the soil, which in turn change latent and sensible heat fluxes between soil and atmosphere. The soil representation including micro-topography enables the model to better represent atmospheric temperature.

bucket soil model, if we compare the results with Runkle et al. (2014).

3.3.5 Sensitivity analysis

We test our model with a different set of parameters. We call *Standard configuration* the parameter values we used in the previous Sections.

We first test our model varying the grid size. In the previous paragraphs we compared the *Standard configuration* with number of grid cells $N = 10^6$, and a classical single bucket model, i. e. $N = 1$, and because of different water table behaviors we explained large differences in methane emissions. We gradually increase the number of grid cells, and compute the cumulative methane emissions over the whole season. In Figure 3.12 we show how the cumulative emissions increase almost linearly if $N \leq 10$. If we increase further the number of cells, the cumulative emissions stabilize, even slightly

decreasing if $10 < N \leq 100$. We explain this difference in behavior as the water table position dynamics changes if the number of grid cells increases. In particular, the water is retained within the system as the number of hydrological interactions between the different grid cells increases, and the water table lays more and more in proximity of the average soil surface. This change explains the drastic increase in emissions as $N \leq 10$. By $N > 10$, instead, the water table behavior asymptotically approaches water table dynamics for $N = 10^6$, i. e. for model resolution of 1 m, hence changes in cumulative emissions are not significant anymore. We nevertheless chose this resolution in the *Standard configuration*, because such resolution is approximatively the dimension of the micro-topographic features in the field, and the purpose of our model was not only to compute greenhouse gas emissions, but also to infer the general influence of an accurate micro-topographic representation on peatland properties.

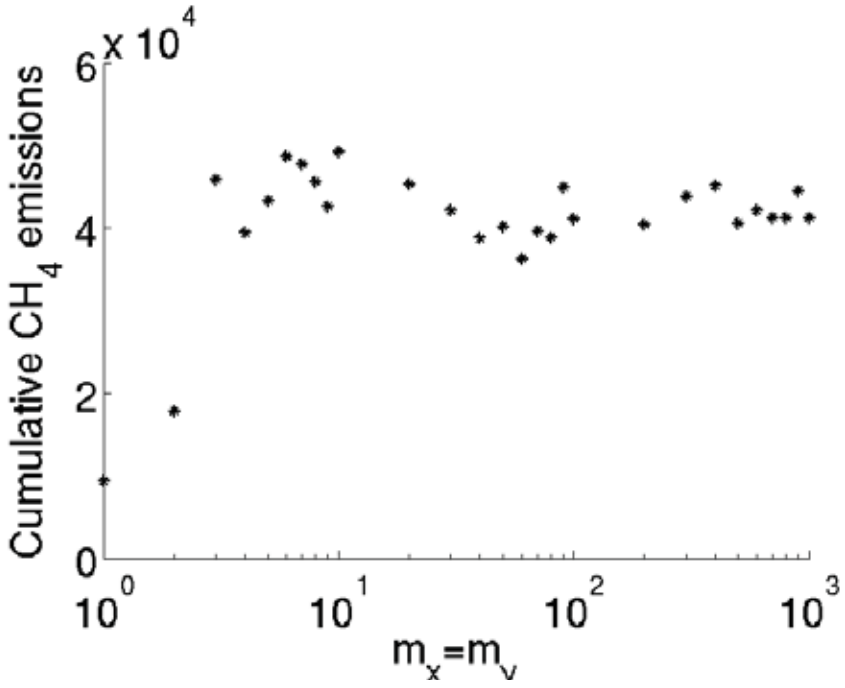

Figure 3.12: Figure shows the dependence of the cumulative methane fluxes computed over the whole warm season on the grid size of the microtopogrpahic model. The x axis shows the squared root of the number of cells N, as $\sqrt{N} = m_x = m_y$. Let us note that x axis is on a logarithmic scale. We see how the cumulative methane emissions change greatly if $\sqrt{N} \leq 10$, but they quickly stabilize as the number of grid cells increases. This phenomenon is mirrored by the average position of the water table dynamics, which by increasing N asymptotically approaches the water table dynamics for $N = 10^6$.

Among other parameters, drainable porosity $s_{i,j}$ in Equation 3.5 has a direct impact on water table position and therefore indirectly on methane emissions. We chose the amount of water the peat soil can retain in the *Standard configuration* baed on Kolka

et al. (2011). This parameter can vary greatly in different peatlands, and therefore the values in our *Standard configuration* are a susceptible assumptions we need to test. In order to assess the model sensitivity to this parameter we make drainable porosity uniform over the whole region, i. e., not we do not distinguish between hummocks and hollows. We changed $s_{i,j}$ uniformly at steps of 0.1 from 0.5 to 1.0, and we see how water table changes its position. Average position is generally lower in respect to the *Standard scenario* dynamics, but the differences are not significant, nor we can see any effect in methane emissions.

3.4 Summary and conclusions

We presented a novel model for peatland micro-topography working at 1 m resolution, fine tuned with field data from the Ust-Pojeg mire complex in the Komi Republic, Russia. In order to correctly represent the peatland characteristics we use elevation data collected on site of by a team of the Institute of Soil Science of Hamburg University. We fit the histogram of the elevation data with a generalized 3-parameters gamma distribution, $f_A(x)$ in Equation 3.31, and a Kolmogorov-Smirnoff test does not reject the null hypothesis, i. e. the hypothesis that data and $f_A(x)$ belong to the same distribution. We initialize the model elevation randomly picking a value from $f_A(x)$, and we also assign to each grid cell other quantities inferred from site data, such as peat profile and slope. We compute the water balance for each grid cell, taking into account different hydrological features, such as parameters for Manning's and Darcy's later flow (Equations 3.15 and 3.14 respectively). By computing the water balance at 1 m resolution, the complex hydrological interactions affect the average water balance, as we show by comparing results of the model with micro-topographic representation and the results of model in a simple single bucket configuration, where all quantities are averaged over the whole peatland surface. By comparing the two models with field data we see how the model with micro-topography representation performs better in representing the peatland water balance.

We couple the surface model with a process-based model for methane emissions (Walter and Heimann, 2000). Water table directly influences the depth of the oxic zone, i. e. the zone where methane fluxes can be oxidate, and therefore released as carbon dioxide. Hence, changing the water balance has a direct effect on fluxes, and we show how accounting for micro-topography representation changes dramatically the ecosystem-scale methane fluxes. The methane emission responses to water table position are highly nonlinear, and therefore slight differences in water table depth may lead to dramatic changes in fluxes. By not accounting for micro-topography in a

classical single bucket model, as the water table depth drops faster, methane emissions are much lower than in the configuration with micro-topography.

We also couple the model with a simple one-box model for the planetary boundary layer, modified from D'Andrea et al. (2006), in order to assess possible micro-topographic influences on local energy balance. In the uncoupled configuration we forced the model with CMIP5 time series of temperature and NPP. By coupling the model with an atmospheric model, instead, we dynamically compute both atmospheric and surface temperature, and we substitute the external forcing with in situ measurements of solar incoming radiation. Once again, the difference in water table position affects the energy balance if we consider micro-topography or simply a classical single bucket model. The persistently higher (in average) water table in the configuration with micro-topography, due to the difference in water and soil heat capacity, leads to large differences in the local energy balance. In particular, the earlier drop in water table leads to an early increase in soil temperature, being the surface drier and exposed to incoming solar radiation. The sudden increase of soil temperature happens instead later in the season in the model with micro-topographic representation.

We also performed a sensitivity analysis on model parameters. The model resulted particularly sensitive, as expected, to grid cell size. In particular, we see how the cumulative fluxes depend on this key parameter. The model is size dependent for a number of cells N lower than 100, i. e. for grid size lower than 100 m. Using a finer grid cell the computational time for calculation increases, but there is no evidence of any real improvement or change in water table dynamics and therefore in methane emissions or in energy balance. On the other hand, we chose to keep the grid size of 1 m because it is approximatively the size of micro-topographic features in real peatlands.

In order to upscale fluxes from the peatland one way could be to reduce the computational expensiveness of the model by increasing the grid size. On the other hand, the amount of parameters would still be quite large, and for consistency issues integrating a micro-topography model in a larger land surface model, or a DGVM, even drastically coarsening the grid-size, is not feasible. Another way involves the use of pattern recognizers, such as Minkowski densities (Mecke, 2000), and their properties which could be of help in identifying the main processes relating the micro-topographic features to the landscape-scale methane emissions. We will explore the possibility to develop such a parameterization in the next Chapter.

The model we presented could be further developed, in order to answer further research questions. One interesting development would involve expanding the model to the fen system which in the Ust-Pojeg mire complex lays near to the elevated bog

ecosystem we modeled in the present Chapter. The fen system has different ecological features. A model able to describe the interactions between the two ecosystems could definitely help to investigate properties of the water flow, as pointed out by recent studies (Runkle et al., 2012, 2014). The model could further explore the relations among ecosystems by modeling also the transition zone between the proper peatland and the forest. Other research areas of great interest are the implementation of nutrient flow, as well as a more consistent modeling plant ecological communities.

Other directions of developments include expanding the array of climatic forcing. It is of interest the generalization of the findings presented in this Chapter to future projections. This is possible by forcing the model with the output of the CMIP5 runs from the MPI-ESM model for both temperature and NPP, in order to investigate the response of the micro-topographic model coupled to the process-based model for methane emissions. Changes in temperature would likely lead to an increase in methane emissions, but the magnitude of this effect is still unknown, and in order to tackle such a complex problem a fine tuned micro-scale model working at the peatland-scale is a valuable tool. Analogously, we could force the model with different climatic conditions in order to adapt it to different peatlands in different environments. The flexibility of the approach has its limitation in the amount of small-scale data needed for the calibration, and therefore further developments in generalizing the results to other ecosystems shall be supported by analogous efforts in field measurements. On the other hand, a more general initialization could lead to less precise results, but they could still be interesting on the statistical and qualitative point of view. In this respect, it could be interesting to couple the model with a carbon accumulation model, and to explore also possible large-scale effects on carbon storage in peatlands, e. g. using extensive datasets for not boreal peatlands, such as the ones developed by Loisel and Yu (2013). The next step in this direction involves the coupling of the model to a peatland development module, similar to the one developed by Baird et al. (2012); Morris et al. (2012).

In general, we think that the overall good agreement between the micro-topographic model and data show how fundamental effects small-scale surface heterogeneities can have in predicting landscape-scale hydrology, methane emissions, and energy balance.

Chapter 4

Upscaling micro-topography using Minkowski functionals

Minkowski functionals are a useful tool to measure patterns, as they can help to quantify emergent landscape-scale properties arising from local, small-scale interactions. In the previous Chapters we showed how such small-scale interactions can be fundamental in reproducing large-scale properties. In Chapter 2 we showed that the overall water balance and the climatic response of the system can be better represented by taking into account the heterogeneities of the system with the help of a stochastic model. In Chapter 3, instead, we developed a model for local micro-topography for a typical boreal peatland and we showed how the small-scale interactions affect the hydrological representation, and in turn, greenhouse gas emissions and energy balance. In this Chapter we extensively analyze the spatial output of the previously presented models with the tools we derive from the Minkowski functional theory, and we are able to identify large-scale pattern properties. We are also able to link the behavior of some local features to the seasonal dynamics of greenhouse gases. Regarding the model for peatland micro-topography, we develop a simple and novel parameterization which is computationally feasible and significantly improves the output of the model running without micro-topography. This is a first step towards a comprehensive method to fill the general scale gaps in climate-biosphere interactions.

4.1 Introduction

A challenging problem in climate modeling is how to deal with interactions and feedbacks across a multiplicity of spatial scales, and how to improve our understanding of the role played by small-scale phenomena in the climate system. In the general framework of biogeosphere and climate interactions, many studies tackled the complex effects

of climate forcing on small-scale features of soil and vegetation, from self-organized vegetation patterns to early warning signals for critical transitions (Scheffer et al., 2009). Simple reaction-diffusion equations forced by different precipitation levels, along with other disturbances, are thought to be some of the mechanisms which drive pattern formation in arid and semiarid ecosystems (von Hardenberg et al., 2001; Kletter et al., 2009; Dijkstra, 2011), or that induce pattern formation along with self organization (Sheffer et al., 2013). Also in other ecosystems, many studies proposed such a top-down approach to explain local small-scale characteristics of the biogeosphere, with climatic forcing influencing and driving formation and evolution of different soil surface heterogeneities and small-scale vegetation patterns (Shur and Jorgenson, 2007; Couwenberg and Joosten, 2005; Rietkerk and van de Koppel, 2008). Other studies tried to address the complex problem of feedbacks across different spatial scales in various ecosystems: how do the small-scale features, whose formation depends on the climatic conditions, influence the local and regional climate (Rietkerk et al., 2011)? Many efforts addressed the water cycle in drylands, where water recycling from vegetation may play an important role in the local water budget (Dekker and Rietkerk, 2007; Janssen et al., 2008). In particular, Baudena et al. (2013) showed that the amount of water transferred through transpiration may change up to 10% if one considers different vegetation patterns, even with the same biomass and the same spatial scale.

Such nonlinear behaviors also influence the carbon cycle of northern peatlands, as we showed in Chapter 3. In Chapter 2 we addressed this issues of scale interactions in permafrost environments, such as the polygonal landscape in some tundra ecosystems, and in Chapter 3 we showed how micro-topography affects methane emissions in a typical northern peatland, with the model tuned with data from the Ust-Pojeg mire complex in the Komi Republic, Russian Federation. Recent studies showed how the greenhouse gas fluxes (in particular methane) strongly depend on the micro-topographic features of such environments (Sachs et al., 2010; Couwenberg and Fritz, 2012). This property of methane emissions could potentially constitute a large local and even regional feedback to the climate system, which is neglected in the current Global Circulation Models (GCMs), as shown e. g. in Baird et al. (2009a). The issue is of particular interest in northern peatland ecosystems, because of the large amount of carbon stored in the soil. It is essential to consider the local heterogeneous behavior of the system components in order to properly estimate water and carbon balances, but it is computationally feasible to represent such micro-scale features only in local mechanistic models (i. e., Nungesser, 2003), with a fine grained resolution ($10^{-2} - 10^{0}$ m), and therefore able to resolve both the small-scale features responsible for the nonlinearities in fluxes and the local processes which arise by considering such small scales.

Land surface models such as JSBACH (Raddatz et al., 2007), the Dynamical Global Vegetation Model (DGVM) included in the Earth System Model MPI-ESM, work at a spatial resolution analogous to the atmospheric one, which is of about 50 x 50 km at the finest feasible scale. Even a geometric tessellation approach, such as the one presented in Chapter 2 is computationally too expensive, because of the complexity of the features represented at the working scale of the model. A more complex model including explicit representation of hydrology, as the one presented in Chapter 3, is computationally even more demanding, and therefore it is not feasible to be included directly in any DGVM. Another reason is that an improvement in the resolution of some particular model features (i. e., the polygonal tundra or the micro-topography in peatlands) would lead to inconsistencies in the spatial representation of the rest of the grid cells, which still would work at the grid cell spatial scale, and have a very coarse spatial representation (e. g., the tiling approach). On the other hand, we showed how the predicted fluxes of greenhouse gases may be underestimated or generally wrongly represented by neglecting the information coming from the small-scale surface heterogeneities.

The problem is similar to the one of coarse-graining in physics of complex systems, where starting from a fine grained description of a system with a large number of elements one tries to infer large-scale properties by coarsening the resolution of the model, ultimately finding an effective theory able to preserve the information useful for a final prediction (DeDeo, 2011). Because of the small-scale interactions that drive the hydrological behavior of the system, it is difficult to upscale the local dynamics neglecting those local interactions. We propose a novel method to fill the scaling gap from local mechanistic models to large-scale mean field approximations, using the output of the local fine grained model to tune and modify the coarse grained bucket model, in order to upscale the local information ($10^0 - 10^1$ m) to the landscape-scale (10^3 m) and above.

Minkowski numbers and functionals (Mecke, 2000) are useful geometric measures for quantification of patterns in images. They have been widely used in the analysis of images of heterogeneous soil patterns, to quantify properties resulting from crack processes in the soil (Vogel et al., 2005), to quantify soil structure in different generic soils (Vogel et al., 2010), and to describe properties in porous media (Lehmann et al., 2006). They have been first introduced in the analysis of Arctic and Subarctic patterns by Roth et al. (2005), where they have been applied in the analysis and the quantification of pattern properties at different scales in aerial images from the polygonal landscape in Howe Island, off the Alaskan Arctic coast. In comparison to other methods for image analysis (i. e., Skurikhin et al., 2013) they provide not only information on the area

covered by different surface classes, but also quantification of other properties of the patterns, such as for example the interconnectivity of the pattern patches. What we propose here is a method which could potentially be applied to every kind of surface heterogeneity, being it independent on the physical processes generating the pattern.

We analyze the Minkowski densities of black and white patterns we obtain by running the models we presented in the previous Chapters, and we show how to obtain different and further information on the pattern dynamics. As we analyze patterns from the models, we are able to investigate properties which are not directly evident from analyzing photographs and satellite images, i. e., water table position within the soil, or even greenhouse gas fluxes. We also show an example of a possible upscaling method, where we compute the Minkowski functionals for black and white images from the output of the micro-topographic model we described in Chapter 3. We use the position of the water table relatively to the surface as a variable, and thus we identify three different surface classes, analogously to what we did to infer methane emissions from the polygonal tundra in Chapter 2. We then show how a simple parameterization of pattern properties inferred from the Minkowski functionals dynamics can significantly improve the representation of methane fluxes. Such an example is a first step towards a comprehensive representation of the micro-topography effect in northern peatlands under different climatic forcing.

4.2 Theory

We aim to analyze the output of the models presented in the previous Chapters with Minkowski functionals (and densities in particular) at each time step of the model. We therefore use two models as input sources. The first model is a stochastic spatial tessellation representing a typical low-centered polygonal tundra landscape, and it is able to compute spatial patterns of water table variations over the 90 days of the warm period in such high-latitude environments. The latter model, which represents an idealized peatland at a resolution of 1×1 m, computes water table level, surface wetness, methane and energy fluxes, thus resolving surface microrelieves, such as hummocks and hollows. For both models, we plot the model output for each measured quantity, such as the water table level, for the whole region considering what happens at the micro-relief scale. Looking at the Minkowski functionals we are able to infer spatial characteristics and to quantify pattern properties. It can also be a way to transfer information of the temporal dynamics of spatial patterns across scales. In this Section we present the theory and the concepts of *Minkowski functionals*, the normalization leading to the

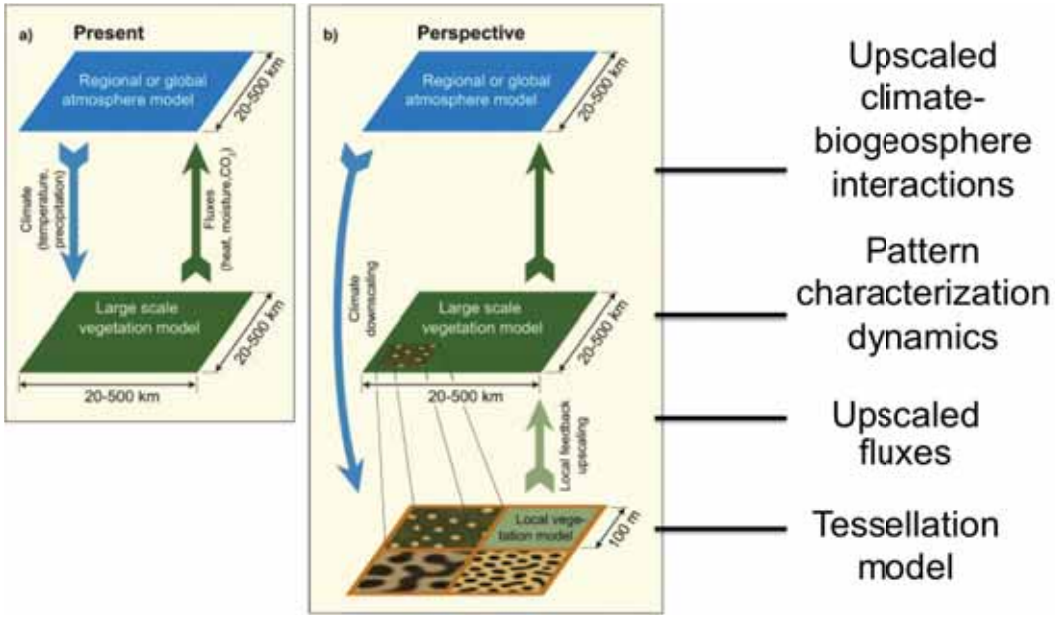

Figure 4.1: Modified from Rietkerk et al. (2011). The figure shows a schematics of the main challenges of scale interactions in climate modelling. In the previous two Chapters we were able to develop robust tessellation models, which work at the landscape-scale (first square below, in panel (b)). Such models, while able to upscale local feedbacks and fluxes, can not be directly linked to a model working at regional or global atmospheric scale, because of their intrinsic complexity, and because of consistency issues with the other processes described in a GCM. What we propose in this Chapter is a characterization of the local patterns described by the tessellation models, which can lead to a consistent and feasible general upscaling technique.

definition of *Minkowski densities*, and the description of a novel parameterization of surface wetness based on the Minkowski densities analysis.

4.2.1 Minkowski Functionals

Geometric functionals, known as Minkowski functionals or intrinsic volumes (curvature integrals) in integral geometry, may be introduced as integrals of curvatures using differential geometry of smooth surfaces. Let X be a compact domain in $\mathbb{R}^d$ with regular boundary $\partial A \in \mathcal{C}^2$ and $d-1$ principal radii of curvature $R_i (i = 1, ...d-1)$. The functionals $W_\nu(X)$, with $\nu \geq 0$, can be defined by the surface integrals

$$W_{\nu+1}(X) = \frac{1}{(\nu+1)\binom{d}{\nu+1}} \int_{\partial A} S_\nu \left(\frac{1}{R_1}, ..., \frac{1}{R_{d-1}} \right) \mathrm{d}\mathcal{S} \tag{4.1}$$

where S_ν denotes the ν-th elementary symmetric function and $\mathrm{d}\mathcal{S}$ the $(d-1)$-dimensional surface element. Although the Minkowski functionals are introduced as curvature integrals, they are well defined for polyhedra with singular edges. Therefore,

one can define these functionals naturally for lattice configurations. It is convenient to normalize the functionals

$$M_\nu(X) = \frac{\omega_{d-\nu}}{\omega_\nu \omega_d} W_\nu(X),\ \nu = 0, ..., d \tag{4.2}$$

using the volume ω_d of a d-dimensional unit sphere: $\omega_d = \pi^{d/2}/\Gamma(1 + d/2)$, namely $\omega_0 = 2$, $\omega_1 = \pi$, and $\omega_1 = 4\pi/3$. We are interested in a 2-dimensional problem, and more concretely, we are interested in 2 dimensional images: $\nu = 0, 1, 2$. In this case the first member of the family of Minkowski functionals is simply the mass of the structural unit, which in 2D is its surface area:

$$M_0(X) = A(X). \tag{4.3}$$

The other Minkowski numbers are defined through integrals over the boundary ∂X of the object X. For $d = 2$ the first integral measures the total length of the boundary,

$$M_1(X) = \int_{\partial X} \mathrm{d}s = L(X) \tag{4.4}$$

and the second integral measures the total curvature of the boundary

$$M_2(X) = \int_{\partial X} \frac{1}{r} \mathrm{d}s = C(X) \tag{4.5}$$

where ds is the boundary element and r is its radius of curvature, positive for convex and negative for concave shapes. Notice that the curvature integrals equals 2π for each closed convex boundary (objects) and -2π for each closed concave boundary (holes). Thus, M_2 is closely related to the Euler number χ which counts the number N_{hole} of holes within the objects, which are also referred to as loops. In particular:

$$\chi(X) = N_{object} - N_{hole} = \frac{1}{2\pi} M_2(X). \tag{4.6}$$

This last quantity is a dimensionless number, that measures the connectivity of the pattern, while M_1 and M_0 represent physical quantities, and have therefore units $[L]$ and $[L^2]$ respectively.

Minkowski densities have some advantages if compared to other pattern characterizes. According to Hadwiger's theorem (Hadwiger, 1957) cited in Mecke (2000), all other properties of a given pattern, which are motion invariant, continuous, and additive, can be directly derived by the Minkowski functionals. This characterization theorem asserts that any additive, motion-invariant and continuous functional that depends on the form of the object alone, $\phi(X)$, can be derived as a linear combination

of the $d+1$ Minkowski functionals:

$$\phi(X) = \sum_{k=0}^{d} c_k M_k \tag{4.7}$$

where coefficients $c_k \in \mathbb{R}$ depend on the particular property $\phi(X)$, but not on the object X. The completeness of the Minkowski functionals is the theoretical background for using these quantities as pattern characterizers and not other ones. The most important property for our purposes is additivity, i.e., the functional of the union A plus B of two domains A and B is the sum of the functional of the single domains subtracted by the intersection

$$M_\nu(A \cup B) = M_\nu(A) + M_\nu(B) - M_\nu(A \cap B). \tag{4.8}$$

This relation generalizes the common rule for the addition of the volume of two domains to the case of a general morphological measure, i.e. the measure of the double-counted intersection has to be subtracted.

Other properties of the Minkowski functionals are motion invariance and continuity. Such properties assure that results of the computations do not change if the analyzed object is moved or rotated (motion invariance), and that small changes of the analyzed objects correspond to small changes in the measure (continuity). In order to eliminate the influence of the area of the image one can introduce a normalization with respect to the total area $A(\Omega)$, defining then the so called Minkowski *densities* m_ν as:

$$m_\nu := \frac{M_\nu(X \cup \Omega)}{A(\Omega)} \tag{4.9}$$

In this Chapter we use the Minkowsi densities to analyze the spatial pattern we obtain by running the two models we presented in Chapter 2 and 3, in order to describe the large-scale properties of the landscape-scale patterns. In Table 4.1 we show a summary of the Minkowski densities we will use later in the next Sections.

The Minkowski densities are integral quantities, and therefore they only deliver information over the whole domain. In order to investigate what happens at the smaller scale, as well as to explicitly distinguish between different spatial structures, we need to use different methods of mathematical morphology, namely erosion and dilation processes. Using such techniques one could define other quantities, called Minkowski *functions* (Vogel et al., 2010), but such further applications go beyond the scope of the present Chapter. We show an insight on the Minkowski *functions* in Appendix B.

In Appendix A we describe the algorithm we use to compute the Minkowski densities, which we modified from the original C++ algorithm developed by H. J. Vogel

Symbol	Meaning	Units
m_0	Area density	$[L^{-2}]$
m_1	Boundary length density	$[L^{-1}]$
m_2	Euler number	$-$

Table 4.1: The Table shows the Minkowski densities in 2D. Minkowski functionals are normalized over the image domain obtaining the Minkowski densities, allowing possible comparisons between densities from different images.

(QuantIm library, available at www.quantim.ufz.de).

4.2.2 Minkowski densities and upscaled methane emissions

The general purpose of the new method we introduce is to upscale information from the local to the atmospheric scale (as in Figure 4.1). With a mechanistic and local model we are able to simulate the dynamics of local observables in specific environments. We showed how the local behavior and micro-topographic surface properties are important for methane emissions in northern peatlands in Chapter 3, and in particular we demonstrated how better hydrological parameterization can reproduce water table measurements. Methane emissions depend on water table position. We can identify different surface types, as we did in Chapter 2, depending on the relative position of the water table W_t and the surface S:

$$\begin{aligned} S - W_t &> \epsilon_a && \Rightarrow && \text{Wet surface} \\ -\epsilon_b \leq S - W_t &\leq \epsilon_a && \Rightarrow && \text{Saturated surface} \\ S - W_t &< -\epsilon_b && \Rightarrow && \text{Dry surface} \end{aligned}$$

where, analogously to what we did for the polygon centers in Chapter 2, following Couwenberg and Fritz (2012), we assume:

$$\epsilon_a = 15 \text{ cm} \tag{4.10}$$

$$\epsilon_b = 10 \text{ cm} \tag{4.11}$$

because of the importance of such thresholds for methane emissions. By performing image analysis of black and white patterns from the micro-topographic model, we are able to describe the dynamics of the so-defined surface classes. In particular, the first

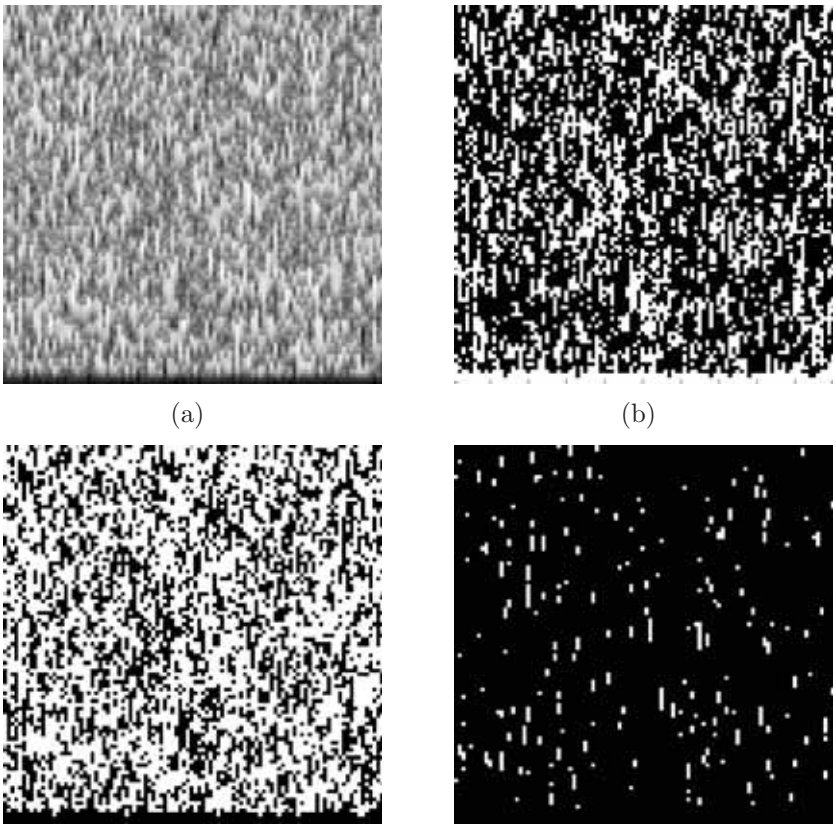

Figure 4.2: Figure shows the black and white image processing before the computation of Minkowski densities. The original image is the output from the model described in Chapter 3. Panel (a) shows a zoomed region (100 x 100 m) of a greyscale image of the water table position in respect to the surface for each grid cell. From this figure we can identify different surface classes, i. e. *Dry surface* in panel (b), *Saturated surface* in panel (c), and *Wet surface* in panel (d). We then analyze the white phase for each surface class, computing the three Minkowksi densities for each image.

Minkowski density m_0 provides the fraction of the total surface covered by a certain pattern. We assume the *Saturated surface* to be the surface class which dominates the methane emission dynamics, as the water table being approximatively at the surface level prevents most of the oxidation to happen.

After obtaining the seasonal behavior of the desired surface class, we aim to parameterize the dynamics of m_0 for the *Saturated* surface class with a fractional number $q(t)$, which represents the fraction of the total surface which is saturated at each time step. In Chapter 3, we showed how a single bucket model is inadequate to represent methane fluxes because of the lack of representation of complex hydrological interactions. This information translates in a different water table behavior which in turns controls methane emissions and energy balance. By knowing the fraction q of saturated surface at each time step t we could implicitly subdivide the surface of the bucket

model A in unsaturated surface U_{Sat} and saturated surface S_{at}:

$$A = (1 - q)U_{Sat} + qS_{at} \tag{4.12}$$

We know the position of the water table in S_{at} being between $-\epsilon_b <= W_t^{sat} <= \epsilon_a$, which is given by the definition of the saturated surface, and therefore we assume:

$$W_t^{sat} = -\epsilon_b + (\epsilon_a + \epsilon_b)r \tag{4.13}$$

where r is a random number. The position of the water table in U_{Sat}, instead, we assume to be the one computed by the single bucket model without micro-topography, i. e., W_t. Therefore, we compute the methane fluxes as function of the water table assuming a linear relationship between emitting area and methane fluxes:

$$F_{CH_4} = (1 - q)F_{CH_4}^{uns}(W_t) + qF_{CH_4}^{s}(W_t^{sat}) \tag{4.14}$$

where F_{CH_4} are the methane fluxes from the whole region, $F_{CH_4}^{uns}$ the fluxes from the unsaturated area U_{Sat}, and $F_{CH_4}^{s}$ the fluxes from the saturated area S_{at}. We only consider methane fluxes as function of the water table position, since the other variables on which F_{CH_4} depends are the same in $F_{CH_4}^{uns}$ as in $F_{CH_4}^{s}$. Fluxes are computed using the process based methane emission model developed by Walter and Heimann (2000).

4.3 Results and discussion

We use the algorithm computing Minkowski densities developed by Roth et al. (2005), and later modified by Overduin in 2009 in a MATLAB code. We use as input images from spatially explicit models. The methodological difference from the approach used by Roth et al. (2005) is that we compute the Minkowski densities not from a photograph of the actual system, but from model output. This approach allows us not only to identify patterns in processes by looking at particular snapshots, but also to analyze the seasonal dynamics of the pattern itself. On the other hand, we are also able to investigate some patterns which can not be necessarily directly evident in photographs, i. e. the water table position in the soil, which we showed in Chapter 2 and 3 to be an important indicator of greenhouse gas emissions.

4.3.1 Minkowski measures and the polygonal tundra

We start our analysis of model output with the geometrical patterns in the polygonal tundra we presented in Chapter 2. In Figure 4.3 we show a realization of the Poisson-

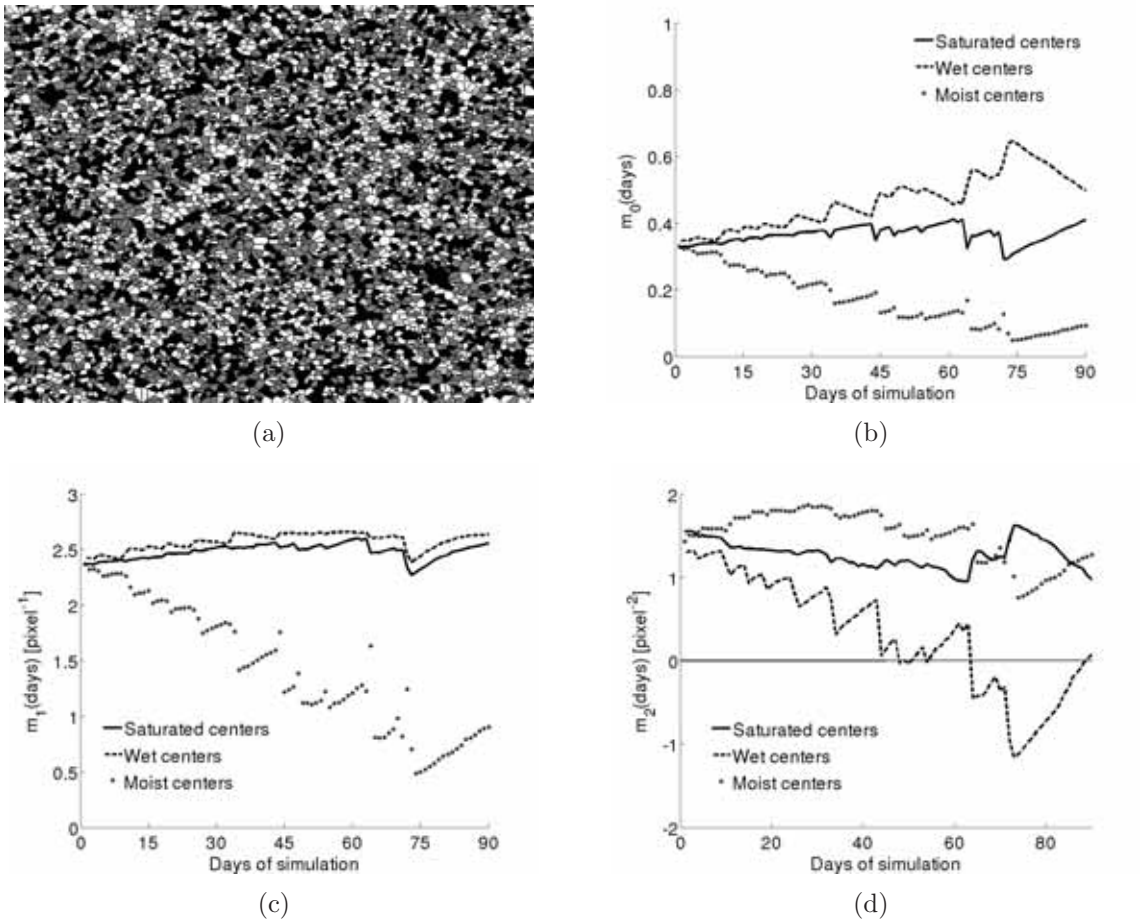

Figure 4.3: Figure shows the Minkowski densities for the white phase of the binary representation of water table pattern of a northern peatland. In panel (a) we show a gray scale image of a snap shot for the Voronoi diagrams representing low-center polygonal tundra. We compute the Minkowski densities for each surface class for the polygon centers, *Wet*, *Moist*, and *Saturated*. In panel (b) we show the seasonal dynamics for m_0, or the area density. Analogously, we show m_1, the boundary length density, and m_2, the Euler number, in panels (c) and (d) respectively. The dynamics of the m_1 for *Wet* and *Saturated* centers, displayed in panel (c) are similar.

Voronoi Diagram where the different colors reflect different positions of the water table relative to the surface. In particular, as we discussed in Chapter 2, we discretize the position of the water table in respect to the surface in three different classes for the polygon centers, which we can recall as being:

$$
\begin{aligned}
S - W_t > \epsilon \quad &\Rightarrow \quad \text{Wet centers} \\
|S - W_t| \leq \epsilon \quad &\Rightarrow \quad \text{Saturated centers} \\
S - W_t < -\epsilon \quad &\Rightarrow \quad \text{Moist centers}
\end{aligned}
$$

where, following Sachs et al. (2010), we assume $\epsilon = 10$ cm. We analyze the dynamics of the densities over the 90 days of simulation, and in Figure 4.3 we show the results for *Wet* centers (dashed lines), *Saturated* centers (solid lines), and *Moist* centers (dotted lines). Panel (b) shows the area density dynamics of the different surface classes. The pronounced variations depend on the precipitation events, which occur sparsely during the season. As we see in the more explicit computation in Chapter 2, the area covered by saturated centers stays pretty much constant over the whole season, with a relative increase towards the end of the simulation. It is worthy to notice that we show here the analysis of images from one particular realization, whereas lines in panel (b) in Figure 2.6 are ensemble averages of 30 model simulations.

Relative area of *Wet* centers increases almost constantly till the end of the season, when a drastic reduction in the area covered by this surface class takes place, as the water table drops because of lateral runoff. Recalling the physical properties of the model, towards the end of the season the water table is in average above the thaw depth. This property increases the lateral runoff from the polygonal centers to the rims, and it becomes an important feature in the the water balance. The *Moist* centers dynamics, conversely, displays a constant decrease in the 90 days of simulation, which stops as the thaw depth averagely drops below the water table level. The dynamics of the boundary length density m_1 for *Saturated* and *Wet* centers are very similar, even though the dynamics of the two area densities are quite different. We can explain this phenomenon by considering that most of the polygonal centers belong either to the *Saturated* or to the *Wet* surface class. Therefore, the length of the boundary has to be similar, as the two patterns almost cover the whole landscape. On the other hand, the boundary length for *Moist* centers drops because of the constant decrease of the relative density area. This feature is confirmed by the dynamics of m_2, which measures the connectivity of the patches belonging to the analyzed pattern. m_2 for *Moist* centers lays consistently above the 0 line, as there are never enough polygons belonging to the *Moist* surface class to reach connectivity. This phenomenon is clear in the dynamics of m_2 for *Wet* centers. The decrease in m_2 for *Wet* centers parallels the increase in area density m_0, before the water table depth drops at the end of the simulation. This phenomenon causes some *Wet* polygons to change class becoming *Saturated*. On the other hand, m_2 for *Saturated* centers stays above the 0 line (as well as m_2 for *Moist* centers), because, even though many polygonal centers are *Saturated*, they never reach a number large enough for the m_2 to change sign.

4.3.2 Permafrost patterns under different climatic forcing

As we did in Chapter 2, we changed the climatic forcing and looked at the system response to different precipitation levels. The precipitation input is the main input of water in the water balance, and it is defined by Equation 2.9, which we recall here:

$$P = \begin{cases} R_p \sin(\frac{t+T}{6T\pi}) & \text{if } 30 < t < 90 \\ 10\frac{\text{mm}}{\text{day}} \sin(\frac{t+T}{6T\pi}) & \text{otherwise} \end{cases} \tag{4.15}$$

where R_p is the size of the the maximum rainfall in the central part of the season. We choose three different values for three scenarios: in the *Standard* scenario $R_p = 30$ mm/day, whereas $R_p = 60$ mm/day and $R_p = 15$ mm/day in the *Wet* scenario and in the *Dry* scenario respectively. In Figure 4.4 we show the comparison of the Minkowski density dynamics in the three different scenarios for the three surface classes of the polygon centers. The first row displays the seasonal dynamics for m_0, the second one the seasonal dynamics for m_1, and the third row the seasonal variations of m_2. The first column displays the complete Minkowski densities analysis for *Saturated* centers in the three different precipitation scenarios, the second column the Minkowski densities for *Wet* centers, and analogously the third column the Minkowski densities for *Moist* centers. In the *Dry* scenario, the *Saturated* centers seem to be more numerous than in the other scenarios. This is not in contradiction with the results of Chapter 2, where the *Standard* scenario showed a larger amount of *Saturated* centers. This can be explained by the fact that in Figure 4.4 we only show results from one single realization, whereas in Chapter 2 we showed the dynamics of the average of 30 ensemble runs. The trend of the *Wet* scenario shows almost the disappearance of both *Saturated* and *Moist* centers, as in most of the polygons water table lays above the surface. The boundary length dynamics of *Saturated* and *Wet* centers are very similar, as we see in panels (d) and (e) especially in the *Standard* and in the *Wet* scenarios. This phenomenon can be explained by the fact that most of the polygons belonging to the *Saturated* class become *Wet* and vice versa. In the dry scenario we can observe a significant difference between the m_1 dynamics of *Saturated* and *Wet* centers, and this is because of the larger number of *Moist* centers that influence the boundary length of the pattern. In panels (f) and (c) we see how the dynamics of m_0 for moist centers in the dry scenario (red dotted line) leads to an increase also in the boundary length for both *Standard* and *Dry* scenarios at the end of the season.

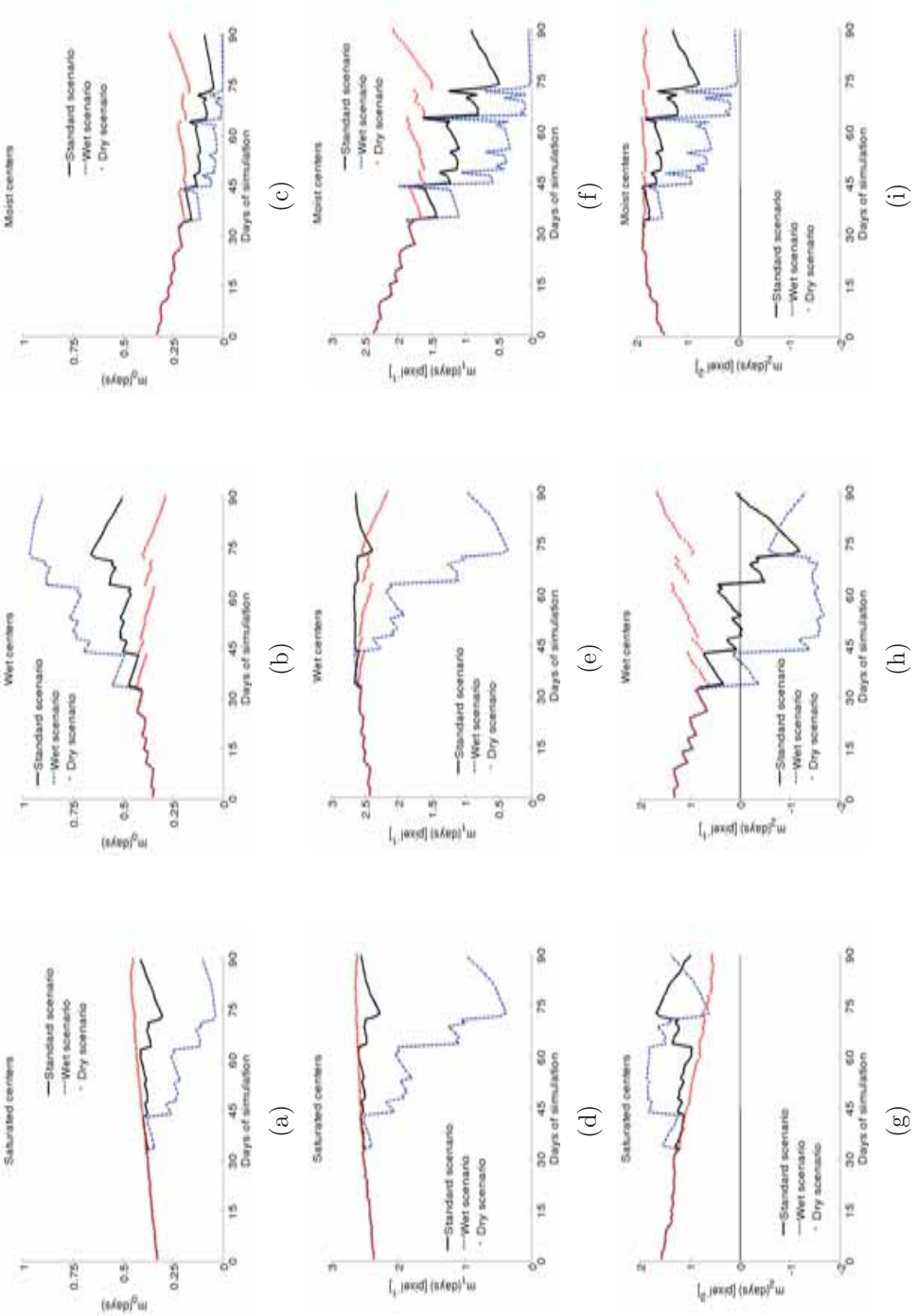

Figure 4.4: The figure shows the seasonal dynamics of the Minkowski densities $m_{0,1,2}$ for the three surface classes *Saturated*, *Wet*, and *Moist* for the polygon centers, depending on the position of the water table level in respect to the surface level. We compare the dynamics of the quantities under three different scenarios of climatic forcing, changing the precipitation input. The maximum amplitude of the rainfall events of the *Standard* scenario is doubled in the *Wet* scenario, whereas it is halved in the *Dry* scenario.

Because of the same reason the m_2 dynamics of *Moist* center, shown in panel (i), stays above the 0 line in all three scenarios. It reaches 0 only in the *Wet* scenario, because there are almost no *Moist* centers in the landscape, as we see in panels (c) and (f) (blue dashed line). It is similar to the *Wet* center dynamics in the *Dry* scenario and of *Saturated* center dynamics in all scenarios (panel (g)), as most of the polygons belong to other surface classes. In the *Wet* scenario (blue dashed line) the m_1 length density of the pattern boundary reaches very low values in both panels (d) and (e) (*Saturated* and *Wet* centers respectively) because almost the whole landscape is tessellated by *Wet* polygons, as the m_0 dynamics shows in panel (b). The dynamics of *Wet* centers in the *Wet* scenario is confirmed by the dynamics of the m_2 dynamics in panel (h), which in the second half of the simulation stays constantly below the 0 line, meaning the patches belonging to the pattern are interconnected.

In general, the amount of information we infer even from a qualitative analysis of the Minkowski densities completes the analysis of Chapter 2 of the modeled polygonal pattern.

4.3.3 Minkoski measures and northern peatlands

We repeat the experiment by using the spatial output of the micro-topographic model described in Chapter 3. Water table controls methane emissions since it modifies the depth of the oxic zone. By modelling this essential control more accurately, we aim to significantly improve the carbon cycle representation at different spatial scales. We start by analyzing the Minkowski densities for the 2D greyscale images of the water table patterns in respect to the surface for different days of the season. We vary the segmentation threshold g_0 at which we transform the greyscale image into a binary representation of the pattern. This process is quite straight-forward, since we perform the transformation by assigning a 0 value for the grid cells with $g < g_0$ (white pattern, or white phase), and 1 to the other ones (black pattern, or black phase). We compute the Minkowski densities using the algorithm we show in the Appendix A at each value of g_0, obtaining information on the pattern depending on the segmentation threshold. By increasing the threshold we increase the numbers of grid cells belonging to the white phase of the pattern.

The results shown in Figure 4.5 describe qualitatively how the pattern evolves during the season. We selected three representative snapshots within the 209 days of simulation at which we variated the g_0 threshold, and we computed the Minkowski densities. The number m_0, which represents the area density of the white phase, increases (as expected) monotonically by increasing g_0. The dynamics is similar in the

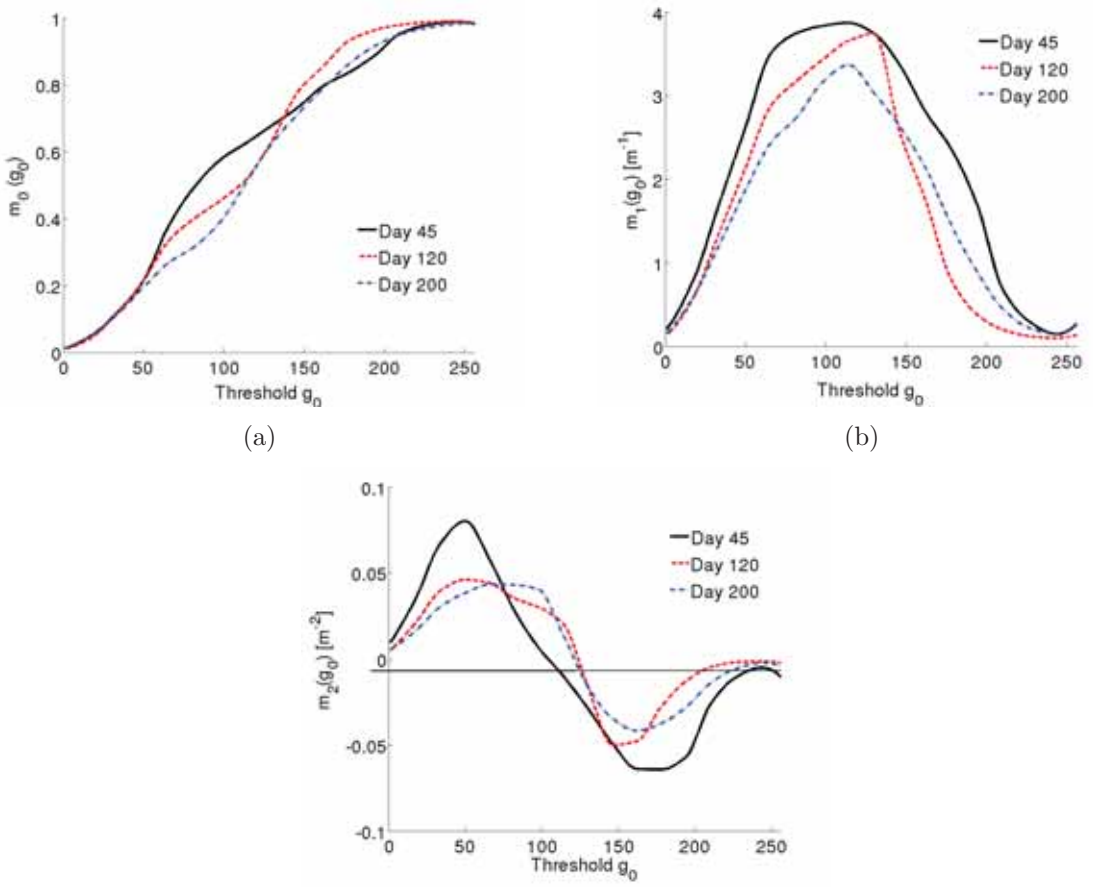

Figure 4.5: Figure shows the Minkowski densities for the white phase of the binary representation of water table pattern of a northern peatland. The different patterns are represented changing the segmentation threshold value g_0 Quantities m_0, m_1, and m_2 are shown in panels (a), (b), and (c) respectively. We chose 3 snapshots at three representative time steps in order to compare the dependence on the g_0 threshold.

three different snapshots, but it seems that the the saturation is reached earlier for the snapshot at the day 45 (dashed line) than what happens in the two other snapshot taken later in the simulation. This can be explained by the fact that at the beginning of the simulation the water table is generally largely above the surface because of the large water input from the snow melt. On the other hand, towards the hand of the simulation, the water table is generally below the surface. Instead, as we are explaining more extensively in the next section, the pattern is more complex towards the mid of the season, when water table can be above, below, or at the level the surface, depending also on the micro-topography.

The density m_1 represents the length density of the interface between the black and the white phase. It increases monotonically as long as the patches stay isolated, but it decreases when they start to merge (i. e., for larger values of g_0). The maximum value

of m_1 progressively decreases as the season progresses because the pattern becomes more and more structured due to the directional flow. The quantity m_2, instead, is proportional to the Euler number of the white phase. For extreme values of g_0, we expect the pattern to consist predominately of isolated patches, namely large black patches for small values, representing isolated objects, and large white patches for large values. Thus, m_2 is expected to be positive for small values of g_0 and negative for large ones, as shown in Figure 4(c).

In order to investigate the dynamics of the water table influenced by micro-topography at a landscape-scale we have to repeat the analysis with the Minkowski densities at each time step of the simulation. This procedure can help to develop a parameterization that can bridge the spatial scale gap from the 1 m scale of the micro-topographic features to the 1 km scale of the landscape dynamics. We show the procedure in the following two sections.

4.3.4 Water table dynamics at landscape-scale

We analyze the dynamics of the different Minkowski densities over the whole season. At each time step we produce a binary image of the water table position in respect to the surface. As we described in Section 4.2.2, we discretize the surface depending on the position of the water table relatively to the surface of the grid cell. We therefore obtain thee surface classes defined as:

- Wet surface
- Saturated surface
- Dry surface

At each time step t, i. e., and for each image, and for each surface class, we compute a Minkowski densities $m_\nu(t)$, with $\nu = 0, 1, 2$. We are therefore able to compute the dynamics of the Minkowski densities. Results are shown in Figure 4.6. Panel (a) shows the dynamics of the density area $m_0(t)$ for the three surface classes. Note that if we sum up the densities for the three classes at each time step, we always obtain 1. The dynamics of the densities shows a general drastic decrease in the area covered by the *Wet* surface after the snowmelt (dashed line). This result agrees with the water table dynamics we showed in the previous Chapter, which displays an almost linear decrease over the summer season if averaged over the whole region. In particular, we see how the line approaches 0 as the simulation proceeds and no grid cell belongs to this surface

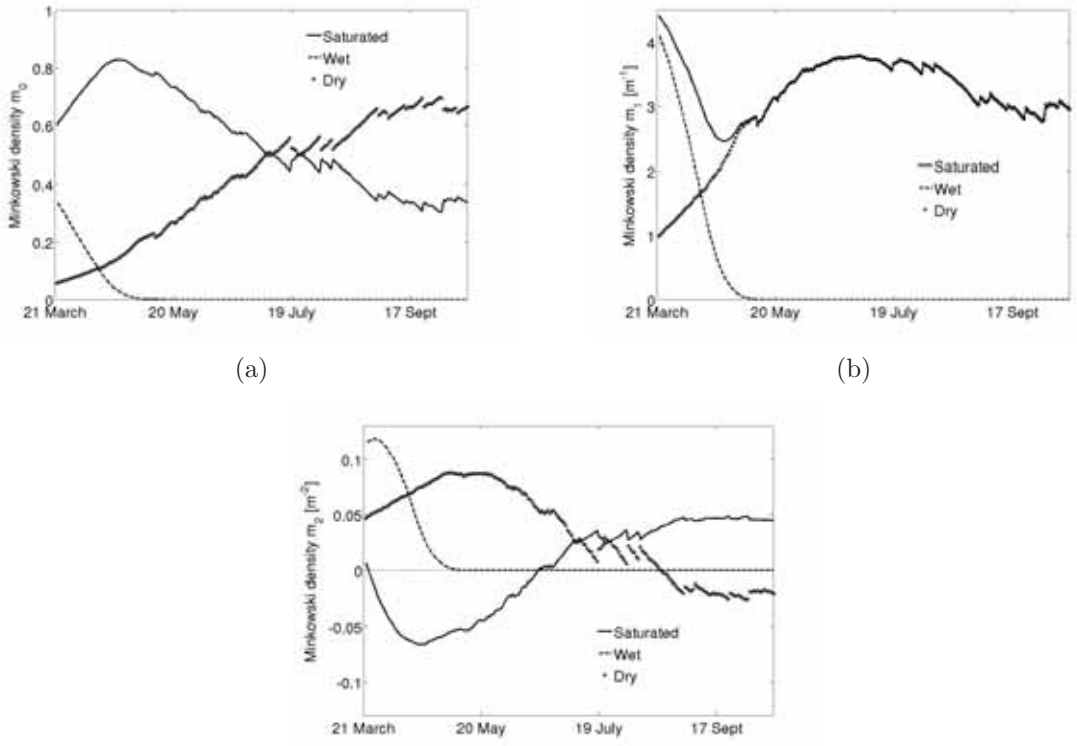

Figure 4.6: Figure shows the Minkowski densities for the white phase of the binary representation of water table pattern of a northern peatland. The different patterns are represented during the summer season, analyzing the dynamics of the water table level. We chose three different levels for surface wetness: *Wet* if water table is more than 15 cm above the surface level, *Saturated* if water table lays between -10 cm and 15 cm in respect to the surface level, and *Dry* if water table lays more than - 10 cm below the surface. Quantities $m_0(t)$, $m_1(t)$, and $m_2(t)$ are shown in panels (a), (b), and (c) respectively.

class by the end of May. This dynamics is also confirmed by the analysis of the spatial distribution of water table in Chapter 3. After snowmelt, when a large amount of water is released on the peatland, and most of the grid cells become inundated, water starts to flow out of the system. At the beginning of the season, virtually only *Wet* and *Saturated* surface classes are present, and conversely *Saturated* (solid line) and *Dry* (dotted line) classes are represented at the end of the season. Because of this general drying, more and more of formerly *Wet* grid cells, become *Saturated*. This property is reflected in the solid line dynamics in panel (a) of Figure 4.6, which grows as the dashed line decreases. The amount of *Saturated* cells increases as much as 85 % of all cells at the beginning of May, before constantly decreasing as the water table drops. At the end of the season, most of the landscape becomes relatively drier, and more than 70 % of the grid cells belong to the *Dry* surface class.

Minkowski densities, as we mentioned in the Theory section, are integral quantities, therefore they do not give any information on the local patterns, but they give only information on the pattern properties at the landscape-scale. In panel (b) of Figure 4.6, we show the dynamics of $m_1(t)$ for the three surface classes. This Minkowski density represents the perimeter of all the patches captured by the binary image. For the *Wet* class (dashed line), we see how the perimeter of the patches decreases sharply as the number of *Wet* grid cells decreases. Similarly to what happened in the analysis of surface classes in the polygonal model, after May the landscape is covered only by grid cells belonging to two surface classes, *Saturated* and *Dry*. Towards the end of the season, then, the perimeter length of these two classes is the same because they represent the white phase and the black phase of the pattern we analyze. As the water table continues to drop, the number of *Saturated* grid cells decreases (solid line). The perimeter length reaches its minimum around the same time when the area density reaches its maximum, as most of the grid cells belong to one single pattern. Symmetrically, at the end of the season, the perimeter density of *Dry* grid cells (dotted line) reaches its minimum as the m_0 for the same surface class peaks.

Dynamics of both $m_0(t)$ and $m_1(t)$ are mirrored by the Euler number $m_2(t)$, displayed in panel (c) of Figure 4.6, which in in turn gives information on connectivity of the patches belonging to a certain pattern. Negative values of this quantity mean that most of the patches are interconnected (i. e., two grid cells share a side with each other). As we expected the *Saturated* surface class (solid line) displays a high degree of connectivity at the beginning of the season, when most of the patches are *Saturated*, and therefore they have to be strongly interconnected. The Euler number changes sign (i. e., there are less interconnected patches than connected ones), when the number of patches is less than 58 %. This property emerges also by the analysis of the solid (*Saturated*), and dotted (*Dry*) lines: as the number of cell belonging to a certain surface class reaches 58 %, the corresponding Euler number $m_2(t)$ approaches 0. In partiuclar, in the case of the *Dry* surface class, the Euler number changes sign only at the end of the season, when the number of grid cells exceeds the 58 % threshold. Let us note that this number is *not* the percolation threshold for the squared lattice, which is in fact exactly 50 %. This mismatch is explained by the intrinsic nature of the Minkowski densities, which are once again integral quantities. In the percolation theory we look for an open path from one border of the domain to an other one. As the number of connected patches increases, this threshold must be smaller than the number of patches necessary for the Euler number to become negative.

4.3.5 Upscaling greenhouse gas emissions from northern peatlands

We want to use the output we obtain from the Minkowski density dynamics in order to describe the dynamics of methane emissions from northern peatlands. In particular, we want to upscale the information from the micro-topography model, relating the surface class we analyzed in the previous Sections to greenhouse gas emissions. We show here a first example of the upscaling power of the method involving Minkowski densities. We link the first density $m_0(t)$ of the *Saturated* surface class and the greenhouse gas emissions. As described in the Section 4.2.2, according to Eq. 4.12 and 4.14, we assume that by parameterizing the behavior of the highly emissive saturated area we can better capture the methane fluxes and their dynamics.

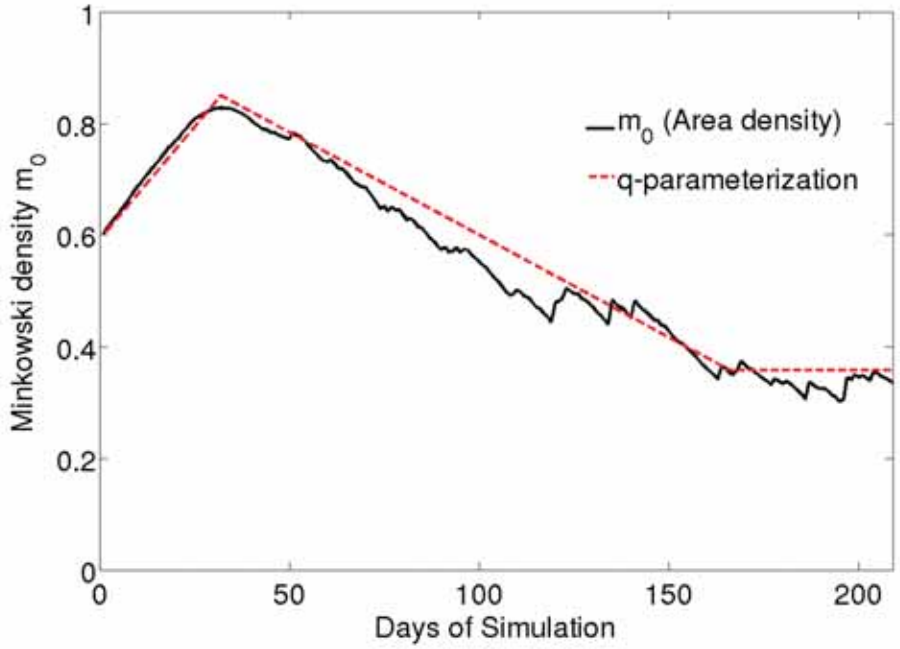

Figure 4.7: Comparison between $m_0(t)$ (black solid line) and parameterization of saturated area $q(t)$ (red dashed line). We assume the parameterization with a simple linear function to be a good enough fit to the modeled saturated grid cells dynamics in the micro-topographic model described in Chapter 3.

In order to achieve this result, we analyze the dynamics of the Minkowski density $m_0(t)$ for the *Saturated* grid cells, which gives us information on the area covered by this surface class. We parameterize the $m_0(t)$ with a simple linear function $q(t)$ which

Symbol	Meaning	Value	Units
t_0	Initial day of simulation	0	days
t_1	Day of maximum saturation	110	days
t_2	Day of minimum saturation	245	days
q_{in}	Initial saturation area density	0.6	–
q_{max}	Maximum saturation area density	0.85	–
q_{fin}	Saturation area density at the end of simulation	0.2	–

Table 4.2: Table showing parameter values for Equation 4.16. We infer the values from the dynamics of the first Minkowski density $m_0(t)$ for grid cells belonging to *Saturated* surface class. The output of the model is obtained from the micro-topographic model described in Chapter 3 at 1 m resolution.

at each time step gives the amount of *Saturated* grid cells:

$$q(t) = \begin{cases} q_{in} + \frac{q_{max}-q_{in}}{t_1-t_0}(t-t_0) & \text{if } t \leq t_1 \\ q_{max} + \frac{q_{fin}-q_{max}}{t_2-t_1}(t-t_2) & \text{if } t \geq t_1 \\ q(t-1) & \text{otherwise} \end{cases} \tag{4.16}$$

where t is the daily time step of the simulation, and the parameters t_i and q_j, with $i = 0, 1, 2$ and $j = in, max, fin$, are tuned quantities we obtain according to the dynamics of $m_0(t)$, and their values are listed in Table 4.2. Figure 4.7 shows the agreement between $q(t)$ parameterization and $m_0(t)$ dynamics of *Saturated* grid cells. Both $q(t)$ and $m_0(t)$ are area densities, therefore their values are between 0 and 1.

The amount of methane which is emitted by each kind of surface class changes according to the relative position of water table and surface. In the process-based methane emission model developed by Walter and Heimann (2000), the water table is a key variable in methane fluxes, because of the oxidation processes simulated as the water table drops below the surface and as the oxic zone deepens. The micro-topographic representation allows us to better represent the methane fluxes, because the hydrological interactions at the finer scale influence the average position of the water table. Combining the assumptions of Section 4.2.2, Equations 4.12 and 4.14, and parameterization of $q(t)$ in Equation 4.16, we obtain a new fluxes dynamics. We show the comparison among classical single bucket model, model with micro-topography representation, and the new flux with the tuned $m_0(t)$ information in Figure 4.8. The figure shows ensemble simulations of methane emissions from the different configura-

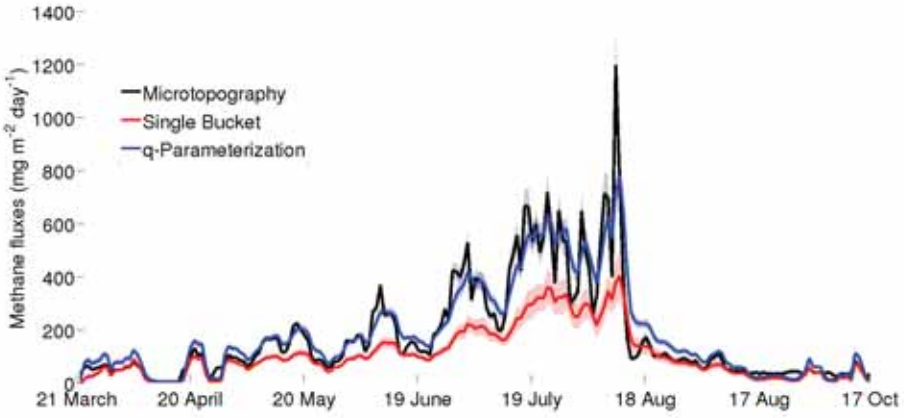

Figure 4.8: Ensemble simulations of methane dynamics and upscaled micrtopographic effects. The lines represents the simulated methane emission dynamics from the Ust-Pojeg mire complex in the Komi Republic, Russia. The red line represents emissions from a classical single bucket model, which ignores the micro-topographic representation. The black line shows emissions from the same region, but considering micro-topography at 1 m resolution. The difference in fluxes is largely dependent on the different position of the water table in respect to the surface in the two model configuration. The blue line represents methane emissions from the bucket model tuned with the upscaled information from the $m_0(t)$ dynamics of the saturated grid cells. The shaded areas are the standard deviation from the ensemble means (solid lines).

tions of the model. The solid lines represents the ensemble mean of the 30 ensemble members, and the shaded areas represent the standard deviation from the ensemble mean. The classical single bucket model (red line) underestimates the methane emissions, because of the rapid drying of the surface due to the lacking of a physically sound hydrological representation. The model with micro-topography representation at 1 m resolution (black line), instead, correctly simulates methane emissions, but it is computationally much more expensive. Using the tuning we described above, we obtain the new flux dynamics from the modified single bucked configuration (blue line), which is computationally analogous to the classical single bucket, but improves quite substantially the methane emissions if compared to the black line.

The main difference between the single bucket configuration and the one with micro-topography representation is the fact that the single bucket largely underestimates emissions in the central part of the summer season, i. e. in July and August, and we manage to improve this feature. The improvement is visually good, and it strikes to be even better if we compare the cumulative emissions of the three different configurations, as shown in Table 4.3. With the $q(t)$ parameterization of the saturated surface we effectively change the average water table level, coming closer to the output from the configuration representing the micro-topography.

Symbol	Meaning	Value	Units
CH_4^{sin}	Cumulative emissions from the classical single bucket configuration (no micro-topography)	1.7×10^4	mg m^{-2}
CH_4^{mic}	Cumulative emissions from the model with micro-topography at 1 m resolution	3.7×10^4	mg m^{-2}
CH_4^{tun}	Cumulative emissions from the single bucket configuration tuned with the $q(t)$ parameterization (no micro-topography)	3.5×10^4	mg m^{-2}

Table 4.3: The table shows the cumulative emissions from different model configurations. The single bucket produces less than the half of the cumulative methane emissions in respect to the model with micro-topography representation. By inserting a simple parameterization of the saturated surface dynamics, we improve significantly the seasonal methane emissions. The values are averages over 30 ensemble members in each configuration.

The parameterization of $q(t)$ is therefore fundamental in forecasting cumulative emissions, and the linear function we inferred from the $m_0(t)$ is dependent on the particular climatic conditions we simulated, which are described in details in Chapter 3. In order to obtain a working procedure that can be inserted in a larger scale model such as a DGVM, we would need to explore different climate regimes, and different surface properties. Such a forcing and parameter exploration of the model described in Chapter 3 could potentially produce an array of parameterization functions $q_i(t)$, with i depending on climatic conditions and terrain properties. Such procedure could lead to a global upscaling of micro-topography in different peatlands.

4.4 Summary and conclusions

We presented Minkowski functionals and densities as a useful instrument to analyze and quantify pattern dynamics at a landscape-scale. Patterns emerging from local interactions can influence larger scale properties of the ecosystems, which in turn influence land-atmosphere interactions. In particular, greenhouse gas emissions depend on heterogeneous landscape properties, and only local mechanistic or statistical models can correctly represent the small-scale behavior of local properties as we showed in

Chapter 3 and 2 respectively. By the means of the Minkowski densities we can analyze and compare pattern properties emerging from the model output, obtaining information at the landscape-scale, due to the integral nature of the densities. We used the spatially explicit outputs from the models we presented in the previous Chapters to understand landscape-scale properties of the emergent patterns.

We initially applied the analysis to the stochastic model for the polygonal tundra, which is based on the structure of the Poisson-Voronoi Diagrams. We discretized the surface of the polygonal centers in three classes, depending on the relative position of the water table in respect to the surface. Translating the outputs in black and white images we are able to distinguish the different dynamics of surfaces with different moisture characteristics. Most of the polygons display a water table either approximatively at the surface level, or above the surface, which seems to be the dominating pattern under standard levels of precipitation. If we increase precipitation input further, the landscape becomes tessellated mostly by small ponds, and the patches constituting the pattern rapidly become interconnected. Such a phenomenon, due to the very coarse and simplistic representation of both thaw depth dynamics and hydrology, does not aim to explain or represent realistic or actual phenomena, but it might be an interesting starting point for further investigations.

In the latter sections, we applied the Minkowski densities to the model for peatland micro-topography we developed and showed in Chapter 3. In this case, we described more explicitly the hydrology and the micro-scale properties of the system, coupling it with the process-based model for methane emissions developed by Walter and Heimann (2000). We analyzed the pattern response visualized in greyscale images at different levels of segmentation threshold, applying this procedure at three different representative time steps. We showed the dependence on the analyzed pattern on such threshold g_0, and we showed how it changes in the three snapshots we chose. In order to better understand the information, we needed to repeat the the procedure developed for the analysis of the permafrost patterns, discretizing the surface in three classes based on the position of the water table in respect to the surface. By doing so, we were able to capture the dynamical characteristics of surface classes with different wetness and different emitting properties. In Chapter 3 we showed how the position of the water table affects and regulates the emissions, and how the water table position depends on the micro-topography. Therefore we developed a novel simple parameterization in order to take into account these effects in the single-bucket model. We showed how such a simple parameterization of the area covered by the highly emissive saturated grid cells could significantly improve not only the overall cumulative amount of emissions from the landscape, but also the dynamics of the pattern.

In the examples we showed, we made mainly use of the information of the m_0 density, namely the area density. This is because the particular problem of greenhouse gas emissions from northern peatlands can be tackled, as we showed in Section 4.3.3, only by considering the dynamics of the area covered by a particular surface class. The dynamics of m_1 and m_2 are useful to quantify some of the pattern properties, which we can indeed describe better by considering also these quantities. Such information, though, is neglectable in the direct computation of fluxes. We nevertheless argue that other research questions could be investigated and successfully tackled by further applications of all the densities to pattern analysis. In particular, we think at the problem of surface heterogeneity triggering convection. Moreover, in order to grasp the full potential of the Minkowski numbers one would need to tackle the problem not on a landscape-scale level through integral quantities, but one would need tools which could resolve also local pattern variations. Therefore, one would need to expand the concepts of Minkowski functionals and densities to Minkowski *functions* (Vogel et al., 2010), as we extensively show in Appendix B. Such tools can not only provide properties like the size distributions of the patches, but they can also theoretically provide the variance of the average properties we analyze with the Minkowski densities. As for the applications to the polygonal model, it could also be possible to link the connectivity of the patches with the bond percolation threshold. A further analysis involving Minkowski functions would directly provide a link between the two methods. It would be necessary to use field data to tune and adapt the model to better describe the water flow in the ice channels. This phenomenon of multichannel flow and interconnectivity has been observed in recent studies (i. e., Fortier et al., 2007; Boike et al., 2008) and it has been suggested a connection between landscape-scale channel interconnectivity and thermokarst lake formation due to channel degradation because of thermal erosion (A. Liljedahl and G. Grosse, personal communication). As for the applications to the peatland model, recent works (i. e., Morris et al., 2013; Larsen et al., 2012) highlighted how directional connectivity could provide information on landscape-scale properties, such as environmental degradation and peatland development. These phenomena are worthy to be investigated with applications of m_2 to photographs and possibly to expansions of the micro-topographic model.

The parameterization of the $q(t)$ dynamics (equation 4.16 and table 4.2), at almost no computational cost qualitatively changes the system response for methane emissions. This is just an example, but it is a first significant step towards a full parameterization of the micro-topographic impacts on such complex systems at the DGVM-scale. In order to fulfill such a task, though, we would need a comprehensive and statistical analysis on the response of the mechanistic local-scale model to climatic forcing, such

as change in precipitation, net primary productivity (NPP), or temperature. Such a study would be able to construct a consistent array for the parameterization of saturated area dynamics, ultimately leading to a climate-dependent parameterization, feasible to be introduced in a DGVM such as JSBACH.

Introducing the analysis of spatial patterns produced by different mechanistic models in multiple ecosystems can be a powerful method to infer landscape-scale dynamics a characteristics of patterns. It can potentially be applied to outputs of models investigating vegetation patterns in water limited ecosystems, in peatlands and in Periarctic environments, and also to models describyng spatial gaps in forests.

This procedure could be repeated using other mechanistic models working in different ecosystems, possibly filling the scale gaps in climate-biosphere interactions identified by Rietkerk et al. (2011).

Chapter 5

Summary and Conclusions

5.1 Synthesis and answers to the research questions

In Chapter 1, I outlined the main research questions I tackled in the present thesis. In Chapter 2, I focused my modeling efforts of sub-grid scale heterogeneities on the polygonal tundra. In Chapter 3, I generalized my multi-scale investigation to a typical boreal peatland, before applying the Minkowski density analysis in Chapter 4, in order to identify emerging pattern properties of the two models I developed. I now proceed to summarize the answers to the research questions. More complete and detailed answers can be found in the main Chapters. I will first answer to the last, more specific questions formulated in Chapter 1, before tackling the overarching research question.

How can we represent multi-scale phenomena in permafrost environments, such as the polygonal tundra, from the single polygons to the landscape-scale?
By tessellating the surface with Poisson-Voronoi diagrams, I was able to represent with stochastic polygons the small-scale heterogeneities in the low center polygonal tundra. The terrain geometrical characteristics are statistically consistent with data from an aerial image of the polygonal tundra in the Lena river Delta, Russia.

Modeled water table variations in single polygons include both large-scale climate forcing, such as precipitation P, and small-scale phenomena, such as evapotranspiration ET and lateral runoff R. The stochastic representation is fundamental to parameterize the phenomena at different scales and to correctly compute the area covered by surfaces with different wetness, even though it is far from the precision and the accuracy of a mechanistic model.

I demonstrated that a stochastic parameterization, such as the one involving a subdivision of space through Poisson-Voronoi diagrams, is a powerful tool to upscale

small-scale surface heterogeneities. Such a parameterization can represent the ecosystem across different scales, from the single polygons (10^0 - 10^1 m) to the landscape-scale (10^3 m).

How and to which extent do sub-grid scale surface heterogeneities control the water balance in the polygonal tundra?
The sub-grid scale surface heterogeneities, even in the simple parameterization I presented, appear to be fundamental in the representation of water table dynamics, particularly towards the end of the season. When the water table lays above the thaw depth level in single polygons, lateral runoff is triggered and water table drops. By taking into account the surface heterogeneities, the water balance changes from the simple average $P - ET$ to $P - ET - R$. The modeled dynamics is consistent with observations. Such a difference between the simple $P - ET$ balance and the water table dynamics with local runoff becomes even more pronounced under extreme climatic regimes, i .e., if precipitation is doubled or halved.

What are the effects of micro-topography on water, carbon, and energy balance in a typical boreal peatland?
I compared the simulations performed with an accurate representation of the micro-topography with a single bucked model for boreal peatlands to assess the effects of small-scale features on water, carbon, and energy balance of the ecosystem.

In the single bucket version of the model, all features are averaged over the peatland dimensions. In the version with micro-topographic representation, instead, the model runs at a 1 m resolution, resolving the micro-topographic relieves that characterize the surface of the peatlands, i. e., hummocks and hollows. The small-scale micro-topography directly affects the system hydrology and the water table dynamics. After the snowmelt, a large amount of water flows in the system and most of the landscape becomes inundated. As the simulation proceeds, in the single bucket case the water flows quickly out of the system, and the water table drops below the surface level. In the model version with micro-topography representation, instead, complex small-scale hydrological interactions influence water table position as the outflow is delayed, in agreement with observations. Other effects, such as heterogeneous albedo and heterogeneous drainable porosity, do not affect the model behavior qualitatively.

Water table affects in turn both carbon and energy balance of the system, as it changes the amount of greenhouse gas emissions and the heat capacity of the surface. Hydrology changes the depth of the oxic zone in peat soil, influencing the amount of methane which can be oxidated and then emitted as carbon dioxide. I show how neglecting small-scale interactions may lead to an underestimation of cumulative emis-

sions over the warm season by a factor of two.

Water table dynamics also influences the energy balance of the surface, as water and peat have different heat capacities. The water table lasts longer above the surface in the model version with micro-topographic representation and it affects the soil temperature allowing an increase in temperature only after the water table drops below the soil surface.

Some kind of micro-topographic representation is needed to correctly grasp not only the magnitude, but also the dynamics of water, carbon, and energy balance.

How can we identify the landscape-scale properties of the patterns emerging from sub-grid scale features in boreal ecosystem?
Minkowski densities are useful tools to quantify patterns emerging from the small-scale interactions. I used such geometric functionals in the analysis framework I developed in order to infer characteristics of the spatial structures of the landscape-scale patterns in the two models I presented in Chapters 2 and 3. Minkowski densities are integral quantities, which give information only on the overall behavior of the pattern. By analyzing images generated by model output, I was also able to identify the dynamics of the pattern properties over the season.

Applications of Minkowski densities to the model for low center polygonal tundra reveal that the saturated polygons are the dominant pattern in the landscape. With water table dropping, transitions of small ponds into saturated polygons become more frequent. If the precipitation increases, the dominant pattern of the landscape becomes the one constituted by small ponds, as the water table increases accordingly. Therefore, the transition described above changes sign, i. e., saturated centers become small ponds. The drainage network of the system is not sufficient to outflow the water and polygons with small ponds become a highly interconnected pattern.

I then applied the Minkowski density analysis to the spatially explicit output of water table elevation relative to the surface from the peatland micro-topographic version of the model. By discretizing the surface in three different classes, depending on the relative wetness, I was able to identify the seasonal behavior of wet, dry, and saturated surface classes in a typical boreal peatland and to identify the properties of the emerging pattern.

How can we develop an effective theory, feasible to be incorporated in a DGVM, which takes into account the information arising from such small-scale features?
I used the general framework of effective theory development in order to parameterize

important variables in greenhouse gas emissions for northern peatlands. I identified the hydrology as the main physical process affected by presence or absence of micro-topography, and I developed a novel simple parameterization, representing the micro-topographic effect on water table.

As the saturated patches are hotspots for methane emissions, I modified the parameterization for water table dynamics in a classical bucket model, using the information from the pattern dynamics of saturated grid cells. Such parameterization, although computationally analogous to the bucket model dynamics, reproduces the seasonal behavior of water table similarly to the computationally expensive model with explicit micro-topographic representation. Methane emissions are comparable, demonstrating that also nonlinear processes, such as carbon emission dynamics, can be captured by a simple linear parameterization, such as the one that I described in the present thesis.

Parameterizations of water table dynamics can be inferred by taking into account the information emerging from small-scale interactions. Process-based or stochastic models, working at the landscape-scale (10^3 - 10^4 m), can be used in order to develop such computationally feasible parameterizations, which can in turn be included in DGVMs soil modules.

After the specific investigations conducted in the main Chapters, I can finally tackle the overarching research question:
How do sub-grid scale surface heterogeneities influence climate-biogeosphere interactions in high-latitude ecosystems?
Hydrology is one of the main ecosystem controls in high-latitude ecosystems. In peatlands, it controls the form in which greenhouse gases are emitted (i. e., carbon dioxide or methane). Sub-grid scale surface heterogeneities, from permafrost-generated polygons to self-organized vegetation patterns, can directly influence the hydrological properties of the system by adding variability to soil surface parameters, i .e., hydraulic conductivity, albedo, drainable porosity, etc. The small-scale interactions at spatial scales of typical length $\leq 10^0$ m deeply affect not only the small-scale hydrological response to external forcing (such as precipitation, snowfall, etc.), but also ecosystem-scale runoff and other quantities with a typical scale of $\approx 10^3$ m.

By affecting the hydrology, the sub-grid scale surface heterogeneities have also a secondary effect on the land-atmosphere fluxes of water, carbon, and energy. As I explained in details in Chapters 3 and 4, changes in water table depth affect the methane flux dynamics. It is possible to capture the magnitude and the dynamics of greenhouse gas emissions only by taking into account the small-scale topography of soil surface either explicitly (with a process-based model), or with a parameterization

that effectively describes the emergent behavior of the system. Methane emissions, for example, respond in a highly nonlinear way in respect to water table position, and small changes in water table depth may lead to large variations in flux responses. Drier and wetter surfaces, heterogeneously distributed over the landscape (or over the DGVM grid cell), regulate latent to sensible heat flux ratio and affect both soil and air temperature. This phenomenon is particularly pronounced after the snowmelt in boreal peatlands, where a large amount of water flows into the system, regulating the whole warm season hydrology. The spring water flow dominates the hydrological properties in the ecosystem and it influences directly the energy balance, depending on how long the surface ponding lasts and how fast the water flows out of the system.

These parameters vary at scales much finer than the typical scale of an atmospheric model (typically > 30 km). I showed in this thesis how the lack of any representation of sub-grid scale heterogeneities in global model may lead to misrepresentation not only of hydrological features, but also of land-atmosphere water and carbon fluxes.

5.2 Outlook to future research

The present thesis constitutes a first step towards an analysis of the interactions across multiple scales between land, biosphere, and climate in boreal ecosystems. Further developments are possible in different directions, from local model development, to expansions of the developed techniques, to the integration of this work to global models. I will briefly outline the limitations of this study before highlighting the possible implications of the present study for the formulation and the answer to further research questions.

5.2.1 Limitations of the study

The models I presented in this thesis have some limitations that have to be highlighted. For example, I needed to formulate some necessary assumptions for the models to work at the small scales of surface heterogeneities, which I will now briefly describe.

In the case of the stochastic model for polygonal tundra, many process are prescribed. Precipitation, evapotranspiration, thaw depth dynamics, and runoff are simply parameterized. These assumptions are useful for the model purposes in this study, but they hinder the predictive power of the model, since results may depend on such prescribed dynamics. In order to increase the range of applications of the model, i. e. to apply the model to other environments, a more physically-based approach is needed.

The stochastic tessellation is tuned on the Lena river Delta site I analyzed. In order to represent other sites, the tessellation has to be recalibrated. The model represents a snapshot of present day low center polygonal tundra, and it does not consider polygon formation and degradation. I also do not simulate snowfall and snowmelt, hence the maximum number of days of simulations must be limited at t_{max} =90, in order to exclude the period of time when the snowmelt dominates the landscape hydrology.

The model for peatland micro-topography is instead finely tuned with elevation data for hummocks and hollows collected in the Ust-Pojeg mire complex in Komi Republic, Russia. Therefore, the quantitative results on methane emissions and energy balance are limited on the specific site, I analyzed in Chapter 3. The qualitative difference between model versions with and without micro-topographic representation, instead, is robust and not site-specific. The process-based model for methane emissions only outputs methane emissions, but it can be interesting to investigate also carbon dioxide emissions, in order to complete the carbon balance of the environment. Another possible limitation is the absence of vegetation dynamics. Even though the modeling of these processes goes beyond the scope of this study, these features can also have an influence on greenhouse gas dynamics.

Both models are not feasible to be included in DGVMs. Even the faster, stochastic approach has a large number of parameters representing small-scale processes. In order to implement the effects of sub-grid scale heterogeneities, one needs another, simpler and computationally more feasible parameterization.

The models, even if tuned for specific environments, propose novel methods, which are general enough to be applied to different ecosystems. The Poisson-Voronoi tessellation, in particular, as a stochastic subdivision of space is a powerful technique to tackle small-scale problems, from spatially explicit thermokarst lake modeling to forest management. Further possible applications of the models will be discussed in the next Sections.

5.2.2 Stochastic models for scale interactions in permafrost landscapes

The model I presented in Chapter 2 proposes a novel method to tackle the representation of small-scale features in permafrost ecosystems. One possible development of the model is the description and characterization of other landscapes displaying analogous low-center polygonal patterned grounds, such as Barrow, Alaska (described, i. e., in Lachenbruch, 1972). Different sites with similar ecosystems, located in different parts

of the Arctic, may display different properties at the landscape-scale, and such changes can be identified by analyzing the networks representing the different sites. One can repeat the analysis performed in Chapter 2 by fitting the Poisson-Voronoi area distribution to the ice-wedge polygon area distribution. It could be possible to compare the new findings with the results I showed in this thesis for Samoylov Island in the Lena Delta, Russia. Such a comparison can provide information on the landscape-scale differences between the different sites that local measurements would not be able to grasp. Other developments involve inserting more physical processes in the stochastic model. Thaw depth development, for example, is simply prescribed in the model I presented. In order to get more quantative information and to increase the predictive power of the model, a better parameterization of this process is needed.

Recent studies, such as Liljedahl et al. (2012), showed how the snowmelt dominates the water flow input in permafrost regions, and therefore it is a process one needs to include in the model in order to extend the timespan of simulations. Other processes yet not included could improve model physics and model response to climatic forcing. Examples of them are hydrological properties of the system and a better characterization of the channel network. Potentially, such an improved model will be able to describe the response of the drainage network on precipitation or on temperature variations. A further step would be the physical modeling of thermo-erosion of the interpolygonal channels due to water flow, or a stochastic parameterization of this phenomenon. Thermokarst development of small lakes can be initiated by progressive degradation of polygonal rims, due to thermo-erosion. The erosion of interpolygonal channels could trigger possible changes of environmental properties, such as large-scale transitions. The transformation of the low-center polygonal landscape to a high-center polygonal tundra system, and finally to a thermokarst lake, has not yet been investigated with models. However, it is a dominant process that shapes the Arctic environment that has been at work since the last glacial. New modeling efforts are necessary to better understand such a long term process.

Another direction of model expansion and generalization is the application of the stochastic tessellation as a subdivision space at larger scales, in order to model water body area distribution using datasets as the one developed by Muster et al. (2013). One can potentially assign stochastic differential equations to each Voronoi polygon to model transitions from permafrost-dominated landscape to thermokarst lake. Combining this technique with a physically-based model for thermokarst lake expansion over time can be a further potential development to tackle major uncertainties in permafrost environments.

5.2.3 Applications of the peatland micro-topographic model

I developed the model for surface micro-topography in boreal peatlands tuning it with data from the Ust-Pojeg mire complex, in Russia. It is an interesting question how the model works if tuned with other elevation data from different peatlands, but in order to perform such a task more fine-scale elevation data from other peatlands are needed, and extensive field campaigns are necessary to provide them. By focusing on the same peatland, it can be interesting to explore other properties, which are still beyond the scope of this thesis. It is an interesting possible development the expansion of the model through the implementation of information on the nutrient flow inside the system. One could potentially make use of measurements collected by the Institute of Soil Science of the Hamburg University in order to identify the possible effects of micro-topography on nutrient and carbon flow in the peatland.

It is also possible to force the model with other data from CMIP5 experiments, in order to investigate the importance of temperature and NPP changes on methane emissions. Coupling the model with a carbon accumulation model can also help investigating the potential effects of micro-topography on long term peatland evolution as carbon source and sink.

5.2.4 Spatial pattern analysis in different ecosystems

Another implication of the present thesis for possible future research is the use of the Minkowski analysis techniques on other spatial patterns, expanding the range of applications to other environments at lower latitudes. Quantifications of spatial pattern properties, such as interconnectivity and size distribution of the patches can give further insights to ecosystem properties. I applied the analysis to the relative position of water table in respect to the surface, as influenced by surface heterogeneities in peatlands.

An interesting development is the analysis of the spatial output of other models, such as the ones developed by von Hardenberg et al. (2001); HilleRisLambers et al. (2001), or modifications of them. This analysis can be performed not only by the means of Minkowski functionals and densities, but also with the application of Minkowski functions in order to identify not integral properties, as outlined in Appendix B.

It would be theoretically possible also to look for a dynamics in the pattern properties, in order to find out which characteristics change if the system catastrophically collapses. Patch-size distribution have been identified as a warning signal for desertification onset in water-limited ecosystems, as highlighted by Kéfi et al. (2007). Critical

slowing down has been suggested to be a key phenomenon to quantify distance from bifurcations and catastrophic shifts in ecosystems (Scheffer et al., 2009; Dakos et al., 2008), but recent studies pointed out some limitations of such powerful method (Kéfi et al., 2013; Dakos et al., 2011). Exploring the behavior of interconnectivity of patches and other properties, from size to perimeter length in the proximity of a catastrophic shift may give some more insights in the complex issue of critical transitions in ecosystems.

5.2.5 Global and regional scale impacts of sub-grid heterogeneities

A complete and consistent parameterization of sub-grid heterogeneity effects on hydrological features, which I identified as one of the key controls on land-atmosphere fluxes in high-latitude ecosystems, is still missing. I proposed in Chapter 4 a novel parameterization which takes into account cross-scale information, but I only showed and analyzed the functioning of such method under one realization of climatic forcing.

In order to explore the full array of feedbacks emerging from small-scale interactions, it is necessary to force the model with different input data, using possible forcing scenarios with different ranges of climatic forcing. For example, one could potentially vary levels of precipitation, snowfall, and temperature. The values of the linear parameterization I developed and showed in Chapter 4, will change depending on the forcing. Such a sensitivity study could potentially produce a parameterization with climate-dependent parameters can be finally inserted in a global modeling framework, allowing a possible evaluation of large-scale effects and feedbacks originating from small-scale features on regional, or even global climate.

Theoretically, similar parameterizations could be developed for other surface heterogeneities in other environments, in the theoretical framework highlighted by Rietkerk et al. (2011). The upscaling of different features, from land-atmosphere water exchanges in drylands, as shown by Baudena et al. (2013), to scale-dependent land-atmosphere carbon fluxes, as shown by Baird et al. (2009a), could then be feasibly implemented in global parameterizations, which would consistently take into account interactions across multiple scales in the climate-biogeosphere system.

Appendix A

Computation of the Minkowski densities

In order to compute Minkowski functionals and densities we modify and use a MATLAB algorithm developed by Paul Overduin (2009), which in turns translates the original C++ code developed by H. J. Vogel, available in the QuantIm library for image processing at the website www.ufz.de.

We give the algorithm a black and white image as input, where pixels can have a binary value (0 or 1) in respect to the background. The computation of the Minkowski densities derives from the analysis of a 2×2 neighborhood for each point. There are $n = 2^4 = 16$ possible configurations c, if each edge (pixel, in the case of our images) of the square identified by the neighborhood can assume 2 values. In Figure A.1 we show an example of the 2×2 neighborhood and of the 16 possible configurations c. Each configuration c contributes differently to the values of the Minkowski functionals as described in Table A.1, i. e., each configuration contributes differently. The contribution to M_0 is related to the number of vertices (pixels) in the neighborhood which belong to the object. In Figure A.1, we represent the contribution to M_0 with the left top vertex. If the left top vertex is full, it belongs to the object we want to analyze and its contribution is 1, otherwise its contribution is 0. The number of transitions $1 \leftrightarrow 0$ within the object boundary is instead related to M_1. We take into account the transitions over the edges incident in the vetex, and the . For the calculation of $M_2 = 2\pi\chi$ we use the Euler formula:

$$\chi = N_v - N_e + N_f \tag{A.1}$$

where N_v is the number of vertices, N_e the number of edges, and N_f the number of faces belonging to the object. We call each contribution $I_\nu(c)$, where $\nu = 0, 1, 2$ The Minkowski dentisites can be computed using the frequency of occurrence of each

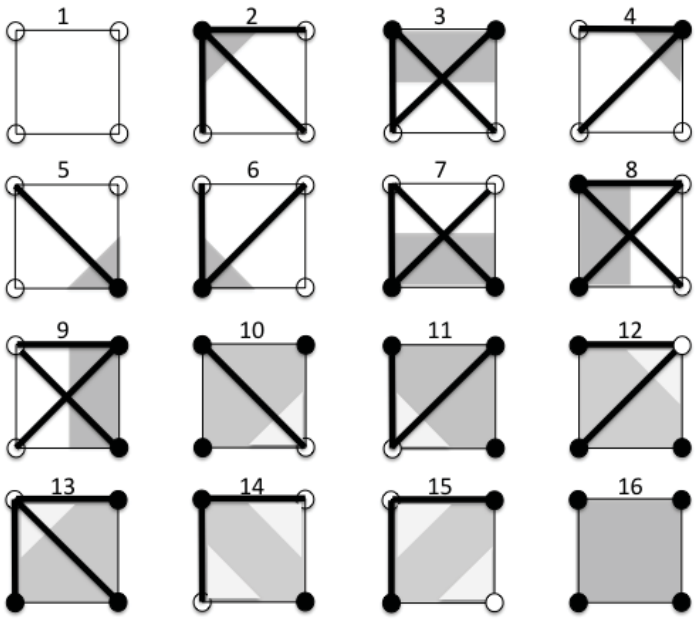

Figure A.1: The figure shows the 16 configurations c for the 2×2 neighborhood. For the computation of the Minkowski functionals in this example we consider the circle (pixel) on the *top left* of the squares. The contributions to the Minkowski functionals are described in detail in Table A.1. The shaded area represents the relative position of the object X we want to analyze and the pixel we consider. The contribution to M_0 is either 0 or 1 if the pixel is respectively full or empty. The contribution to M_1 is the number of thick lines, which show the transition from full to empty pixels and vice versa, evaluating only the edges of the square incident to the circle (pixel) at the top left corner and the square diagonals. The contribution to M_2 is computed according to equation A.1.

configuration inside the image we analyze, following:

$$f(c) = \frac{N(c)}{\sum_{c=1}^{16} N(c)} \tag{A.2}$$

where we indicate with $N(c)$ the number of of 2×2 neighborhood displaying the configuration c. We compute the Minkowski densites as:

$$m_\nu = \omega_n u \sum_{c=1}^{16} I_\nu(c) f(c) \tag{A.3}$$

where again $\nu = 0, 1, 2$, and

$$\omega_0 = \frac{1}{\sum_{c=1}^{16} f(c)} \tag{A.4}$$

$$\omega_1 = \frac{1}{3\pi} \frac{1}{(\lambda + \sqrt{2}\lambda) \sum_{c=1}^{16} f(c)} \tag{A.5}$$

$$\omega_2 = \frac{2\pi}{\lambda^2 \sum_{c=1}^{16} f(c)} \tag{A.6}$$

where λ is the side length of 1 pixel. The weights ω_ν are correct only if pixels are squares, otherwise they need to be adapted to other shapes.

M_ν	1	2	3	4	5	6	7	8	9	10	11	12	13	14	15	16
M_0	0	1	1	0	0	0	0	1	0	1	1	1	0	1	0	1
M_1	0	3	3	2	1	2	3	3	3	1	2	2	3	2	2	0
M_2	0	+1	0	0	0	0	0	0	0	-1	0	0	0	+1	0	0

Table A.1: The table shows the contributions $I_\nu(c)$ of the Minkowski functionals M_ν, where again $\nu = 0, 1, 2$, for the configurations c shown in Figure A.1.

Appendix B

Mathematical morphology and Minkowski Functions

In order to identify some local effects of patterns emerging from micro-scale interactions, information describing average quantities is not enough. This is particularly true in the case of land-atmosphere interactions, where phenomena such as convection are often triggered by spatial variance of surface heterogeneities, (as shown in, e. g., Avissar and Liu, 1996; Garcia-Carreras et al., 2010). Minkowski functionals are integral measures of the pattern, and therefore they only provide information on mean quantities, i. e., in 2D size, perimeter and mean connectivity. Other statistical properties of the pattern, such as size distribution of the patches or local connectivity, must be investigated through a different method, and therefore we introduce the use of Minkowski functions (Vogel et al., 2005). Minkowski densities can be computed as a function of a morphological transformation. Mecke (2000), introduced the Minkowski functions as based on a transformation used in mathematical morphology, morphological erosion and dilation (Serra, 1982). Mathmatical morphology is an approach for analysis of geometrical properties based on set theory, and it constitutes the basis for image transformation.

Morphological erosion/dilation is a technique that consists in probing a binary image with a shape, computing how the probe modifies the binary structure by fitting or missing the original image. The probe must be also a binary image, and it is called *structuring element*. Let us assume E to be an Euclidean space in $\mathbb{R}^2$. A is a binary image of E, and B is the structuring element. The erosion process is then described by:

$$A \ominus B = \{z \in E | B(r) \subseteq A\} \tag{B.1}$$

where $B(r)$ is the translation of B by the vector r:

$$B(r) = \{b + r | b \in B\}, \forall r \in E. \tag{B.2}$$

We can think at the resulting object of an erosion process $X_e(r)$ of A from the structuring element $B(r)$ (in this case, a disk of radius r), as the locus reached by $B(r)$ moving in A. In other words, $X_e(r)$ is the set of points z where the circular structuring element $B(r)$, moving in A, is still a complete subset of A:

$$X_e(r) = \{z : B(r) \subset A\} \tag{B.3}$$

The eroded object is then smaller than the original object, and its area depends on the radius r of the structuring element $B(r)$. The definition of dilation is analogous:

$$A \oplus B = \{z \in E | (B(r)^s) \cap A \neq \varnothing\} \tag{B.4}$$

where $B(r)^s$ is the symmetric of $B(r)$. The resulting object of a dilation process $X_d(r)$ of A from the structuring element $B(r)$ is defined as:

$$X_d(r) = \{z : B(r) \cup A \neq \varnothing\} \tag{B.5}$$

One can variate the size of the structuring element $B(r)$ and apply the Minkowski density analysis at different values of r (namely, at different pixel size): $m_\nu(r)$, $\nu = 0, 1, 2,$. This analysis is referred to as Minkowski functions with respect to r, following Vogel et al. (2010). Such an analysis provides not only averaged quantities, but also information on the local structure of the pattern. The area density function $m_0(r)$ gives information on the size distribution of the patches in the original pattern, while the length density $m_1(r)$ reflects both size distribution and the connectivity among the patterns. The number $m_2(r)$ which, as we have seen, is the Euler number, gives information the connectivity of the patches. Combinations of the functions can therefore describe local properties with local information, improving the integral description of the pattern we obtained with Minkowski densities.

List of Figures

List of Tables

Bibliography

Avissar, R. and Liu, Y. (1996). Three-dimensional numerical study of shallow convective clouds and precipitation induced by land surface forcing. *Journal of Geophysical Research: Atmospheres*, 101(D3):7499–7518.

Baird, A. J., Belyea, L. R., and Morris, P. J. (2009a). *Carbon Cycling in Northern Peatlands*, volume 184 of *Geophysical Monograph Series*. American Geophysical Union, Washington, D. C.

Baird, A. J., Belyea, L. R., and Morris, P. J. (2009b). Upscaling of Peatland-Atmosphere Fluxes of Methane: Small-Scale Heterogeneity in Process Rates and the Pitfalls of the "Bucket-and-Slab" Models. In Baird, A. J., Belyea, L. R., Comas, X., Reeve, A. S., and Slater, L. D., editors, *Carbon Cycling in Northern Peatlands*, volume 184, pages 37–53. American Geophysical Union.

Baird, A. J., Morris, P. J., and Belyea, L. R. (2012). The digibog peatland development model 1: rationale, conceptual model, and hydrological basis. *Ecohydrology*, 5(3):242–255.

Baudena, M., D'Andrea, F., and Provenzale, A. (2008). A model for soil-vegetation-atmosphere interactions in water-limited ecosystems. *Water Resources Research*, 44(12):1–9.

Baudena, M., von Hardenberg, J., and Provenzale, A. (2013). Vegetation patterns and soilatmosphere water fluxes in drylands. *Advances in Water Resources*, 53:131–138.

Becker, A. and Ziff, R. (2009). Percolation thresholds on two-dimensional Voronoi networks and Delaunay triangulations. *Physical Review E*, 80(4):1–9.

Bellisario, L. M., Bubier, J. L., Moore, T. R., and Chanton, J. P. (1999). Controls on ch4 emissions from a northern peatland. *Global Biogeochemical Cycles*, 13(1):81–91.

Blodau, C. (2002). Carbon cycling in peatlands A review of processes and controls. *Environmental Reviews*, 10:111–134.

Bohn, T. J., Podest, E., Schroeder, R., Pinto, N., McDonald, K. C., Glagolev, M., Filippov, I., Maksyutov, S., Heimann, M., Chen, X., and Lettenmaier, D. P. (2013). Modeling the large-scale effects of surface moisture heterogeneity on wetland carbon fluxes in the west siberian lowland. *Biogeosciences*, 10(10):6559–6576.

Boike, J., Wille, C., and Abnizova, A. (2008). Climatology and summer energy and water balance of polygonal tundra in the Lena River Delta , Siberia. *Journal of Geophysical Research*, 113:1–15.

Bousquet, P., Ciais, P., Miller, J., Dlugokencky, E., Hauglustaine, D., Prigent, C., Van der Werf, G., Peylin, P., Brunke, E.-G., Carouge, C., et al. (2006). Contribution of anthropogenic and natural sources to atmospheric methane variability. *Nature*, 443(7110):439–443.

Broadbent, S. and Hammersley, J. (1957). Percolation processes. In *Mathematical Proceedings of the Cambridge Philosophical Society*, volume 53, pages 629–641. Cambridge Univ Press.

Camill, P. and Clark, J. S. (1998). Climate change disequilibrium of boreal permafrost peatlands caused by local processes. *The American Naturalist*, 151(3):pp. 207–222.

Christensen, T. (1995). Response of methane emission from Arctic tundra to climatic change: results from a model simulation. *Tellus B*, 47(3):301–309.

Christensen, T. R., Ekberg, A., Strm, L., Mastepanov, M., Panikov, N., quist, M., Svensson, B. H., Nyknen, H., Martikainen, P. J., and Oskarsson, H. (2003). Factors controlling large scale variations in methane emissions from wetlands. *Geophysical Research Letters*, 30(7).

Couwenberg, J. and Fritz, C. (2012). Towards developing IPCC methane 'emission factors' for peatlands (organic soils). *Mires and Peat*, 10:1–17.

Couwenberg, J. and Joosten, H. (2005). Self-organization in raised bog patterning: the origin of microtope zonation and mesotope diversity. *Journal of Ecology*, 93(6):1238–1248.

Cresto Aleina, F., Baudena, M., D'Andrea, F., and Provenzale, A. (2013a). Multiple equilibria on planet Dune: climate vegetation dynamics on a sandy planet. *Tellus B*, 65:1–12.

Cresto Aleina, F., Brovkin, V., Muster, S., Boike, J., Kutzbach, L., Sachs, T., and Zuyev, S. (2013b). A stochastic model for the polygonal tundra based on Poisson-Voronoi diagrams. *Earth System Dynamics*, 4(October):187–198.

Dakos, V., Kfi, S., Rietkerk, M., Nes, E. H. v., and Scheffer, M. (2011). Slowing down in spatially patterned ecosystems at the brink of collapse. *The American Naturalist*, 177(6):pp. E153–E166.

Dakos, V., Scheffer, M., van Nes, E. H., Brovkin, V., Petoukhov, V., and Held, H. (2008). Slowing down as an early warning signal for abrupt climate change. *Proceedings of the National Academy of Sciences*, 105(38):14308–14312.

D'Andrea, F., Provenzale, A., Vautard, R., and De Noblet-Decoudré, N. (2006). Hot and cool summers: Multiple equilibria of the continental water cycle. *Geophysical Research Letters*, 33(24).

DeDeo, S. (2011). Effective theories for circuits and automata. *Chaos: An Interdisciplinary Journal of Nonlinear Science*, 21(3):–.

Dekker, S. and Rietkerk, M. (2007). Coupling microscale vegetation soil water and macroscale vegetation precipitation feedbacks in semiarid ecosystems. *Global change biology*, pages 1–8.

Dieckmann, U., Law, R., and Metz, J. A. J. (2000). *The Geometry of Ecological Interactions*. Cambridge University Press.

Dijkstra, H. A. (2011). Vegetation pattern formation in a semi-arid climate. *International Journal of Bifurcation and Chaos*, 21(12):3497–3509.

Ekici, A., Beer, C., Hagemann, S., and Hauck, C. (2013). Improved soil physics for simulating high latitude permafrost regions by the jsbach terrestrial ecosystem model. *Geoscientific Model Development Discussions*, 6(2):2655–2698.

Eppinga, M., Rietkerk, M., Borren, W., Lapshina, E., Bleuten, W., and Wassen, M. (2008). Regular surface patterning of peatlands: Confronting theory with field data. *Ecosystems*, 11(4):520–536.

Fortier, D., Allard, M., and Shur, Y. (2007). Observation of rapid drainage system development by thermal erosion of ice wedges on bylot island, canadian arctic archipelago. *Permafrost and Periglacial Processes*, 18(3):229–243.

French, H. (2007). *The periglacial environment*. Wiley, West Sussex, England, 3rd edition.

Garcia-Carreras, L., Parker, D. J., Taylor, C. M., Reeves, C. E., and Murphy, J. G. (2010). Impact of mesoscale vegetation heterogeneities on the dynamical and thermodynamic properties of the planetary boundary layer. *Journal of Geophysical Research: Atmospheres*, 115(D3):n/a–n/a.

Gažovič, M., Kutzbach, L., Schreiber, P., Wille, C., and Wilmking, M. (2010). Diurnal dynamics of ch4 from a boreal peatland during snowmelt. *Tellus B*, 62(3):133–139.

Gell-Mann, M. and Low, F. E. (1954). Quantum electrodynamics at small distances. *Phys. Rev.*, 95:1300–1312.

Grimmett, G. (1999). *Percolation(Google eBook)*. Springer-Verlag, New York, second edition.

Hadwiger, H. (1957). *Vorlesungen über Inhalt, Oberfläche und Isoperimetrie*. Springer-Verlag, Berlin.

Haltigin, T., Pollard, W., and Dutilleul, P. (2011). Statistical evidence of polygonal terrain self organization on earth and mars. In *Lunar and Planetary Institute Science Conference Abstracts*, volume 42, page 1622. 42nd Lunar and Planetary Science Conference, held March 711, 2011 at The Woodlands, Texas. LPI Contribution.

Hasegawa, M. and Tanemura, M. (1976). On the pattern of space division by territories. *Annals of the Institute of Statistical Mathematics*, 28(1):509–519.

Helbig, M., Boike, J., Langer, M., Schreiber, P., Runkle, B., and Kutzbach, L. (2013). Spatial and seasonal variability of polygonal tundra water balance: Lena river delta, northern siberia (russia). *Hydrogeology Journal*, 21(1):133–147.

HilleRisLambers, R., Rietkerk, M., van den Bosch, F., Prins, H. H. T., and de Kroon, H. (2001). Vegetation pattern formation in semi-arid grazing system. *Ecology*, 82(1):50–61.

Hugelius, G., Tarnocai, C., Broll, G., Canadell, J. G., Kuhry, P., and Swanson, D. K. (2013). The northern circumpolar soil carbon database: spatially distributed datasets of soil coverage and soil carbon storage in the northern permafrost regions. *Earth System Science Data*, 5(1):3–13.

Janssen, R. H. H., Meinders, M. B. J., van NES, E. H., and Scheffer, M. (2008). Microscale vegetation-soil feedback boosts hysteresis in a regional vegetationclimate system. *Global Change Biology*, 14(5):1104–1112.

Kéfi, S., Dakos, V., Scheffer, M., Van Nes, E. H., and Rietkerk, M. (2013). Early warning signals also precede non-catastrophic transitions. *Oikos*, 122(5):641–648.

Kéfi, S., Rietkerk, M., Alados, C. L., Pueyo, Y., Papanastasis, V. P., Elaich, A., and de Ruiter, P. C. (2007). Spatial vegetation patterns and imminent desertification in Mediterranean arid ecosystems. *Nature*, 449(7159):213–7.

Kettunen, A., Kaitala, V., Lehtinen, A., Lohila, A., Alm, J., Silvola, J., and Martikainen, P. J. (1999). Methane production and oxidation potentials in relation to water table fluctuations in two boreal mires. *Soil Biology and Biochemistry*, 31(12):1741 – 1749.

Kirschke, S., Bousquet, P., Ciais, P., Saunois, M., Canadell, J. G., Dlugokencky, E. J., Bergamaschi, P., Bergmann, D., Blake, D. R., Bruhwiler, L., Cameron-Smith, P., Castaldi, S., Chevallier, F., Feng, L., Fraser, A., Heimann, M., Hodson, E. L., Houweling, S., Josse, B., Fraser, P. J., Krummel, P. B., Lamarque, J.-F., Langenfelds, R. L., Le Quere, C., Naik, V., O'Doherty, S., Palmer, P. I., Pison, I., Plummer, D., Poulter, B., Prinn, R. G., Rigby, M., Ringeval, B., Santini, M., Schmidt, M., Shindell, D. T., Simpson, I. J., Spahni, R., Steele, L. P., Strode, S. A., Sudo, K., Szopa, S., van der Werf, G. R., Voulgarakis, A., van Weele, M., Weiss, R. F., Williams, J. E., and Zeng, G. (2013). Three decades of global methane sources and sinks. *Nature Geosciensces*, 6:813–823.

Kleinen, T., Brovkin, V., and Schuldt, R. J. (2012). A dynamic model of wetland extent and peat accumulation: results for the Holocene. *Biogeosciences*, 9(1):235–248.

Kletter, a. Y., von Hardenberg, J., Meron, E., and Provenzale, a. (2009). Patterned vegetation and rainfall intermittency. *Journal of theoretical biology*, 256(4):574–83.

Kolka, R. K., Sebestyen, S. D., Verry, E. S., and Brooks, K. N. (2011). *Peatland Biogeochemistry and Watershed Hydrology at the Marcell Experimental Forest*. CRC Press, Taylor & Francis Group.

Kutzbach, L., Wagner, D., and Pfeiffer, E.-M. (2004). Effect of microrelief and vegetation on methane emission from wet polygonal tundra, Lena Delta, Northern Siberia. *Biogeochemistry*, 69:341–362.

Lachenbruch, A. H. (1972). *Mechanics of thermal contraction cracks and ice-wedge polygons in permafrost*, volume 70. Geological Society of America.

Langer, M., Westermann, S., and Boike, J. (2010). Remote Sensing of Environment Spatial and temporal variations of summer surface temperatures of wet polygonal tundra in Siberia - implications for MODIS LST based permafrost monitoring. *Remote Sensing of Environment*, 114(9):2059–2069.

Langer, M., Westermann, S., Heikenfeld, M., Dorn, W., and Boike, J. (2013). Satellite-based modeling of permafrost temperatures in a tundra lowland landscape. *Remote Sensing of Environment*, 135(0):12 – 24.

Langer, M., Westermann, S., Muster, S., Piel, K., and Boike, J. (2011a). Permafrost and surface energy balance of a polygonal tundra site in Northern Siberia Part 2 : Winter. *The Cryosphere*, 5:509–524.

Langer, M., Westermann, S., Muster, S., Piel, K., and Boike, J. (2011b). The surface energy balance of a polygonal tundra site in northern Siberia Part 1: Spring to fall. *The Cryosphere*, 5(1):151–171.

Larsen, L. G., Choi, J., Nungesser, M. K., and Harvey, J. W. (2012). Directional connectivity in hydrology and ecology. *Ecological Applications*, 22(8):2204–2220.

Law, B., Falge, E., Gu, L., Baldocchi, D., Bakwin, P., Berbigier, P., Davis, K., Dolman, A., Falk, M., Fuentes, J., Goldstein, A., Granier, A., Grelle, A., Hollinger, D., Janssens, I., Jarvis, P., Jensen, N., Katul, G., Mahli, Y., Matteucci, G., Meyers, T., Monson, R., Munger, W., Oechel, W., Olson, R., Pilegaard, K., U, K. P., Thorgeirsson, H., Valentini, R., Verma, S., Vesala, T., Wilson, K., and Wofsy, S. (2002). Environmental controls over carbon dioxide and water vapor exchange of terrestrial vegetation. *Agricultural and Forest Meteorology*, 113(14):97 – 120. {FLUXNET} 2000 Synthesis.

Lehmann, P., Wyss, P., Flisch, A., Lehmann, E., Vontobel, P., Krafczyk, M., Kaestner, A., Beckmann, F., Gygi, A., and Flhler, H. (2006). Tomographical Imaging and Mathematical Description of Porous Media Used for the Prediction of Fluid Distribution. *Vadose Zone Journal*, (5):80–97.

Levy, J. S., Marchant, D. R., and Head, J. W. (2010). Thermal contraction crack polygons on Mars: A synthesis from HiRISE, Phoenix, and terrestrial analog studies. *Icarus*, 206(1):229–252.

Liljedahl, A., Hinzman, L., and Schulla, J. (2012). Ice-wedge polygon type controls low-gradient watershed-scale hydrology. In *Tenth International Conference on Permafrost, Salekhard, Russia*.

Limpens, J., Berendse, F., Blodau, C., Canadell, J. G., Freeman, C., Holden, J., Roulet, N., Rydin, H., and Schaepman-Strub, G. (2008). Peatlands and the carbon cycle: from local processes to global implications a synthesis. *Biogeosciences*, 5(5):1475–1491.

Loisel, J. and Yu, Z. (2013). Holocene peatland carbon dynamics in patagonia. *Quaternary Science Reviews*, 69(0):125 – 141.

Lucarini, V. (2009). Symmetry-Break in Voronoi Tessellations. *Symmetry*, 1(1):21–54.

Lucarini, V., Danihlik, R., Kriegerova, I., and Speranza, A. (2008). Hydrological cycle in the Danube basin in present-day and XXII century simulations by IPCCAR4 global climate models. *Journal of Geophysical Research*, 113(D9):1–17.

Mecke, K. (2000). Additivity, convexity, and beyond: Applications of minkowski functionals in statistical physics. In Mecke, K. and Stoyan, D., editors, *Statistical Physics and Spatial Statistics*, volume 554 of *Lecture Notes in Physics*, pages 111–184. Springer Berlin Heidelberg.

Melton, J. R. and Arora, V. K. (2014). Sub-grid scale representation of vegetation in global land surface schemes: implications for estimation of the terrestrial carbon sink. *Biogeosciences*, 11(4):1021–1036.

Melton, J. R., Wania, R., Hodson, E. L., Poulter, B., Ringeval, B., Spahni, R., Bohn, T., Avis, C. A., Beerling, D. J., Chen, G., Eliseev, A. V., Denisov, S. N., Hopcroft, P. O., Lettenmaier, D. P., Riley, W. J., Singarayer, J. S., Subin, Z. M., Tian, H., Zürcher, S.,

Brovkin, V., van Bodegom, P. M., Kleinen, T., Yu, Z. C., and Kaplan, J. O. (2013). Present state of global wetland extent and wetland methane modelling: conclusions from a model inter-comparison project (wetchimp). *Biogeosciences*, 10(2):753–788.

Miles, R. E. and Maillardet, R. J. (1982). The basic structures of voronoi and generalized voronoi polygons. *Journal of Applied Probability*, 19:pp. 97–111.

Mohammed, A., Stoy, P. C., and Malthus, T. J. (2012). Information preservation and change detection across spatial scales in the assessment of global ch4 emission estimates from wetlands. *The International Journal of Climate Change: Impacts and Responses*, 1:93–114.

Moore, T. R. and Knowles, R. (1989). The influence of water table levels on methane and carbon dioxide emissions from peatland soils. *Canadian Journal of Soil Science*, 69(1):33–38.

Morris, P. J., Baird, A. J., and Belyea, L. R. (2012). The digibog peatland development model 2: ecohydrological simulations in 2d. *Ecohydrology*, 5(3):256–268.

Morris, P. J., Baird, A. J., and Belyea, L. R. (2013). The role of hydrological transience in peatland pattern formation. *Earth Surface Dynamics*, 1(1):29–43.

Muster, S., Heim, B., Abnizova, A., and Boike, J. (2013). Water body distributions across scales: A remote sensing based comparison of three arctic tundra wetlands. *Remote Sensing*, 5(4):1498–1523.

Muster, S., Langer, M., Heim, B., Westermann, S., and Boike, J. (2012). Subpixel heterogeneity of ice-wedge polygonal tundra : a multi-scale analysis of land cover and evapotranspiration in the Lena River Delta , Siberia. *Tellus Series B Chemical And Physical Meteorology*, 1:1–19.

Nichols, D. S. and Brown, J. M. (1980). Evaporation from a sphagnum moss surface. *Journal of Hydrology*, 48(34):289 – 302.

Nungesser, M. K. (2003). Modelling microtopography in boreal peatlands: hummocks and hollows. *Ecological Modelling*, 165(2-3):175–207.

O'Connor, F., Boucher, O., Gedney, N., Jones, C. D., Folberth, G. A., Coppell, R., Friedlingstein, P., Collins, W. J., Chappellaz, J., Ridley, J., and Johnson, C. E. (2010). Possible role of wetlands, permafrost, and methane hydrates in the methane cycle under future climate change: A review. *Reviews of Geophysics*, 48(4):1–33.

Okabe, A., Boots, B., Sugihara, K., and Chiu, S. N. (2000). *Spatial tessellations: concepts and applications of Voronoi diagrams*. John Wiley & Sons, second edition.

Pielke, R. A., Sr, Avissar, R. I., Raupach, M., Dolman, A. J., Zeng, X., and Denning, A. S. (1998). Interactions between the atmosphere and terrestrial ecosystems: influence on weather and climate. *Global Change Biology*, 4(5):461–475.

Pithan, F. and Mauritsen, T. (2014). Arctic amplification dominated by temperature feedbacks in contemporary climate models. *Nature Geosciences*, 7:181–184.

Raddatz, T., Reick, C., Knorr, W., Kattge, J., Roeckner, E., Schnur, R., Schnitzler, K.-G., Wetzel, P., and Jungclaus, J. (2007). Will the tropical land biosphere dominate the climate-carbon cycle feedback during the twenty-first century? *Climate Dynamics*, 29(6):565–574.

Rietkerk, M., Brovkin, V., van Bodegom, P. M., Claussen, M., Dekker, S. C., Dijkstra, H. a., Goryachkin, S. V., Kabat, P., van Nes, E. H., Neutel, A.-M., Nicholson, S. E., Nobre, C., Petoukhov, V., Provenzale, A., Scheffer, M., and Seneviratne, S. I. (2011). Local ecosystem feedbacks and critical transitions in the climate. *Ecological Complexity*, 8(3):223–228.

Rietkerk, M. and van de Koppel, J. (2008). Regular pattern formation in real ecosystems. *Trends in ecology & evolution (Personal edition)*, 23(3):169–75.

Roth, K., Boike, J., and Vogel, H.-J. (2005). Quantifying permafrost patterns using Minkowski densities. *Permafrost and Periglacial Processes*, 16(3):277–290.

Runkle, B., Wille, C., Gaovi, M., Wilmking, M., and Kutzbach, L. (2014). The surface energy balance and its drivers in a boreal peatland fen of northwestern russia. *Journal of Hydrology*, 511(0):359 – 373.

Runkle, B. R. K., Wille, C., Gažovič, M., and Kutzbach, L. (2012). Attenuation Correction Procedures for Water Vapour Fluxes from Closed-Path Eddy-Covariance Systems. *Boundary-Layer Meteorology*, 142(3):401–423.

Sachs, T., Giebels, M., Boike, J., and Kutzbach, L. (2010). Environmental controls on CH4 emission from polygonal tundra on the microsite scale in the Lena river delta, Siberia. *Global Change Biology*, 16:3096–3110.

Sachs, T., Wille, C., Boike, J., and Kutzbach, L. (2008). Environmental controls on ecosystem-scale CH 4 emission from polygonal tundra in the Lena River Delta, Siberia. *Journal of Geophysical Research*, 113:1–12.

Scheffer, M., Bascompte, J., Brock, W. a., Brovkin, V., Carpenter, S. R., Dakos, V., Held, H., van Nes, E. H., Rietkerk, M., and Sugihara, G. (2009). Early-warning signals for critical transitions. *Nature*, 461(7260):53–9.

Scheffer, M., Holmgren, M., Brovkin, V., and Claussen, M. (2005). Synergy between small- and large-scale feedbacks of vegetation on the water cycle. *Global Change Biology*, 11(7):1003–1012.

Schneider, J., Kutzbach, L., and Wilmking, M. (2012). Carbon dioxide exchange fluxes of a boreal peatland over a complete growing season, komi republic, nw russia. *Biogeochemistry*, 111(1-3):485–513.

Schuldt, R. J., Brovkin, V., Kleinen, T., and Winderlich, J. (2013). Modelling Holocene carbon accumulation and methane emissions of boreal wetlands an Earth system model approach. *Biogeosciences*, 10(3):1659–1674.

Schuur, E. a. G., Bockheim, J., Canadell, J. G., Euskirchen, E., Field, C. B., Goryachkin, S. V., Hagemann, S., Kuhry, P., Lafleur, P. M., Lee, H., Mazhitova, G., Nelson, F. E., Rinke, A., Romanovsky, V. E., Shiklomanov, N., Tarnocai, C., Venevsky, S., Vogel, J. G., and Zimov, S. a. (2008). Vulnerability of Permafrost Carbon to Climate Change: Implications for the Global Carbon Cycle. *BioScience*, 58(8):701–714.

Schymanski, S. J., Kleidon, A., Stieglitz, M., and Narula, J. (2010). Maximum entropy production allows a simple representation of heterogeneity in semiarid ecosystems. *Philosophical transactions of the Royal Society of London. Series B, Biological sciences*, 365(1545):1449–55.

Serra, J. (1982). *Image analysis and mathematical morphology.* Academic Press, London.

Sheffer, E., von Hardenberg, J., Yizhaq, H., Shachak, M., and Meron, E. (2013). Emerged or imposed: a theory on the role of physical templates and self-organisation for vegetation patchiness. *Ecology letters*, 16(2):127–39.

Shur, Y. L. and Jorgenson, M. T. (2007). Patterns of permafrost formation and degradation in relation to climate and ecosystems. *Permafrost and Periglacial Processes*, 18(1):7–19.

Skurikhin, A. N., Gangodagamage, C., Rowland, J. C., and Wilson, C. J. (2013). Arctic tundra ice-wedge landscape characterization by active contours without edges and structural analysis using high-resolution satellite imagery. *Remote Sensing Letters*, 4(11):1077–1086.

Smith, L. C., MacDonald, G. M., Velichko, A. A., Beilman, D. W., Borisova, O. K., Frey, K. E., Kremenetski, K. V., and Sheng, Y. (2004). Siberian peatlands a net carbon sink and global methane source since the early holocene. *Science*, 303(5656):353–356.

Stoy, P. C., Williams, M., Spadavecchia, L., Bell, R. a., Prieto-Blanco, a., Evans, J. G., and Wijk, M. T. (2009). Using Information Theory to Determine Optimum Pixel Size and Shape for Ecological Studies: Aggregating Land Surface Characteristics in Arctic Ecosystems. *Ecosystems*, 12(4):574–589.

Strack, M. (2004). Effect of water table drawdown on northern peatland methane dynamics: Implications for climate change. *Global Biogeochemical Cycles*, 18(4):1–7.

Tarnocai, C., Canadell, J. G., Schuur, E. A. G., Kuhry, P., Mazhitova, G., and Zimov, S. (2009). Soil organic carbon pools in the northern circumpolar permafrost region. *Global Biogeochemical Cycles*, 23(2).

Turunen, J., Tomppo, E., Tolonen, K., and Reinikainen, A. (2002). Estimating carbon accumulation rates of undrained mires in finlandapplication to boreal and subarctic regions. *The Holocene*, 12(1):69–80.

Vogel, H.-J., Hoffmann, H., and Roth, K. (2005). Studies of crack dynamics in clay soil: I. experimental methods, results, and morphological quantification. *Geoderma*, 125(34):203 – 211.

Vogel, H.-J., Weller, U., and Schlter, S. (2010). Quantification of soil structure based on minkowski functions. *Computers and Geosciences*, 36(10):1236 – 1245.

von Hardenberg, J., Meron, E., Shachak, M., and Zarmi, Y. (2001). Diversity of Vegetation Patterns and Desertification. *Physical Review Letters*, 87(19):3–6.

Waddington, J. M., Roulet, N. T., and Swanson, R. V. (1996). Water table control of ch4 emission enhancement by vascular plants in boreal peatlands. *Journal of Geophysical Research: Atmospheres*, 101(D17):22775–22785.

Walter, B. P. and Heimann, M. (2000). A process-based, climate-sensitive model to derive methane emissions from natural wetlands: Application to five wetland sites, sensitivity to model parameters, and climate. *Global Biogeochemical Cycles*, 14(3):745–765.

Walter, B. P., Heimann, M., Shannon, R., and White, J. (1996). A process-based model to derive methane emissions from natural wetlands. *Geophysical Research Letters*, 23(25):3731–3734.

Walter, K. M., Zimov, S. a., Chanton, J. P., Verbyla, D., and Chapin, F. S. (2006). Methane bubbling from Siberian thaw lakes as a positive feedback to climate warming. *Nature*, 443(7107):71–75.

Wania, R., Melton, J. R., Hodson, E. L., Poulter, B., Ringeval, B., Spahni, R., Bohn, T., Avis, C. A., Chen, G., Eliseev, A. V., Hopcroft, P. O., Riley, W. J., Subin, Z. M., Tian, H., van Bodegom, P. M., Kleinen, T., Yu, Z. C., Singarayer, J. S., Zürcher, S., Lettenmaier, D. P., Beerling, D. J., Denisov, S. N., Prigent, C., Papa, F., and Kaplan, J. O. (2013). Present state of global wetland extent and wetland methane modelling: methodology of a model inter-comparison project (wetchimp). *Geoscientific Model Development*, 6(3):617–641.

Wania, R., Ross, I., and Prentice, I. C. (2009a). Integrating peatlands and permafrost into a dynamic global vegetation model: 1. Evaluation and sensitivity of physical land surface processes. *Global Biogeochemical Cycles*, 23(3):1–19.

Wania, R., Ross, I., and Prentice, I. C. (2009b). Integrating peatlands and permafrost into a dynamic global vegetation model: 2. Evaluation and sensitivity of vegetation and carbon cycle processes. *Global Biogeochemical Cycles*, 23(3):1–15.

Wieder, R. K., Turetsky, M. R., and Vile, M. A. (2009). Peat as an Archive of Atmospheric, Climatic and Environmental Conditions. In Maltby, E. and Barker, T., editors, *The Wetlands Handbook*, pages 96–112. Blackwell Publishing, 1 edition.

Wille, C., Kutzbach, L., Sachs, T., Wagner, D., and Pfeiffer, E.-M. (2008). Methane emission from Siberian arctic polygonal tundra: eddy covariance measurements and modeling. *Global Change Biology*, 14(6):1395–1408.

Wolf, U. (2009). Above- and belowground methane dynamics of a peatland ecosystem of varying vegetation composition during summer in the Komi Republic, Russia.

Yu, Z., Loisel, J., Brosseau, D. P., Beilman, D. W., and Hunt, S. J. (2010). Global peatland dynamics since the last glacial maximum. *Geophysical Research Letters*, 37(13):n/a–n/a.

Zhang, Y., Sachs, T., Li, C., and Boike, J. (2012). Upscaling methane fluxes from closed chambers to eddy covariance based on a permafrost biogeochemistry integrated model. *Global Change Biology*, 18(4):1428–1440.

Zona, D., Lipson, D. a., Zulueta, R. C., Oberbauer, S. F., and Oechel, W. C. (2011). Microtopographic controls on ecosystem functioning in the Arctic Coastal Plain. *Journal of Geophysical Research*, 116(January):1–12.

Acknowledgements

At the end of these years I am happy to have the chance to thank all the people who helped me along the way.

First and foremost I want to express my gratitude to my supervisor, Victor Brovkin, for the inspiration and the help he gave me during the whole duration of my work under his guidance. He was able to stimulate my curiosity towards Arctic environments and the carbon cycle, and he played a fundamental role in my development as a scientist. I also want to acknowledge the great help of Martin Claussen and Andreas Chlond, who deeply helped me in developing and assessing my work during our discussions in the panel meetings.

I want to thank a lot Lars Kutzbach, Ben Runkle, Julia Boike, Sina Muster, Armine Avagyan, and Thorsten Sachs for the long discussions that were necessary for the development of my ideas. All of them helped me to visualize better the high-latitude environments from the "field scientist" perspective. I also take the chance to thank all people here in the Land Department, Thomas Kleinen in particular, who helped me a great deal with useful comments and discussions.

I would like to thank Andy Baird, Murray Lark, and an anonymous reviewer for the comments during the revision of the manuscript describing the results of Chapter 2.

I would also like to express my gratitude to Antonello Provenzale and to Mara Baudena, who introduced me to land surface modeling during my Master's thesis. They both played a major role in my arrival here at the MPI in Hamburg as a PhD student.

During these three years I had the chance to be part of this great school that is the IMPRS. I need to thank Antje Weitz, Wiebke Böhm, and Connie Kampmann for their patience, help and support in these years. If the IMPRS is such a successful school and such a great experience for so many of us, it is also thanks to them. I would also like to thank my (numerous) office mates with whom I shared work and laughters along the way: Sebastian, Helge, Andreas, Victoria, and in particular Jessica, who had to cope with me till the very end. I express my gratitude also to the other PhD students of the IMPRS for the nice time we had at the numerous retreats.

I would like to thank all people I met during my summer/winter schools and during the conferences I attended. With many of them I shared a lot of very nice and funny moments, both scientifically and personally. In particular, I would like to mention the participants in the "Training School on Terrestrial Biosphere Modelling", the fellow peat-friends I met in the "Carbon dynamics and exchange in peatlands" in Umeå, and the participants in the great "Complex System Summer School" in Santa Fe. All these experiences have been very important for the development of my research, and I want to thank Victor once again for allowing me to take part in all of them.

During this time here I met many nice people, and it is going to be difficult to remember you all. Max and Ritthik, I will never forget our Fridays during the first months at the fake *Bok* (and the consequent bellyaches), nor the beers at *Omas*, nor our trips. Well, in a way they were more *your* trips... And I also want to thank Mathias and Daniel, who from Hamburg, to Beijing, to San Francisco, showed me the true colors of German culture. Es hat was mit Bier zu tun.

I will not forget my small Italian clique here in Hamburg. Sarà impossibile dimenticare le cene da Ciccio con la Juve e col suo vinello, le tirate fino a tardissimo con Francesco,

e le tante risate con Lorenza. Al buon Jacopo, va un sentito grazie perché non ci siamo persi nonostante la distanza. A proposito di italiani, poi, non posso non nominare i sempre giovanissimi, sempre presenti, ma non sempre opportuni Marco, Paolo e Paolo. Non è del tutto appropriato ricordare qui i tanti motivi per cui vi ringrazio, ma, insomma, *you know what I mean*!

Voglio poi ringraziare la mia famiglia, i miei genitori e mio fratello Gianluca, per tutto il supporto che mi hanno dato in questi tre anni, per avermi dato la possibilità di essere qui e di seguire i miei sogni. Senza di voi non sarei qui.

Und am Ende möchte ich mich bei dir bedanken, Annika. Danke für die Liebe, die Geduld mit mir und manchmal auch meiner "Paranoia". Danke, dass du immer für mich da bist. Du hast mein Leben verändert.

Eidesstattliche Versicherung / *Declaration on oath*

Hiermit erkläre ich an Eides Statt, dass ich die vorliegende Dissertationsschrift selbst verfasst und keine anderen als die angegebenen Quellen und Hilfsmittel benutzt habe.

I hereby declare, on oath, that I have written the present dissertation by my own and have not used other than the acknowledged resources and aids.

Hamburg _____ Unterschrift / Signature _____

(Datum / Date)

Hinweis / Reference

Die gesamten Veröffentlichungen in der Publikationsreihe des MPI-M
„Berichte zur Erdsystemforschung / Reports on Earth System Science“,
ISSN 1614-1199

sind über die Internetseiten des Max-Planck-Instituts für Meteorologie erhältlich:
http://www.mpimet.mpg.de/wissenschaft/publikationen.html

All the publications in the series of the MPI -M
„Berichte zur Erdsystemforschung / Reports on Earth System Science“,
ISSN 1614-1199

are available on the website of the Max Planck Institute for Meteorology:
http://www.mpimet.mpg.de/wissenschaft/publikationen.html